ABSTRACT

ELECTRIC-FIELD ASSISTED MANIPULATION AND SELF-ASSEMBLY OF PARTICLE SUSPENSIONS

by

Edison Chijioke Amah

The aim of this dissertation is to model the processes by which particles suspended in liquids and at liquid surfaces self-assemble when they are subjected to uniform and non-uniform electric fields. To understand the role of electric forces, three related problems were studied numerically and experimentally.

In the first problem, particles are assumed to be suspended inside a liquid and a nonuniform electric field is applied using electrodes mounted in the domain walls which causes positively polarized particles to collect in the regions where the electric field intensity is locally maximal and the negatively polarized particles collect in the regions where the electric field intensity is locally minimal. A direct numerical simulation (DNS) scheme based on the Maxwell stress tensor (MST) method is developed to simulate the motion.

In the second problem, a uniform electric field is applied to manipulate particles adsorbed on the surface of a drop. The presence of the drop makes the electric field nonuniform and this gives rise to dielectrophoretic forces and an electrohydrodynamic (EHD) flow which cause particles to collect either at the poles

or the equator of the drop. The EHD flow, which arises because of the accumulation of charge on the surface of the drop, can be from pole-to-equator or equator-to-pole, depending on the properties of the drop and ambient liquids. When the fluid and particles properties are such that the EHD and DEP forces are in the opposite directions, particles can be moved from the poles to the equator, or *vice versa*, by varying the frequency.

In the third problem, a mixture of positively and negatively polarized particles adsorbed on a flat liquid surface was manipulated by applying an electric field in the direction normal to the surface. Both experiments and numerical simulations show that the resulting inter-particle forces cause particles to self-assemble into molecular-like hierarchical arrangements, consisting of particle chains or composite particles arranged in a pattern. The structure of a composite particle depends on factors such as the relative sizes and the number ratio of the particles, and their polarizabilities.

ELECTRIC-FIELD ASSISTED MANIPULATION AND SELF-ASSEMBLY OF PARTICLE SUSPENSIONS

by
Edison Chijioke Amah

Co-Advisor: Dr. Pushpendra Singh
Co-Advisor: Dr. Ian Fischer

A Dissertation
Submitted to the Faculty of
New Jersey Institute of Technology
in Partial Fulfillment of the Requirements for the Degree of
Doctor of Philosophy in Mechanical Engineering

Department of Mechanical and Industrial Engineering

May 2018

APPROVAL PAGE

ELECTRIC-FIELD ASSISTED MANIPULATION AND SELF-ASSEMBLY OF PARTICLE SUSPENSIONS

Edison Chijioke Amah

Dr. Pushpendra Singh, Dissertation Co-Advisor — Date
Professor of Mechanical Engineering, NJIT

Dr. Ian Fischer, Dissertation Co-Advisor — Date
Professor of Mechanical Engineering, NJIT

Dr. Rao Joga, Committee Member — Date
Professor of Mechanical Engineering, NJIT

Dr. Denis Blackmore, Committee Member — Date
Professor of Mathematics, NJIT

Dr. Shawn Chester, Committee Member — Date
Assistant Professor of Mechanical Engineering, NJIT

Dr. Dibakar Datta, Committee Member — Date
Assistant Professor of Mechanical Engineering, NJIT

BIOGRAPHICAL SKETCH

Author: Edison Chijioke Amah

Degree: Doctor of Philosophy

Date: May 2018

Undergraduate and Graduate Education:

- Doctor of Philosophy in Mechanical Engineering,
  New Jersey Institute of Technology, Newark, NJ, 2018

- Bachelor of Science in Aeronautical and Astronautical Engineering,
  University of Washington, Seattle, WA, 2012

Major: Mechanical Engineering

Journal Publications:

Amah, E., Singh, P., and Janjua, M., P., 2018, "Direct numerical simulation (DNS) of particles in spatially varying electric fields," Fluids *(Submitted).*

Amah, E., Fischer, I., Singh, P., Musunuri, N., and Hossain, M., 2018, "Numerical simulations of electric field driven hierarchical self-assembly of monolayers of mixtures of particles," Physical Review E *(Submitted).*

Singh, P., Musunuri, N., Bunker, D., Pell, S., Amah, E., Fischer, I., and Hossain, M., 2017, "Capillarity-driven hydrophilous pollination in ruppia maritima l.," Biophysical Journal, *(Submitted).*

Benouaguef, I., Amah, E., Fischer, I., Blackmore, D., Singh, P., and Musunuri, N., 2017, Flow induced on a salt waterbody due to the impingement of a freshwater drop or a water source," Mechanics Research Communications, 85, pp. 89-95.

Amah, E., Singh, P., and Shah, K., 2016, "Electrohydrodynamic manipulation of particles adsorb on drop surfaces," Soft Matter, 12, pp. 1663-1673; DOI: 10.1039/C5SM02195B.

Singh, P, Hossain, M., Gurupatham, S.K., Shah, K., Amah, E., Ju, D., Janjua, M., Nudurupati, S., and Fischer, I., 2014, "Molecular-like hierarchical self-assembly of monolayers of mixtures of particles," Scientific Reports, 4, 7427; DOI: 10.1038/srep07427.

Amah, E., 2013, "Numerical simulation of flow over a circular cylinder using an immersed boundary method," The McNair Journal, UW, Seattle, WA, 12, pp. 67-75.

Conference Proceedings:

Amah, E., Musunuri, N., Singh, P., and Fischer, I., 2016, "Electric field driven hierarchical self-assembly of monolayers of mixtures of particles," *Proceedings of the 24th International Congress of Theoretical and Applied Mechanics*, Montreal (CA)

Amah, E., Fischer, I., Singh, P., and Hossain, M., 2016, "Self-assembly of monolayers of mixtures of particle," *Proceedings of the ASME Fluids Engineering Division Summer Meeting*, New York, NY, DOI:10.1115/ICNMM2016-1050.

Amah, E., Fischer, I., and Singh, P., 2016, "Transient electrohydrodynamic manipulation of particles on the surface of a drop," *Proceedings of the ASME Fluids Engineering Division Summer Meeting*, New York, NY, DOI:10.1115/HT2016-1051.

Amah, E., Singh, P., Fischer, I., and Shah, K., 2014, "Self-assembly and manipulation of particles on drop surfaces," *Proceedings of the 4th Joint ASME US-European Fluids Engineering Summer Meeting*, New York, NY, DOI: 10.1115/FEDSM2014-21792.

Amah, E., Janjua, M., and Singh, P., 2014, "Direct numerical simulation (DNS) of particles in spatially varying electric fields," *Proceedings of the 4th Joint ASME US-European Fluids Engineering Summer Meeting*, New York, NY, DOI:10.1115/FEDSM2014-21791.

Amah et al., 2012, "Defining a successful commercial lunar mining program," Proceedings *of AIAA Space 2012 Conference & Exposition*, Pasadena, CA, DOI: 10.2514/6.2012-5298.

Presentations:

Amah, E., Benouaguef, I., Fischer, I., Blackmore, D., Singh, P., and Musunuri, N., 2017, "Flow induced on the surface of a waterbody by a source," *70th Annual Meeting of the APS Division of Fluid Dynamics*, November 19-21, Denver, CO.

Amah, E., 2017, "Manipulation and self-assembly of particles in micro-channels and at liquid-fluid interfaces," Seminar, *Sandia National Laboratories*, August 17, Albuquerque, NM

Amah, E., Musunuri, N., Singh, P., and Fischer, I., 2016, "Numerical simulations of electric field driven hierarchical self-assembly of monolayers of binary mixtures of particles," *69th Annual Meeting of the APS Division of Fluid Dynamics*, November 20-22, Portland, OR.

Amah, E., Musunuri, N., Singh, P., and Fischer, I., 2016, "Electric field driven hierarchical self-assembly of monolayers of mixtures of particles," *24th International Congress of Theoretical and Applied Mechanics*, Aug 21-26, Montreal, Canada.

Amah, E., Fischer, I., and Singh, P., 2016, "Transient electrohydrodynamic manipulation of particles on the surface of a drop," *ASME 2016 Fluids Engineering Division Summer Meeting*, July 10-14, Washington, DC.

Amah, E., Musunuri, N., Singh, P., and Fischer, I., 2016, "Numerical simulation of Electric Field Driven Hierarchical Self-assembly of Monolayers of Mixtures of Particles," *ASME 2016 Fluids Engineering Division Summer Meeting*, July 10-14, Washington, DC.

Amah, E., Fischer, I., and Singh, P., 2015, "Electrohydrodynamic manipulation of particles adsorbed on the surface of a drop," *68th Annual Meeting of the APS Division of Fluid Dynamics*, November 22-24, Boston, MA.

Amah, E., Fischer, I., and Singh, P., 2015, "Electrohydrodynamic manipulation of particles adsorb on drop surfaces," *12th Annual Conference on Frontiers in Applied and Computational Mathematics*, Newark, NJ.

Amah, E., Fischer, I., and Singh, P., 2015, "Electrohydrodynamic manipulation of particles on drop surfaces," *3rd Northeast Complex Fluids and Soft Matter Workshop (NCS3)*, Newark, NJ.

Amah, E., Fischer, I., and Singh, P., 2014, "Electrohydrodynamic manipulation of particles on drop surfaces," *67th Annual Meeting of the APS Division of Fluid Dynamics*, November 23-25, San Francisco, CA.

Amah, E., Fischer, I., and Singh, P., 2014, "Electrohydrodynamic manipulation of particles on drop surfaces," *IX Annual GSA Graduate Student Research Day*, October 30, NJIT, Newark, NJ.

Amah, E., Janjua, M., and Singh, P., 2014, "Direct numerical simulation (DNS) of particles in spatially varying electric fields," *86th Annual Meeting of the Society of Rheology*, October 5-9, Philadelphia, PA.

Amah, E., Singh, P., Fischer, I., and Shah, K., 2014, "Self-assembly and manipulation of particles on drop surfaces," *ASME 4th Joint US-European Fluids Engineering Summer Meeting*, August 4-7, Chicago, IL.

Amah, E., Janjua, M., and Singh, P., 2014, "Direct numerical simulation (DNS) of particles in spatially varying electric fields," *ASME 4th Joint US-European Fluids Engineering Summer Meeting*, August 4-7, Chicago, IL.

Amah, E., Janjua, M., and Singh, P., 2013, "Direct numerical simulation (DNS) of particles in spatially varying electric fields," *66th Annual Meeting of the APS Division of Fluid Dynamics*, November 24-26, Pittsburg, PA.

Amah, E., Janjua, M., and Singh, P., 2013, "Direct numerical simulation (DNS) of particles in spatially varying electric fields," *16th Annual Philadelphia AMP Research Symposium and Mentoring Conference*, November 16, Philadelphia, PA.

Amah, E., 2013, "Direct numerical simulation (DNS) of particles in spatially varying electric fields," *IX Annual GSA Graduate Student Research Day*, October 31, NJIT, Newark, NJ.

Amah et al., 2012, "Defining a successful commercial lunar mining program," *AIAA Space 2012 Conference & Exposition*, AIAA, September 11-13, Pasadena, CA.

Amah et al., 2012, "Defining a successful commercial lunar mining program," *NASA/NIA RASC-AL Concept Design*, Cocoa Beach, FL.

Amah, E., 2012, "Numerical simulation of the flow over a circular cylinder using an immersed boundary method," *University of Washington McNair/Undergraduate Research Conference*, May 18, Seattle, WA. [Poster]

Amah, E., 2011, "Numerical simulation of flow over a flat plate," *National McNair Research Conference*, November 11-12, Milwaukee, WI.

This work is dedicated to my heroine, my late mother, Mrs. Grace Ifeoma Amah (Mkpurumma) whose unwavering love, sacrifices, guidance, motivation, and support, helped me to garner the courage and determination to pursue my doctorate, against all odds. May God bless you!

ACKNOWLEDGEMENT

I will like to genuinely thank those individuals, institutions, and academic programs that directly or indirectly provided academic, moral, and financial supports for me over the course of my doctorate study at NJIT. Without those supports, this doctoral dissertation would not have been made possible.

First, I will like to specially thank my research advisors, Professor Pushpendra Singh and Professor Ian Fischer. Since my admittance into the doctoral program, I have benefited immensely from their expertise and guidance, including academically, research-wise, professional development, as well as personal development. I owe a very high degree of my success in the program to them; their mentorship is invaluable. More so, nobody has pushed me outside of my comfort zone as Dr. Singh had done. As a stutterer, coming into the program, I never foresaw myself giving oral presentations of my research work in front of an audience. While I knew I would present my work someday, it did so occur to me that it would be too soon and frequent; which I become accustomed to it in a short period of time, all because of him. These conference presentations have helped me with my communication skills to be a more effective presenter. Over the duration of the doctoral study, I have presented my work in more than twenty technical

conferences, which I found helpful in improving my speech and communication skills, as well as building my confidence.

Academically, my dissertation is successful because of the immense expert contributions of each member of my dissertation committee: Dr. I. Joga Rao, Dr. Denis Blackmore, Dr. Shawn A. Chester and Dr. Dibakar Datta. I have interacted with majority of them both on professional and personal levels. Dr. Chester had accepted my accepted my invitation as a speaker for workshops organized by The PhD Club on several occasions. Dr. Rao's graduate continuum mechanics class expanded my understanding of fluid behaviors. Dr. Datta has been resourceful to me in molecular dynamics simulation. He had devoted his time to guide me in areas that I was having difficulties. Dr. Blackmore's expertise has been valuable in some of the research projects that I have worked on. I am grateful and appreciative of the advice, time and efforts they put in reshaping the final outcome of this dissertation.

I am grateful to the Education Opportunity Program (EOP) at NJIT, through which I was awarded a 2-year National Science Foundation (NSF) fellowship for my doctoral program. In addition, I am graciously indebted to Tony Howell and Yvette Johnson in EOP for their steadfast support in attending to my needs, whenever I walked into the office. Even after the tenure of my NSF

fellowship was over, Mr. Howell would always source for means to fund my conference-related travel expenses or reimbursements. While Mrs. Johnson, on the other hand, would not hesitate to file the necessary paperwork for the reimbursements of my conference expenses. I am forever very grateful to them.

A great thank you to all my relatives who have shown me moral support in one way or the other, whether through cards, gifts, and prayers; this support rekindled my perseverance at some trying stages of my study. On the same note, I specifically thank my father, Simon Chinwuba Amah; my elder brother, Ebuka Amah; and my younger brother, Ogonna Amah for their unwavering love and candid advices. I would not have pushed forward with the idea of getting a doctorate if not for the high perception of academics within the family. You contributed to who I am today, and I love you all for it.

My experience at NJIT would not have been exciting if not for the amazing friends and colleagues that made my stay worthwhile, both on-campus and off-campus. I will like to do "shoutouts" to my following friends, whom I have known since high school, for their support and for keeping my social life active: Nnamdi Uchegbu, Kene Okeke, and Emeka Molokwu. In addition, I will like to express gratitude to my colleagues: Dr. Kinnari Shah, Dr. Naga Musunri, Islam Benouaguef, Suchandra Das, and Dr. MD.Shahadat Hossain. These former

colleagues of mine immeasurably contributed their time and expertise to my projects: For instance, Dr. Shah, Dr. Musunri, and Dr. Hossain taught me how to operate most laboratory instruments, right from the first day I joined the research group. Islam has been like a brother to me from our very first day of class. He toured the city with me and taught me how to navigate the New York City's Subway. He is that friend who is always around whenever I ask for help.

Finally, I would like to acknowledge the various groups I have had the pleasure of working with during my stay at NJIT: The PhD Club and Graduate Student Association. These groups gave me platforms to express myself and make my voice heard on campus. Needless to say, I will to show my appreciation to the Graduate Student Office, especially Clarisa Gonzalez-Lenahan for the time she devotes in organizing the Thesis and Dissertation workshops, as well as reviewing the dissertation at multiple stages to make sure that it meets the approved format.

TABLE OF CONTENTS

TABLE OF CONTENTS
(Continued)

TABLE OF CONTENTS
(Continued)

Chapter **Page**

TABLE OF CONTENTS
(Continued)

LIST OF TABLES

LIST OF FIGURES

LIST OF FIGURES
(Continued)

Figure **Page**

LIST OF FIGURES
(Continued)

Figure **Page**

LIST OF FIGURES
(Continued)

Figure **Page**

LIST OF FIGURES
(Continued)

Figure **Page**

LIST OF FIGURES
(Continued)

Figure **Page**

LIST OF FIGURES
(Continued)

Figure **Page**

CHAPTER 1

INTRODUCTION

1.1 Objective

The aim of this dissertation is to model the electric field driven processes by which particles suspended in liquids and at liquid surfaces self-assemble when they are subjected to uniform and non-uniform electric fields. To understand the role of electric forces, three related problems were studied numerically and experimentally.

In the first problem, particles are assumed to be suspended inside a liquid and a nonuniform electric field is applied using electrodes mounted in the domain walls which causes positively polarized particles to collect in the regions where the electric field intensity is locally maximal and the negatively polarized particles collect in the regions where the electric field intensity is locally minimal. A direct numerical simulation (DNS) scheme based on the Maxwell stress tensor (MST) method is developed to simulate the motion of dielectric particles suspended in a dielectric liquid when it is subjected to an electric field. A particle in a spatially non-uniform electric field is subjected to an electrostatic force, called the dielectrophoretic (DEP) force, and a force that results from its dipole-dipole interaction with other particles. The latter, which is present even when the applied

electric field is uniform, is usually modeled using an approximate dipole-dipole interaction model. In the present work, the interaction forces are fully resolved by calculating the electric field everywhere in the domain including in the gaps between the particles and calculating the MST and integrating it on the surface of particles to obtain the total electric forces. The DNS results obtained from this scheme are compared with the numerical results obtained from the point-dipole approximation method. The MST based approach agrees with the point-dipole model when the spacing between the particles is larger, but as expected when the particles are closer together the point-dipole model results differ from the results obtained using the MST based method.

In the second problem, particles are adsorbed on the surface of a drop and a uniform electric field is applied to manipulate their distribution while they remain trapped on the surface of the drop. The presence of the drop makes the electric field nonuniform and this gives rise to dielectrophoretic forces and an electrohydrodynamic (EHD) flow which cause particles to collect either at the poles or the equator of the drop. The EHD flow, which arises because of the accumulation of charge on the surface of the drop, can be from pole-to-equator or equator-to-pole, depending on the properties of the drop and ambient liquids. The EHD flow is the dominant effect at low electric field frequencies when the drop and

ambient liquids are weakly conducting dielectric liquids. When the fluid and particles properties are such that the EHD and DEP forces are in the opposite directions, particles can be collected at the poles or the equator, and also can be moved from the poles to the equator, or *vice versa*, by varying the frequency.

In the third problem, a mixture of positively and negatively polarized micron- to nano-sized particles, adsorbed on a flat liquid surface, was manipulated by applying an electric field in the direction normal to the surface. Both experiments and numerical simulations show that the resulting inter-particle forces cause particle mixtures to self-assemble into molecular-like hierarchical arrangements, consisting of particle chains or composite particles arranged in a pattern. The structure of a composite particle depends on factors such as the relative sizes and the number ratio of the particles, their polarizabilities, and the electric field intensity. The initial distribution also influenced the final arrangement, especially when the speeds with which the two types of particles moved during the self-assembly process differed substantially.

1.2 Background

The drive to understand the physics surrounding the interfacial dynamics of particles is not just motivated by academic curiosity, but also by the real need for

better understanding of the principle behind such physical phenomena, and applying it to develop and advance novel technologies. The new physical insights gained from these projects can be applied to problems in manufacturing. Over the last two decades, considerable effort has been directed at developing efficient techniques for segregating and trapping micro to nano scale biological and other particles suspended in fluids. These techniques are important for a variety of applications, such as in devices being developed for classifying DNA and protein molecules in which the first step is to concentrate them [1], and also in devices being developed for detecting cells, and for removing particulates from fluids [2-11]. Solid colloidal capsules, e.g., Janus particles, can be produced by assembling colloidal particles at the surface of Pickering emulsions droplets [124].

A particle placed in a spatially varying field becomes polarized and experiences a net force, as a result of a phenomenon referred to as dielectrophoreis. This force on the particle is denoted as the dielectrophoretic (DEP) force. Dielectrophoresis is a powerful technique because particles with different dielectric constants respond differently as the force depends on their dielectric constant relative to that of the fluid in which they are suspended. Therefore, in principle, dielectrophoresis can be used to selectively manipulate and separate particles [3]. For example, it has been demonstrated that cancer cells can be removed from

human blood since their dielectric constant is different from that of normal cells [12-15].

Also, in recent years, studies have been conducted to understand the behavior of particles trapped at fluid-liquid interfaces because of their importance in a range of physical applications and biological processes, e.g., formation of pollen and insect egg rafts, self-assembly of particles at fluid-fluid interfaces resulting in novel nano structured materials, stabilization of emulsions, and the formation of anti-reflection coatings for high-efficiency solar cells, photonic crystals and biosensor arrays [30,58,59,60]. The use of particle stabilized emulsions has increased in the food, biomedical and materials industries since they offer many advantages over those stabilized using surfactants. For example, pH responsive particles can stabilize or destabilize emulsions depending on the pH value [38]. More so, emulsions stabilized by paramagnetic colloidal beads have been shown to undergo controlled phase separation in response to a magnetic field [39].

It is known that a drop placed in a uniform electric field, under a leaky dielectric condition, where either or both fluids are weakly conducting, deforms to a prolate or to an oblate shape. The degree of deformation depends on the electric Weber number. Deformation of a drop to an oblate shape has been noted to be due to a small but finite electrical conductivity of the fluids [43-47, 90-110]. Due to this

conductivity, charge migration to the drop's surface creates a transverse electric stress imbalance, which generates an electrohydrodynamic (EHD) flow, inside and outside of drop. The direction of the EHD flow depends on the properties of the fluids, while the flow strength depends strongly on the frequency of the ac electric field. Thus, since both the EHD force and DEP force acting on particles depend on the frequency, the frequency of an electric field is an important parameter which can be used to adjust the intensities of the DEP and EHD flow induced forces. A possible application is that when the two forces are directed in the opposite directions, binary particles, for example, can systematically be assembled on a drop surface by tuning to the right frequencies; where like particles occupy defined space on the drop's surface. Thus, this technique can be used for developing novel encapsulation methods in the field of nanotechnology, which can be efficiently applied in the making of Janus particles.

In addition, there have been studies to understand the behavior of particles adsorbed at fluid-liquid interfaces because of their importance in a range of physical applications, e.g., formation of anti-reflection coatings for high-efficiency solar cells. The absorption of solid partices at the boundary between two fluid phases can be accompanied by deformation of the liquid interface near the particle. Thus, particles adsorbed at fluid-liquid interfaces interact with one another via

lateral capillary interaction forces that arise mainly because of deformation of the interface by their weights, which enable them to form monolayer arrangements [61-65,117-120]. However, the formed monolayer has defects and lacks long-range order. Also, for submicron-sized particles of typical colloidal densities, the gravity-induced lateral capillary interaction forces are inadequate to produce a self-assembled monolayer. We have recently shown that monolayers containing two or more types of particles, even submicron particles, with different dielectric properties can be self-assembled by applying an electric field in the direction normal to the interface [65]. This is accomplished due to differences in the polarizabilities of both particles and liquids, and the sizes of the particles, which help to drive a hierarchical self-assembly process analogous to that which occurs at atomic scales [65].

1.3 Dissertation Organization

This dissertation is organized in the following order, starting from Chapter 1 where the overall objectives are presented.

In Chapter 2, a DNS scheme based on MST method is presented. The aim is to study the motion of dielectric particles suspended in a dielectric liquid and subjected to a spatially varying electric field. It is well known that a particle in a

spatially non-uniform electric field is subjected to an electrostatic force, called the DEP force, and will also interact electrostatically with other particles. The latter is usually modeled as dipole-dipole interactions, which are present even when the electric field is uniform. The DNS results obtained from this scheme is compared to the numerical results obtained from the point-dipole approximation method.

In Chapter 3, the behavior of particles adsorbed on the surface of a drop is studied at low electric field frequencies, when the drop and ambient liquids are weakly conducting dielectrics. The EHD flow, which arises because of the accumulation of charge on the surface of the drop, can be from pole-to-equator or equator-to-pole depending on the properties of the drop and ambient liquids. When the fluid and particles properties are such that the EHD and DEP forces are in the opposite directions, particles can be collected at the poles or the equator, and also can be moved from the poles to the equator, or *vice versa*, by varying the frequency.

Chapter 4 presents a numerical study of the process of self-assembly of particle mixtures on fluid-liquid interfaces, when an electric field is applied in the direction normal to the interface. The law governing the dependence of the electric field induced dipole-dipole and capillary forces on the distance between the particles and their physical properties, obtained by performing direct numerical

simulations in an earlier study, is used for conducting simulations of the self-assembly process of particle mixtures. The inter-particle forces cause micron- to nano-sized particle mixtures to self-assemble into molecular-like hierarchical arrangements consisting of composite particles which are organized in a pattern. As in experiments, the structure of a composite particle or monolayer depends on factors such as the relative sizes and the number ratio of the particles, their polarizabilities, and the electric field intensity.

Lastly, chapter 5 presents dissertation conclusions and proposes future work in the areas of the numerical study of the process of self-assembly of particle mixtures on fluid-liquid interfaces and the molecular dynamic simulation of molecules at air-fluid interfaces.

CHAPTER 2

DIRECT NUMERICAL SIMULATION OF PARTICLES IN SPATIALLY VARYING ELECTRIC FIELDS

2.1 Introduction

Over the last two decades considerable effort has been directed at developing efficient techniques for segregating and trapping micro to nano scale biological and other particles suspended in fluids. These techniques are important for a variety of applications, such as in devices being developed for classifying DNA and protein molecules in which the first step is to concentrate them [1], and also in devices being developed for detecting cells, and for removing particulates from fluids [2-11].

The DEP force arises because the particle becomes polarized and a polarized particle (or dipole) placed in a spatially varying electric field experiences a net force. This phenomenon itself is referred to as dielectrophoresis [2]. Dielectrophoresis is a powerful technique because particles with different dielectric constants respond differently as the force depends on their dielectric constant relative to that of the fluid in which they are suspended. Therefore, in principle, dielectrophoresis can be used to selectively manipulate and separate particles [3]. For example, it has been demonstrated that cancer cells can be removed from

human blood since their dielectric constant is different from that of normal cells [12-15].

Numerical simulations are essential for understanding the behavior of particles under various physical conditions, as well as for developing better designs for dielectrophoretic devices. We have developed a direct numerical simulation method to study the phenomena of dielectrophoresis in which the exact governing equations are solved to obtain the time-dependent motion of a fluid-particle system. A Direct numerical simulation (DNS) scheme, based on the distributed Lagrange multiplier (DLM) method, is used to study the problem numerically [26].

In most numerical studies to date, the electric force acting on a particle is computed using the point-dipole (PD) approximation [2,14]. In this approximation, the particle is considered small compared to the characteristic length over which the electric field varies, and the distance between particles is assumed to be much larger than their diameters. In the PD model, the electric force that a particle experiences has two components; one due to dielectrophoresis, and other due to particle-particle interaction. An energy based method was used by Bonnecaze & Brady to compute the electrostatic energy of the system subjected to an electrical field [16]. This method allows one to include particle-particle interaction in both far and near fields. As mentioned before, the accuracy of PD approximation diminishes

as non-uniformity of electric field increases or the distance between the particles is reduced. Some of these limitations can be improved by involving higher order multipole moment terms [17]. Even though the multipole technique is more accurate than the PD model, it still lacks the completeness of the Maxwell Stress Tensor (MST), in which the force is computed in terms of the electric field that is obtained by accounting for the presence of particles [18]. The MST method, however, requires calculation of the updated electric potential at each time step and thus is computationally more demanding [19-21]. In addition, there are several other studies that are limited to the prediction of the electric field and the DEP force lines in devices, and there are some in which the particle trajectories are obtained without accounting for the fluid-particle interactions [28,29].

2.2 Numerical Formulation

We first state the governing mass and momentum conservation equations for the motion of fluid and particles. Then, these equations are nondimensionalized and the governing dimensionless parameters are obtained. The domain containing a Newtonian fluid and N solid particles is denoted by Ω, the interior of the i^{th} particle by $P_i(t)$, and the domain boundary by G. The governing equations for the fluid-particle system are:

$$\rho_L\left(\frac{\partial \mathbf{u}}{\partial t}+\mathbf{u}\cdot\nabla\mathbf{u}\right)=-\nabla p+\nabla\cdot(2\eta\mathbf{D}) \quad \text{in} \quad \Omega\backslash\overline{P(t)} \tag{2.1}$$

$$\nabla\cdot\mathbf{u}=0 \ \text{ in } \Omega\setminus\overline{P(t)} \tag{2.2}$$

$$\begin{cases} \mathbf{u}=\mathbf{u}_L \ \text{ on } G \\ \mathbf{u}=\mathbf{U}_i+\boldsymbol{\omega}_i\times\mathbf{r}_i \ \text{ on, } \Gamma Pi \ \ i=1,\ldots,N \end{cases} \tag{2.3}$$

In Equations (2.1)-(2.5), $\mathbf{u}$ is the fluid velocity, p is the pressure, η is the dynamic viscosity of the fluid, ρ_L is the density of the fluid, $\mathbf{D}$ is the symmetric part of the velocity gradient tensor, and $\mathbf{U}_i$ and $\boldsymbol{\omega}_i$ are the linear and angular velocities of the i^{th} particle respectively, and $\Gamma_{Pi} = \partial P_i(t)$ is the boundary of the i$^{\text{th}}$ particle. The above equations are solved using the initial condition $\mathbf{u}|_{t=0}=\mathbf{u}_0$, where $\mathbf{u}_0$ is the known initial value of the velocity.

The linear velocity $\mathbf{U}_i$ and the angular velocity $\boldsymbol{\omega}_i$ of the i^{th} particle are governed by

$$m_i\frac{d\mathbf{U}_i}{dt}=\mathbf{F}_i+\mathbf{F}_{E,i} \tag{2.4}$$

$$I_i\frac{d\boldsymbol{\omega}_i}{dt}=\mathbf{T}_i+\mathbf{T}_{E,i} \tag{2.5}$$

$$\begin{cases} \mathbf{U}_i|_{t=0}=\mathbf{U}_{i,0} \\ \boldsymbol{\omega}_i|_{t=0}=\boldsymbol{\omega}_{i,0} \end{cases} \tag{2.6}$$

where m_i and I_i are the mass and moment of inertia of the i^{th} particle respectively. $\mathbf{F}_{\text{i}}$ and $\mathbf{T}_{\text{i}}$ are the hydrodynamic force and torque acting on the i^{th} particle, $\mathbf{F}_{E,i}$ is the electrostatic force acting on the i^{th} particle and $\mathbf{T}_{E,i}$ is the electrostatic torque acting on the i^{th} particle. This study is restricted to the case of spherical particles. Therefore, there is no need to keep track of the particle orientation. The particle positions are obtained from

$$\frac{d\mathbf{X}_i}{dt} = \mathbf{U}_i \tag{2.7}$$

$$\mathbf{X}_i \,|_{t=0} = \mathbf{X}_{i,0} \tag{2.8}$$

where $\mathbf{X}_{i,0}$ is the position of the i^{th} particle at time $t = 0$.

2.2.1 Point-dipole and Maxwell Stress Tensor Approaches

Based on the PD model approximation, the total electric force on a particle is the summation of the dielectrophoretic and the particle-particle interaction forces; the latter is present even when the electric field is uniform. In solving for the dielectrophoretic force using the PD model, the gradient of the electric field is assumed to be constant. Thus, the time averaged dielectrophoretic (DEP) force acting on a particle in an AC electric field, described in [2,14], is given by

$$\mathbf{F}_{DEP} = 2\pi a^3 \varepsilon_0 \varepsilon_c \beta \nabla \mathbf{E}^2 \tag{2.9}$$

where a is the particle radius, ε_c is the dielectric constant of the fluid, e_0 = 8.8542x10^{-12} F/m is the permittivity of free space and **E** is the RMS value of the electric field. Equation (2.9) is also valid for a DC electric field, where **E** is simply the electric field intensity. The coefficient $\beta(\omega)$ is the real part of the frequency dependent Clausius-Mossotti factor, given by

$$\beta(\omega) = \mathrm{Re}\left(\frac{\varepsilon_p^* - \varepsilon_c^*}{\varepsilon_p^* + 2\varepsilon_c^*} \right) \tag{2.10}$$

where ε_p^* and ε_c^* are the frequency dependent complex permittivities of the particle and fluid, respectively. The complex permittivity $\varepsilon^* = \varepsilon - j\sigma/\omega$, where ε is the permittivity, σ is the conductivity and $j = \sqrt{-1}$. The frequency dependence can be included in simulations by selecting an appropriate value of $\beta(\omega)$. The Clausius-Mossotti factor can take values between -0.5 and 1.0.

According to the PD model, the particle-particle interaction force on the i^{th} particle due to the j^{th} particle in a non-uniform electric field given in [19-25] is

$$\mathbf{F}_D = \frac{12\pi\varepsilon_0\varepsilon_c\beta^2 a^6}{r^4}\left(\mathbf{r}_{ij}\left(\mathbf{E}_i \cdot \mathbf{E}_j\right) + \left(\mathbf{r}_{ij} \cdot \mathbf{E}_i\right)\mathbf{E}_j + \left(\mathbf{r}_{ij} \cdot \mathbf{E}_j\right)\mathbf{E}_i - 5\mathbf{r}_{ij}\left(\mathbf{E}_i \cdot \mathbf{r}_{ij}\right)\left(\mathbf{E}_j \cdot \mathbf{r}_{ij}\right)\right) \tag{2.11}$$

where $\mathbf{r}_{ij}$ is the unit vector in the direction from the center of the i^{th} particle to the center of the j^{th} particle. This force is present even when the applied electric field is uniform.

For the Maxwell stress tensor (MST) approach, the electric force acting on a particle is obtained by solving for the electric field; which is calculated by first solving the electric potential problem shown below:

$$\nabla.(\varepsilon\nabla\varphi) = 0 \tag{2.12}$$

The boundary conditions on the particle surface are given by

$$\begin{cases} \varphi_1 = \varphi_2 \\ \varepsilon_c \dfrac{\partial\varphi_1}{\partial n} = \varepsilon_p \dfrac{\partial\varphi_2}{\partial n} \end{cases} \tag{2.13}$$

where φ_1 and φ_2 are the electric potential in the liquid and particles, respectively. The electric field is then calculated using the expression

$$\mathbf{E} = -\nabla\phi \tag{2.14}$$

The Maxwell stress tensor is given by

$$\boldsymbol{\sigma}_M = \varepsilon\mathbf{E}\mathbf{E} - \frac{1}{2}\varepsilon(\mathbf{E}\bullet\mathbf{E})\mathbf{I} \tag{2.15}$$

The electrostatic force and torque on the i^{th} particle are given by

$$\mathbf{F}_{\mathrm{E,i}} = \int_{\Gamma_{pi}} \boldsymbol{\sigma}_M \cdot \mathbf{n}_i \, d\mathbf{s} \tag{2.16}$$

$$\mathbf{T}_{E,i} = \int_{\Gamma_{pi}} (\mathbf{x} - \mathbf{x}_i) \times \boldsymbol{\sigma}_M \cdot \mathbf{n}_i \, d\mathbf{s} \tag{2.17}$$

where $\mathbf{n_i}$ is the unit outer normal on the surface of the ith particles and $\mathbf{x_i}$ is the center of the ith particle.

2.2.2 Dimensionless Equations and Parameters

Equations (2.4), (2.5) and (2.7) are nondimensionalized by assuming that the characteristic length, velocity, time, stress, angular velocity and electric field scales are a, U, a/U, $\eta U/a$, U/a and E_0, respectively. The gradient of the electric field is assumed to scale as E_0/L, where L is the distance between the electrodes which is taken to be the same as the domain width. The nondimensional equations for the liquid, after using the same symbols for the dimensionless variables, are:

$$Re\left(\frac{\partial \mathbf{u}}{\partial t} + \mathbf{u} \cdot \nabla \mathbf{u}\right) = -\nabla p + \nabla \cdot \boldsymbol{\sigma} \tag{2.18}$$

$$\nabla \cdot \mathbf{u} = 0 \text{ in } \Omega \setminus \overline{P(t)} \tag{2.19}$$

If the PD approximation is used for evaluating the electrostatic force, the dimensionless equations for the particles become

$$\frac{d\mathbf{U}}{dt}=\frac{6\pi\eta a^2}{mU}\int\left(\frac{-pI+\sigma}{6\pi}\right).n\,ds+\frac{4\pi a^4\varepsilon_0\varepsilon_c\beta|E_0|^2}{mU^2L}\mathbf{E}.\nabla\mathbf{E}+\frac{3\pi\varepsilon_0\varepsilon_c a^3\beta^2|E_0|^2}{4mU^2|r_{ij}|^4}\mathbf{F}_D \tag{2.20}$$

$$I_i\frac{d\boldsymbol{\omega}_i}{dt}=\oint(\mathbf{x}-\mathbf{x}_i)\times\left[(-p\mathbf{I}+\boldsymbol{\sigma}).n\right]dA+\mathbf{T}_{E,i} \tag{2.21}$$

In terms of the Maxwell stress tensor, they are:

$$\frac{d\mathbf{U}}{dt}=\frac{6\pi\eta a^2}{mU}\int\boldsymbol{\sigma}.\mathbf{n}ds\quad+\frac{\varepsilon E_0^2a^3}{mU^2}\int\boldsymbol{\sigma}_M.\mathbf{n}ds \tag{2.22}$$

$$\frac{d\boldsymbol{\omega}}{dt}=\frac{5\eta a^2}{2mU}\int(\mathbf{x}-\mathbf{x}_i)\times\boldsymbol{\sigma}.\mathbf{n}ds\quad+\frac{\varepsilon E_0^2a^3}{mU^2}\int(\mathbf{x}-\mathbf{x}_i)\times\boldsymbol{\sigma}_M.\mathbf{n}ds\,. \tag{2.23}$$

If the PD approximation is used, the above equations contain the following dimensionless parameters:

$$\begin{cases} Re=\dfrac{\rho_L\mathrm{U}a}{\eta} \\ P_1=\dfrac{6\pi\eta a^2}{mU} \\ P_2=\dfrac{3\pi\varepsilon_0\varepsilon_c\beta^2a^3|E_0|^2}{4mU^2} \\ P_3=\dfrac{4\pi\varepsilon_0\varepsilon_c\beta a^4|E_0|^2}{mU^2L} \\ h'=\dfrac{L}{a}. \end{cases} \tag{2.24}$$

From Equation (2.24), Re is the Reynolds number, which determines the relative importance of the fluid inertia and viscous forces, P_1 is the ratio of the viscous and inertia forces, P_2 is the ratio of the electrostatic particle-particle

interaction and inertia forces and P_3 is the ratio of the dielectrophoretic and inertia forces. Another important parameter, which does not appear directly in the above equations, is the solids fraction of the particles; the rheological properties of ER suspensions depend strongly on the solids fraction. Another Reynolds number $Re_L = \frac{\rho_L L U}{\eta}$ is defined based on the channel width L.

If the Maxwell stress tensor approach is used, an alternative parameter $P_E = \frac{\varepsilon E_0^2 a^3}{mU^2}$ is derived; which is a measure of the electrostatic forces, in place of P_2 and P_3. This parameter is less informative than parameters P_2 and P_3, as it does not contain any information about the extent of polarization or the shape of the particle. In flows for which the applied pressure gradient or the imposed flow velocity is zero, a characteristic velocity $U = \frac{2\varepsilon_0 \varepsilon_c \beta a^2 \mid E_0 \mid^2}{3\eta L}$ is assumed; this is obtained by assuming that the dielectrophoretic force and the viscous drag terms balance each other.

In order to investigate the relative importance of the electrostatic particle-particle and dielectrophoretic forces, another parameter is defined:

$$P_4 = \frac{P_2}{P_3} = \frac{3\beta L}{16a}. \tag{2.25}$$

Equation (2.25) implies that if b=O(1) and $L>>a$, and thus $P_4 > 1$, the particle-particle interaction forces will dominate, which is the case in most applications of dielectrophoresis. On the other hand, if $b<<$O(1) and $\frac{L}{a} \sim$O(1), and thus $P_4 < 1$, then the dielectrophoretic force dominates.

2.3 Finite Element Method

The computational scheme developed here is based on a combined weak equation of motion for the fluid and particles which eliminates the hydrodynamic forces and torques, as they are internal to the combined system [24-27]. These combined equations of motion are solved on the fluid-solid domain using the distributed Lagrange multiplier method (DLM) in which the motion inside the particle boundaries is forced to be rigid-body motion using a distribution of Lagrange multipliers. The Maxwell stress tensor method is used for computing the electrostatic forces acting on the particles. The time integration is performed using the Marchuk-Yanenko operator splitting technique, which is first-order accurate [26]. The domain is discretized using a tetrahedral mesh where the velocity and pressures fields are discretized using P2-P1 interpolations and the electric potential is discretized using P2 interpolation.

2.4 Simulation Conditions

In the study, the finite element code is tested by performing direct numerical simulations of the transient motions of two spherical particles in a 3-dimensional rectangular channel in a non-uniform electric field. Two different configurations of electrodes placement in the channel walls are simulated; the one-sided configuration and the dielectrophorectic cage, or "DEP Cage", configuration.

In the one-sided configuration, two equally-spaced electrodes are embedded onto one side wall parallel to yz-coordinate plane of the channel, see Figure 2.1. The electrodes are placed such that the wall's centerline is equidistant from that of the electrodes. In order to generate non-uniform electric within the channel, the electrodes are made shorter than the side wall, so that they do not cover the side wall completely when they are embedded. Also the electrodes are placed such that they do not affect the fluid boundary conditions. To maintain uniform electric field in the y-direction, the width of electrodes in the y-direction is made to the domain width.

For the dielectrophorectic cage configuration, the cage is formed by embedding four electrodes in the four side walls parallel to the *yz*- and xy-coordinate planes of the rectangular channel, as shown in Figure 2.4. The

electrodes are placed at the center of the side walls and their width is one-and-a-half the length of the sides.

The fluid density $\rho_L = 1.0$ g/cm^3, and the particles are assumed to be neutrally buoyant. The viscosity of the fluid is $\eta = 0.01$ g/cm.s. Both particles and fluid are assumed to be non-conducting. The normalized dielectric constant of particles is varied and that of the fluid is assumed to be unity. The voltage applied to the electrodes is 1000 V. All dimensional lengths reported in this chapter are expressed in mm and the time is reported in seconds. The initial fluid and particle velocities are set to zero. The no-slip boundary condition is imposed on the domain side walls.

The domain dimensions are L, L/2 and L along the x-, y- and z- axis, respectively, as shown in Figure 2.1. All lengths are nondimensionalized using L. Also, note, there are two characteristics length scales in this problem: the particle radius and the distance between the particles. The latter in general is related to the concentration of the particles in the device, which is not important since for most cases considered in this thesis there are only 2 particles in the domain. The particles shown in following figures are for visualization and are larger than the circles shown.

2.5 Results and Discussion

2.5.1 Domain with the Electrodes Mounted on a Side Wall

The magnitude of electric field **E** in the xz-plane at the domain mid plane is shown in Figure 2.1. The electric field distribution is for the case when there are no particles in the domain. From the figure, the electric field distribution inside the channel is non-uniform. As explained earlier, in a non-uniform electric field, the particles are subjected to two main electrostatic forces; the particle-particle interaction and the dielectrophoretic force. Thus, their transient motions depend on the magnitudes and directions of $\boldsymbol{E}$ and $\boldsymbol{E}.\boldsymbol{\nabla E}$. directions of $\boldsymbol{E}$ and $\boldsymbol{E}\cdot\boldsymbol{\nabla E}$, and also on the particles positions relative to the electric field direction. The dimensionless parameters for the case presented are: Re= $6.52\text{x}10^{-1}$, P_E= $7.47\text{x}10^{1}$, and $P_4 = 1.17\text{x}10^{-1}$.

In Figure 2.1(a), it can be noticed that the electric field magnitude decreases farther away from the electrodes' wall. Figure 2.1(b) shows that the lines of gradient of the electric field magnitudes point toward the electrodes, in the direction normal to the isovalues of $\boldsymbol{E}.\boldsymbol{\nabla E}$. Therefore, due to the proportionality relationship between the dielectrophoretic force and gradient of electric field, if a particle is placed in this domain and its dielectric constant is smaller than that of the liquid, it will experience a dielectrophoretic force directed away from electrodes;

which is in the direction opposite to the lines of gradient of the electric field magnitude. If the dielectric constant of the particle is greater than that of the liquid, it will experience a dielectrophoretic force toward the wall of the electrodes, as indicated by the arrows in Figure 2.1(b). Note: particle's dielectric constant has been normalized with respect to the ambient liquid. Thus, a particle is taken to be positively polarized if $\varepsilon_p > 1$ and negatively polarized if $\varepsilon_p < 1$.

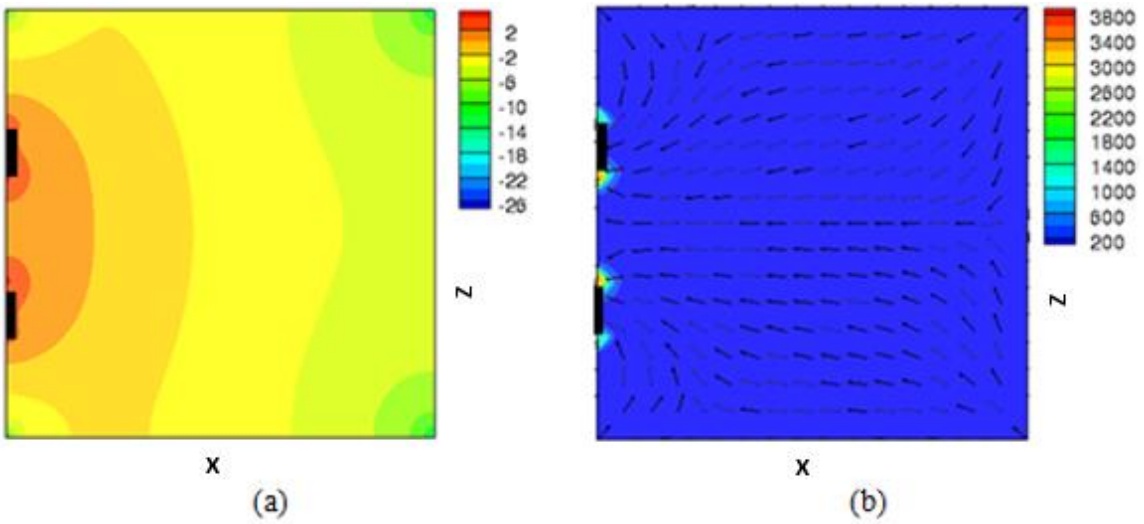

Figure 2.1 Electric field distribution. (a) Isovalues of log|**E**| at y = 0.25, i.e., the domain mid plane. The electric field does not vary with y. The magnitude is maximal near the electrode edges and decreases with increasing distance. (b) Magnitude and direction of $\nabla \mathbf{E}^2$ to which the dielectrophoretic force is proportional. Arrows indicate the direction of positive DEP force (for negative DEP, the direction is the opposite).

2.5.2 Motion of Two Particles

The transient motion of the two particles within the non-uniform electric field is analyzed to better understand the degree of influence each of the two electrostatic

forces. The initial positions of the two particles are (0.2, 0.25, 0.88) and (0.5, 0.25, 0.88), and their diameter is 0.2. Figure 2.2 shows the transient motion of the two particles. The locations of the particles at selected time-steps are color-coded to track the movement of each particle using RYGB, with red signifying the starting position and blue signifying the resting position. In the simulation, the two particles move toward each other due to particle-particle interaction, and at the same time, each particle moves toward the electrode due to dielectrophoretic force. Based on the trajectory of each particle, the first particle, i.e. the one on the left, reaches the electrode wall much faster, as clearly shown by the yellow circles. A reasonable explanation to this is that, even initially, the left particle is acted upon by a greater dielectrophoretic force, due to its proximity to the electrode. As shown in Figure 2.1, the gradient of the electrics field is significantly higher near the electrodes than anywhere else in the domain. Thus, as the distance between the two particles and the electrode decreases, the dielectrophoretic force dominates the particle-particle interaction force. This causes the left particle to be collected at the electrode much faster. However, although the second particle started-out slowly due to small dielectrophoretic force acting on it, it picks up speed at it approaches the electrode, due to the presence of the first particle that has already been

collected and the significant dielectrophoretic force it now experiences near the electrode.

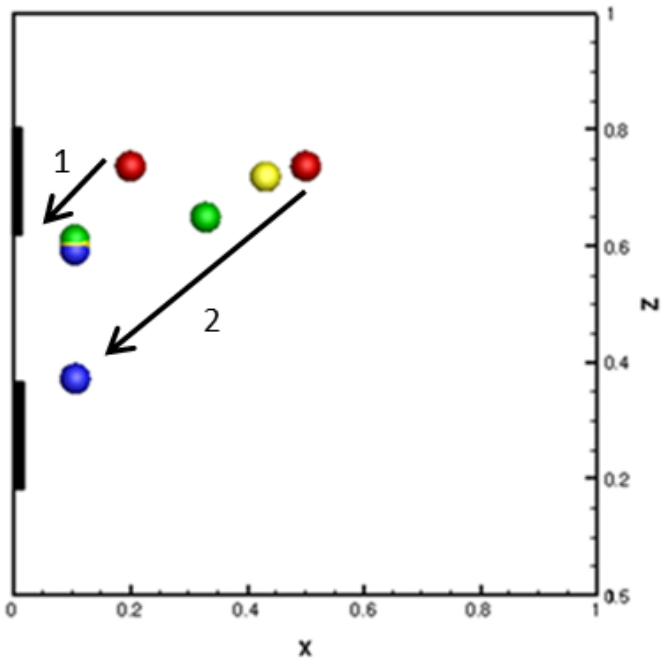

Figure 2.2 The front view of the two particles for $\varepsilon_p = 1.2$. The initial positions of the two particles are (0.2, 0.25, 0.88) and (0.5, 0.25, 0.88). The initial positions are shown in red, while the final positions are shown by black circles.

2.5.3 Convergence Study

To show that the numerical results obtained using the MST method converge when the time-step size is reduced or the mesh resolution is refined, a convergence study is performed on both the mesh resolution and the time-step size.

For the mesh refinement, simulations were performed on two mesh sizes; one with 139425 nodes and the other with 269001 nodes. The times-step size used for these different simulations is 1.0 x 10^{-4} s.

For the time-step, simulations were performed for two different values of time-step size; which are 0.5 x 10^{-4} and 2x10^{-4} s. The number of velocity nodes for the two time-step sizes is 139425.

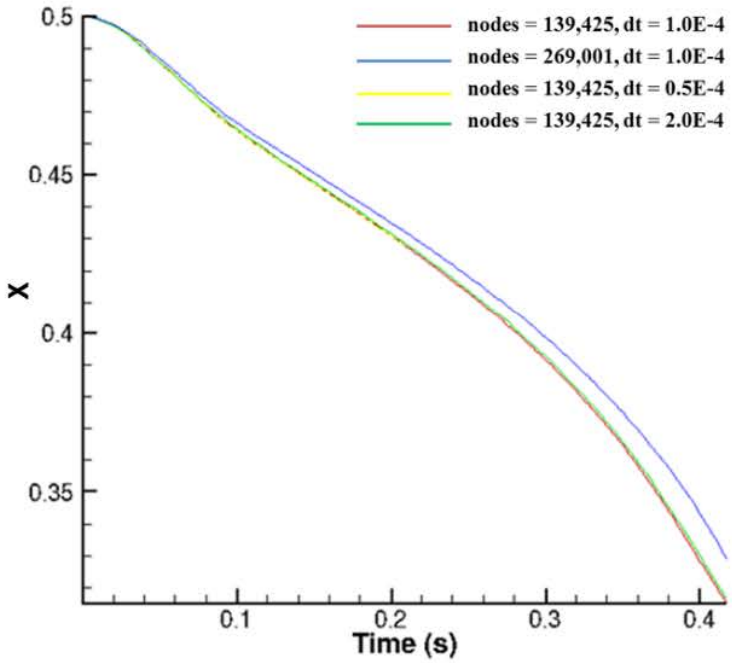

Figure 2.3 The x-coordinate of the transient motion of the first particle as a function of time taken for the case of the two different mesh resolutions and the two time-step sizes.

Figure 2.3 shows a plot of the x-coordinate of the transient motion of the first particle as a function of time taken for the case of the two different mesh resolutions and the two time-step sizes. The initial positions of the two particles are (0.2, 0.25, 0.88) and (0.5, 0.25, 0.88). From the figure, the trajectories of the particle remain virtually unchanged when the time step is reduced. Also, the change is insignificant when the mesh is refined. The slight change in trajectory for

the refined mesh can be attributed to the mesh's ability to resolve the electric field distribution better than the coarse mesh; which is mostly the case for DNS study. However, the difference in the trajectories of the two mesh resolutions is virtually insignificant, as seen in Figure 2.3. Thus, it can be concluded that the results are independent of further mesh refinement and time-step reduction.

2.5.4 Motion in a Dielectrophoretic Cage

This dielectrophoretic cage configuration is of practical interest because it provides a way to trap one or more particles at the center of the channel in a contactless fashion. The magnitude of the electric field **E** in the xz-plane at domain mid plane as shown in Figure 2.4. It can be observed that the local minimum of the electric field magnitude is at the center of the domain, and the field magnitude increases with increasing distance from the center. The Figure 2.4 also shows that the electric field inside the cage is non-uniform, and its gradient near the domain center is non-zero, except at the center itself where it is zero. Figure 2.4(b) shows that the gradient of the electric field magnitude points radially outward from the center and towards the edges of the electrodes. Therefore, if a particle is placed in this domain and its dielectric constant is smaller than that of the liquid, it will experience an electric force towards the center of the domain, i.e., in the direction opposite to the lines of the gradient of the electric field magnitude. If the dielectric

constant of the particle is greater than that of the liquid, the direction of the electric force is away from the center.

For the dielectrophoretic cage configuration, the motion of the two particles under the influence of positive and negative dielectrophoresis is examined. The dielectric constant ε_p of the particles is varied such that for $\varepsilon_p > \varepsilon_c = 1$, the particles collect in the region where the magnitude of the electric field is locally maximal, which is generally on the electrode edges, and for $\varepsilon_p < \varepsilon_c = 1$, the particles collect at the region where the electric field magnitude is locally minimal.

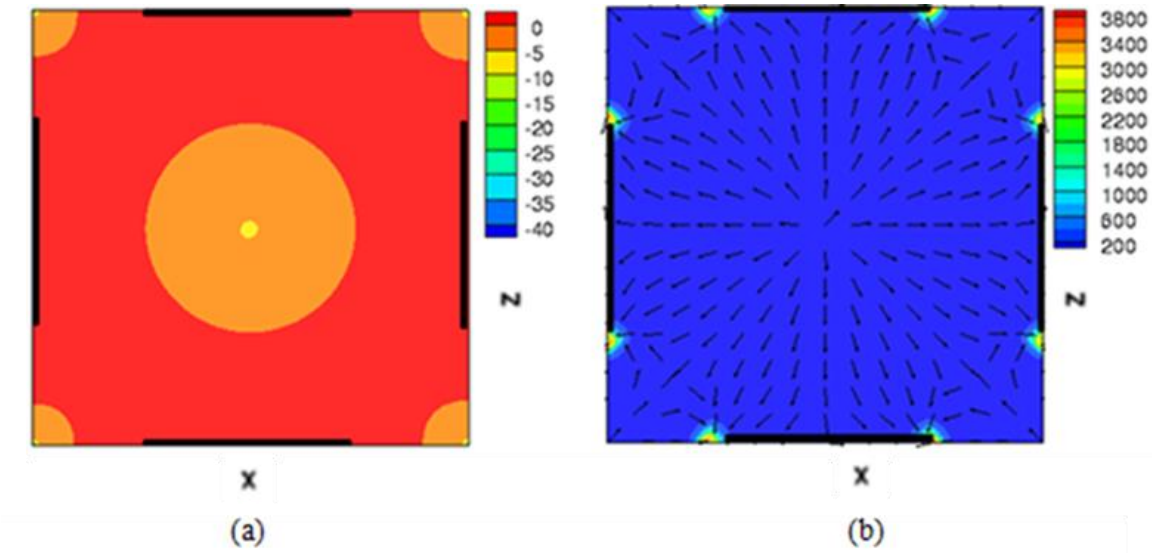

Figure 2.4 Electric field distribution. (a) Isovalues of $\log|\mathbf{E}|$ at y = 0.25, i.e., the domain mid plane. Electric field does not vary with y. The magnitude is maximal near the electrode edges and decreases with increasing distance. The minimum is at the center. (b) Magnitude and direction of $\nabla\mathbf{E}^2$ to which the dielectrophoretic force is proportional. Arrows indicate the direction of positive DEP force (for negative DEP, the direction is the opposite.

2.5.5 Positive Dielectrophoresis $\varepsilon_p = 1.2$

First, the case where the dielectric constant of the particles is greater than that of the suspending fluid has been studied. Figure 2.5 shows transient motions of the two particles under positive dielectrophoresis for four different initial positions. The locations of the particles at selected time-steps are color-coded using RYGB to track the movement of each particle, with red signifying the starting position and blue signifying the resting position. The locations of the particles at selected time-steps are color-coded using RYGB colors to track the movement of each particle, with red signifying the starting position and blue signifying the resting position. In Figure 2.5, the two particles are all collected at the nearby electrode for all four test cases. In the setup, the dimensionless parameters are: Re= $6.52\text{x}10^{-1}$, P_E= $7.47\text{x}10^{1}$, and $P_4 = 1.17\text{x}10^{-1}$.

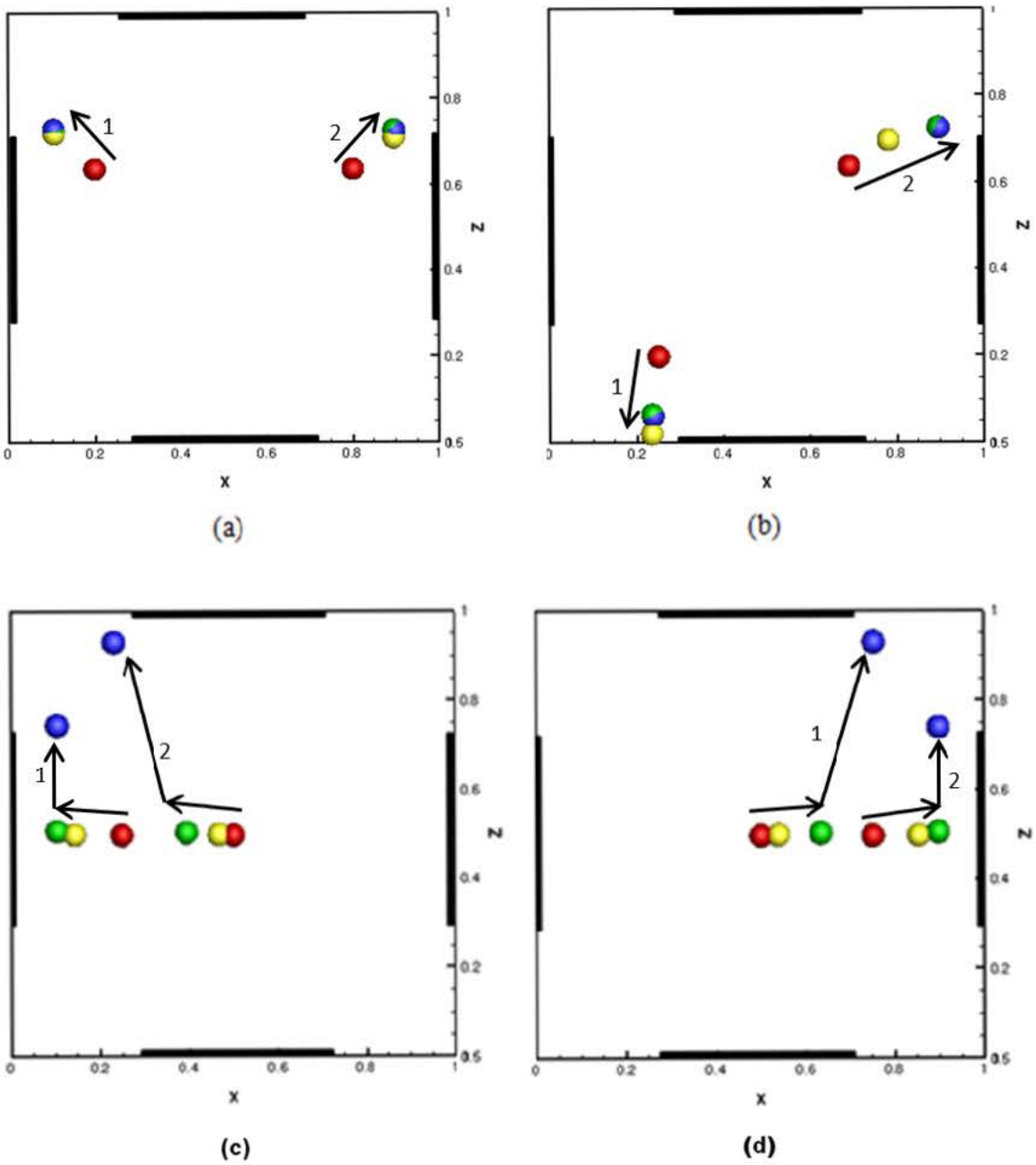

Figure 2.5 Transient motions of the two particles under the influence of positive dielectrophoresis. The initial positions of the two particles are (a) (0.2, 0.25, 0.65) and (0.8, 0.25, 0.65), (b) (0.25, 0.25, 0.2) and (0.5, 0.25, 0.65), (c) (0.25, 0.25, 0.50) and (0.5, 0.25, 0.50, (d) (0.50, 0.25, 0.50) and (0.75, 0.25, 0.50).

Notice that a particle can be collected at a different electrode edge other than the nearby electrode edge, due to the influence of electrostatic particle-

particle interaction force; which, for most of the time, is responsible in determining the final position of a particle between two nearby electrodes edges. For instance, in Figure 2.5(c) and Figure 2.5(d), the final position of the particle, with initial positions at the center of the plane, is dictated by the initial position of the second particle. From Figure 2.5, the particle at the center of the plane is trapped since the gradient of electric field is zero at the location; which means that the dielectrophoretic force on the particle is zero. Thus, the electrostatic particle-particle force pulls the trapped particle in the direction of the second particle, after which dielectrophoretic force starts to act on the freed particle.

2.5.6 Negative Dielectrophoresis $\varepsilon_p = 0.2$

This section describes the case where $\varepsilon_p = 0.2$. All other parameters, including the domain size and the initial particles positions for the four test cases shown in Figure 2.6, are the same as for the case of the positive dielectrophoresis described in Section 2.5.6. For this case, dimensionless parameters are: Re= $5.62\text{x}10^{-2}$, P_E= $1.67\text{x}10^{3}$, and $P_4 = 6.82\text{x}10^{-1}$.

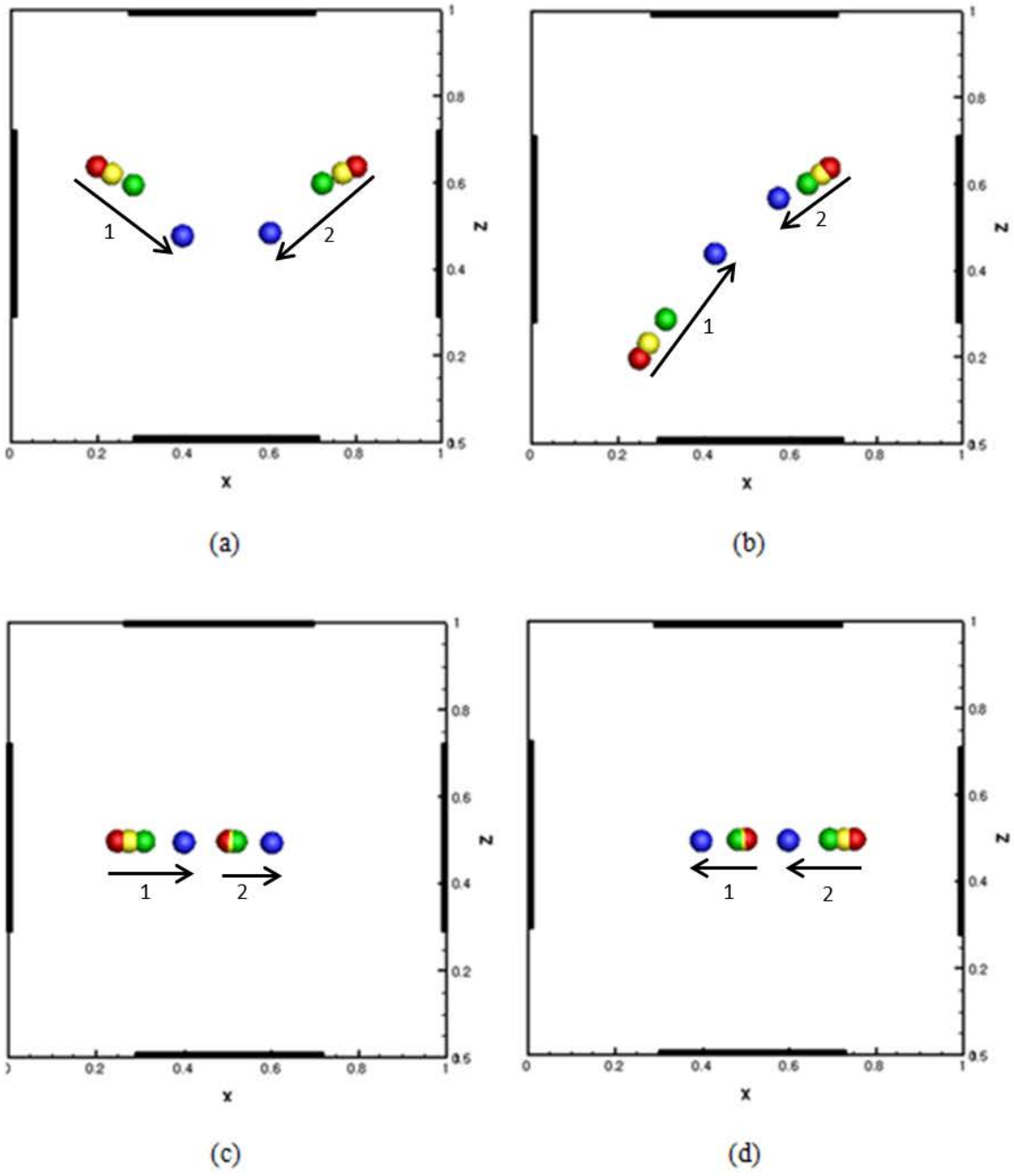

Figure 2.6 Transient motions of the two particles under the influence of negative dielectrophoresis. The initial positions of the two particles are (a) (0.2, 0.25, 0.65) and (0.8, 0.25, 0.65), (b) (0.25, 0.25, 0.2) and (0.5, 0.25, 0.65), (c) (0.25, 0.25, 0.50) and (0.5, 0.25, 0.50, (d) (0.50, 0.25, 0.50) and (0.75, 0.25, 0.50).

As expected, the motion of the particles in this case, even at early times, is quite different from the case where ε_p is positive. The particles move toward the

center where the electric field magnitude is locally minimal. From Figure 2.6, it can be observed that for each test case, the particles move toward the center of the domain in the direction opposite to their nearest line of gradient of the electric field magnitude. Even after being collected at the center of the domain, the particles are still oriented in the direction of particular lines of gradient; which is reasonable since the dielectrophoretic force acts along lines of gradient. Thus, this explains the reasons why the particles are oriented differently at the center for the four test cases.

2.5.7 Motion of Single Particle: PD and MST Comparison

The PD and MST results are compared for the motion of a single particle in the cage. The plots in Figure 2.8 compare quite nicely to the position plots. The offset in the velocity plots can be attributed to the point-dipole method approximations; which are contrary to the observation in Figure 2.7(b), whereby the presence of a particle modifies the electric field.

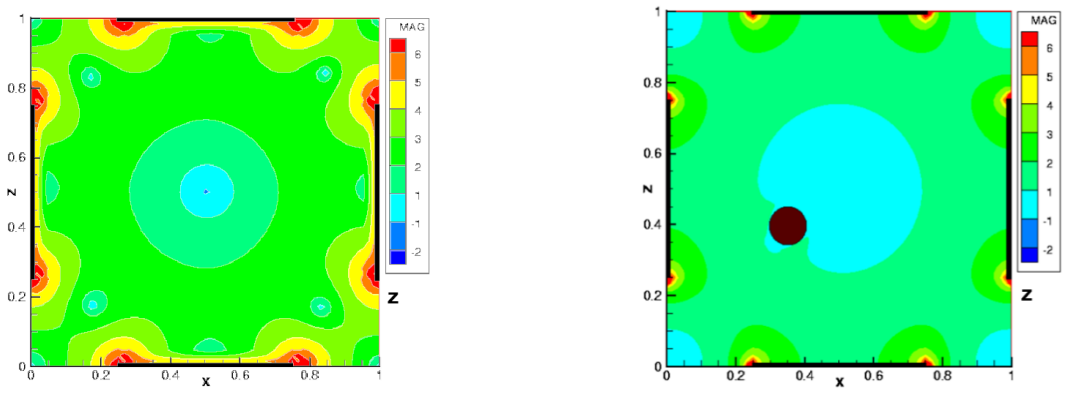

(a) (b)

Figure 2.7 Isovalues of log|**E**| at y = 0.25, i.e., the domain mid plane: (**a**) Without a particle and (**b**) With a particle. The dimensionless parameters are: Re= $1.13\text{x}10^{-1}$, P_E= $3.08\text{x}10^{3}$, and P_4 = $6.68\text{x}10^{-1}$.

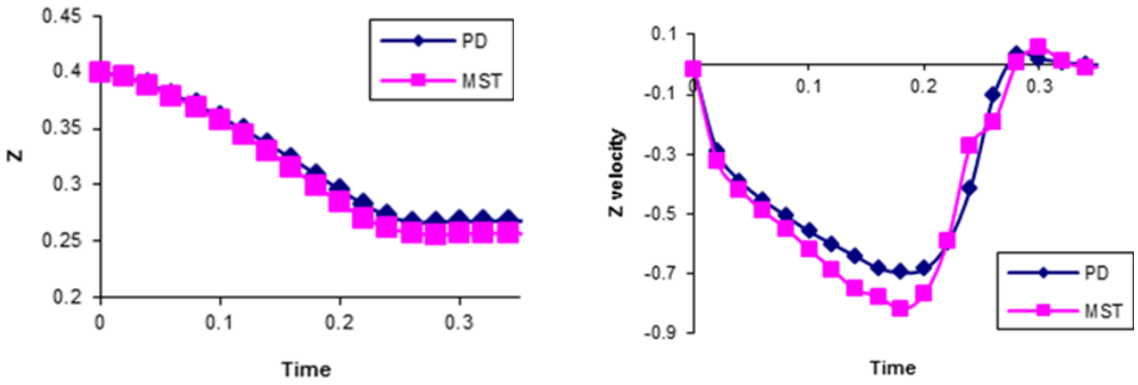

(a) (b)

Figure 2.8 The z-component of particle position computed using the PD and MST methods for a = 0.05 and ε_p=1.5. The initial particle position is (0.35, 0.25, and 0.40), and (a) Position and (b) Velocity.

2.6 Summary

A numerical scheme based on the distributed Lagrange multiplier method is used to study the dynamical behavior of particles in a dielectrophoretic cage. The Maxwell stress tensor method is used for computing the electric forces on the particles. We find that the error in the point-dipole method increases as the distance between the particles decreases. Also, the error is relatively large when the particle radius is comparable to the "cage" size, which determines the length scale over which the electric field varies. The error also increases as the difference between the dielectric constants of the particles and the fluid increases. The final steady positions of the particles, including the orientations of the line joining their centers, for the MST method are different from those for the point-dipole method.

CHAPTER 3

ELECTROHYDRODYNAMIC MANIPULATION OF PARTICLES ADSORBED ON THE SURFACE OF A DROP

3.1 Introduction

Considerable attention has been given in recent years to understand the behavior of particles trapped at fluid-fluid interfaces because of the importance in a wide range of applications, e.g., the self-assembly of particles resulting in novel nano structured materials, micro/nano manufacturing, formation of Janus particles, the stabilization of emulsions, etc.[30-36].

The use of particle stabilized emulsions has increased in the food, biomedical and materials industries since they offer many advantages over those stabilized using surfactants [37-38]. For example, colloidal particles at the interface can be manipulated using external magnetic or electric fields [39,81-90,115], as done in this dissertation, or by changing the temperature or the pH. The latter has been exploited to control particle stabilized capsules for controlled and targeted release of drugs. pH responsive particles can stabilize or destabilize emulsions depending on the pH value. Also, in biomass refining reactions, particles at the liquid interfaces can serve the dual purpose of stabilizing emulsions and acting as a catalyst [40]. Future progress in this area will critically depend upon our ability to

understand and accurately control the particle arrangement for a broad range of particles of various types, sizes and shapes [41,42].

It is known that a drop placed in a uniform electric field, under perfect dielectric conditions, deforms into an axisymmetric ellipsoid (prolate shape), with the major axis aligned along the direction of the field [43,44,116]. The degree of deformation depends on the electric Weber number, which compares the stress due to electric field to interfacial tension between the two fluids. It was shown by Allen and Mason [43] and by Taylor [44] that there is a critical Weber number at which drops break apart or tip-stream.

However, under a leaky dielectric condition, where either or both fluids are weakly conducting, a drop can deform to a prolate or to an oblate shape. Deformation of a drop to an oblate shape has been noted to be due to a small but finite electrical conductivity of the fluids [43-47,90-110]. Due to this conductivity, charge migration to the drop's surface creates a transverse electric stress imbalance, which generates an electrohydrodynamic (EHD) flow inside and outside of drop. The direction of the EHD flow depends on the ratios $R_r = \frac{R_d}{R_s}$, and $q = \frac{k_d}{k_s}$, where R_d and R_s are respectively the drop and ambient liquids resistivities, while k_d and k_s are dielectric constants of the drop and ambient liquids, respectively. When the EHD flow is from equator-to-pole the drop deforms to a prolate shape

and when the EHD flow is from pole-to-equator deforms to an oblate shape. The former is the case when $R_r q > 1$ and the latter is the case when $R_r q < 1$. The drop does not deform for $R_r q = 1$, since there is no induced flow in this case. This flow has been exploited in several recent studies to manipulate the distribution of adsorbed particles [25-26,48-49,110-114]. Particles collect at the poles when the EHD flow is from equator-to-pole and at the equator when the EHD flow is from pole-to-equator. The poles are defined as the two points on the drop which are nearest to the electrodes, and the equator is the curve at equidistance from the poles.

It has been shown that particles distributed on the surface of a perfectly dielectric drop immersed in a perfectly dielectric liquid can be concentrated at its poles or the equator by subjecting it to a uniform electric field, [2,50-52], and that this method can be used to separate on the surface of a drop those particles experiencing positive dielectrophoresis from those experiencing negative dielectrophoresis. The approach works also when the liquids are weakly conducting, provided an ac electric field of sufficiently large frequency is used. In this dissertation, the frequency of an electric field is shown to be an important parameter which can be used to adjust the intensities of the DEP and EHD flow

induced forces on surface-absorbed particles, and thus control their distribution on the surface.

The key idea behind this study is that, under leaky dielectric conditions, surface-adsorbed particles can be effectively controlled by varying the frequency; by being able to move them to the poles or equator by applying electric fields with different frequency regimes. The EHD flow decays with increasing frequency and so the EHD flow induced drag force decreases with increasing frequency. The DEP force acting on particles depends on the real part of the Clasius-Mossati factor which varies relatively slowly with frequency. Therefore, there exists a critical frequency above which the DEP force dominates. A possible application is that when the two forces are directed in the opposite directions the approach can be used to move particles to poles or equator by tuning to the right frequency regime. The approach is superior to traditional dielectrophoresis since the critical frequency is a function of particle and fluids properties and the frequency can be varied easily which makes the approach easier to implement.

The discussion is organized as follows: first, the various forces that act on an adsorbed particle are described, which is followed by a description of the experimental procedure, and then there will be a presentation of results.

3.2 Drop in AC Electric Fields

Torza *et al.* used the leaky dielectric model to calculate the axisymmetric flow induced outside and inside of a drop in an ac electric field [47]. The focus of this work is on the tangential component of the flow on the surface of the drop which can cause particles adsorbed on the surface to move towards the poles or the equator. The tangential velocity contains a steady component and a periodic component. The frequency of the latter is twice the frequency of the applied ac electric field. The periodic component causes particles to oscillate back and forth and so does not cause a net displacement. The steady component of the velocity on the surface of the drop which causes particles to collect at the poles or the equator (in spherical coordinates) is given by [47]

$$U_S = \frac{18\varepsilon_0 k_s E_0^2 b R_r \left(R_r q - 1\right)}{20\mu_s \left(1+\lambda\right)\left(2R_r + 1\right)^2 + a^2\omega^2\left(q+2\right)^2} \sin\theta\cos\theta \tag{3.1}$$

and the periodic component is given by

$$U_T = U_S \frac{\sqrt{R_r^{\,2} + a^2\omega^2}}{R_r} \cos\left(2\omega t + \alpha\right) \tag{3.2}$$

where ε_0 is the permittivity of free space, E_0 is the amplitude of the ac electric field, b is the drop's radius, μ_s is the ambient liquid viscosity, λ is the drop to ambient liquid viscosity ratio, ω is the angular frequency of the field, $a = \varepsilon_0 R_d \mathrm{k}_s$,

and θ is the azimuthal angle. The value and sign of α is defined by these expressions:

$$\sin\alpha = \frac{a\omega}{\sqrt{R_r^{\,2} + a^2\omega^2}} \frac{(2R_r+1)(1-2qR_r-2R_r) - a^2\omega^2(q+2)^2}{(2R_r+1)^2 + a^2\omega^2(q+2)^2} \tag{3.3}$$

$$\cos\alpha = \frac{1}{\sqrt{R_r^{\,2} + a^2\omega^2}} \frac{(2R_r+1)^2 R_r - a^2\omega^2(q+2)(R_r q - 2R_r - 2)}{(2R_r+1)^2 + a^2\omega^2(q+2)^2} \tag{3.4}$$

Notice that the sum of the steady and unsteady components changes direction during each period as the amplitude of the unsteady component is larger than that of the steady component. However, when $a\omega$ is much smaller than R_r, the amplitude of the periodic component is approximately equal to the steady component, and so when the steady and unsteady components are in the same direction the net flow becomes about twice as large as the steady component and about zero when they are in the opposite directions. On the other hand, when $a\omega$ is comparable or larger than R_r, the amplitude of the periodic component can be much larger than the steady component, and so the velocity changes direction during each period. Thus, in the former case, the EHD flow causes particles adsorbed on the surface to move approximately steadily towards the poles or equator. In the latter case, they reverse direction for a part of the period, but the net motion during each period is towards the poles or equator depending on the

direction of the steady component. The interfacial force keeps adsorbed particles on the surface as they move along the surface because of the flow.

The flow causes a particle adsorbed on the surface to experience a drag force in the direction tangential to the interface. This electrohydrodynamic (EHD) flow induced drag can be computed using Stokes' law, since the velocity magnitude is relatively small, and it is given by

$$F_{eh} = 3\pi(\mu_d + \mu_s)R(U_S - U_p). \tag{3.5}$$

Notice that the EHD drag is computed in terms of the steady component U_S of the EHD velocity since it alone causes a net displacement of the particle. The fluid viscosity is taken to be the average viscosity of the ambient liquid and the drop liquid, R is the particle radius, and U_p is the particle velocity. Assuming that the particle velocity is zero, using Equation (3.1) and (3.5) gives

$$F_{eh} = \frac{27\pi k_s \varepsilon_0 E_0^2 bRR_r (R_r q - 1)}{10(2R_r + 1)^2 + a^2\omega^2 (q+2)^2} \sin\theta\cos\theta. \tag{3.6}$$

Notice that the force decreases with increasing electric field frequency and increases with increasing drop radius and increasing electric field strength. For the cases considered in this chapter, it was the dominant force at small frequencies. Therefore, at small frequencies, the final location of particles adsorbed on the

surface of a drop was determined by the direction of the EHD force. The strength of EHD flow diminishes with increasing frequency since it takes a finite amount of time for charges to migrate to the surface. Equation (2.6) also implies that the EHD force is zero both at the poles $(\theta = 0, \pi)$ and at the equator $(\theta = \frac{\pi}{2})$, and maximum at $\theta = \frac{\pi}{4}$.

3.2.1 Dielectrophoretic Force on Adsorbed Particles

A particle adsorbed on the surface is also subjected to a DEP force and to a buoyant weight. The DEP force becomes dominant when the frequency is increased above a critical value and the electric field strength is sufficiently large such that it is larger than the buoyant weight. The point-dipole (PD) approximation can be used to obtain an expression for the dielectrophoretic (DEP) force that acts on a particle of radius R trapped on the surface of a spherical drop of radius b [50]. The tangential component of the DEP force (in spherical coordinates) is given by the following expression:

$$F_{DEP,\theta} = -12\pi R^3 \frac{1}{b} \varepsilon_0 k_s E_0^2 \beta' \beta(2+\beta) \cos\theta \sin\theta \tag{3.7}$$

Here, $\beta(\omega) = Re\left(\frac{\varepsilon_d^* - \varepsilon_s^*}{\varepsilon_d^* + 2\varepsilon_s^*}\right)$ is the drop's Clausius-Mossotti factor, and $\beta'(\omega) = Re\left(\frac{\varepsilon_p^* - \varepsilon_s^*}{\varepsilon_p^* + 2\varepsilon_s^*}\right)$ is the particle's Clausius-Mossotti factor with respect to the outer fluid. ε_p^*, ε_d^* and ε_s^* are the frequency dependent complex permittivities of the particle, the drop and ambient fluids, respectively. The complex permittivity $\varepsilon^* = \varepsilon - j\sigma/\omega$, where ε is the permittivity, σ is the conductivity and $j = \sqrt{-1}$. The above expression is also valid for a dc electric field in which case $\boldsymbol{E}_0$ denotes the electric field intensity. Notice that the magnitude of force on a particle of given radius increases with decreasing drop size. Particles trapped on the interface also interact with each other via the dipole-dipole (D-D) forces [2,54-57], which are not included in Equation (3.7). The PD model accurately predicts the DEP and D-D forces for small particles at small concentrations, but for larger particles, numerical computations based on the Maxwell stress tensor needs to be conducted to obtain accurate estimate of the force [58].

Equation (3.7) implies that the DEP force is zero both at the poles $(\theta = 0, \pi)$ and at the equator $(\theta = \frac{\pi}{2})$, and maximum at $\theta = \frac{\pi}{4}$. Furthermore, it implies that if $\beta\beta' > 0$, particles aggregate at the poles because they are in a

state of stable equilibrium at the poles, and if $\beta\beta' < 0$ they aggregate at the equator where their equilibrium is stable as shown in Figure 3.1(b).

3.2.2 Total Force on Adsorbed Particles

The total tangential force acting on a particle can be obtained by adding the force contributions given by Equations (3.6)-(3.7), and the buoyant weight of the particle

$$F_t = \left[\frac{27\pi R_r \left(R_r q - 1\right)}{10\left(2R_r + 1\right)^2 + a^2\omega^2\left(q+2\right)^2} \left(\frac{b}{R}\right) - \left(\frac{R}{b}\right) 12\pi\beta'\beta\left(2+\beta\right) \right] R^2 \varepsilon_0 k_s E_0^2 \sin\theta\cos\theta + \frac{4}{3}\pi R^3 (\rho_p - \rho_d) \mathrm{f}_b \sin\theta \tag{3.8}$$

where f_b is the buoyancy coefficient which accounts for the fact that the particle is partially immersed in both ambient and drop liquids. In the absence of a strong electric field, the buoyant weight of the particle determines its position on the drop's surface. Notice that the three contributions may not be in same direction and that the total tangential force can be towards or away from the poles. We considered particles both denser than the ambient liquid and less dense than the ambient liquid. In the former cases, particles sedimented to the bottom surface of the drops, and in the latter cases, particles rose to the top surface of the drops. In

a strong electric field such that the buoyant force was relatively small compared to the electric force terms, the latter determined the location where particles collected.

From Equation (3.8), we note that the EHD contribution decreases with decreasing $\frac{b}{R}$, but the DEP contribution increases with decreasing $\frac{b}{R}$. The EHD contribution also decreases with increasing frequency as $\frac{1}{\omega^2}$, whereas the DEP contribution varies only because β and β' vary with ω. For the cases considered in this chapter, β and β' varied slowly with ω, but their variations were negligible.

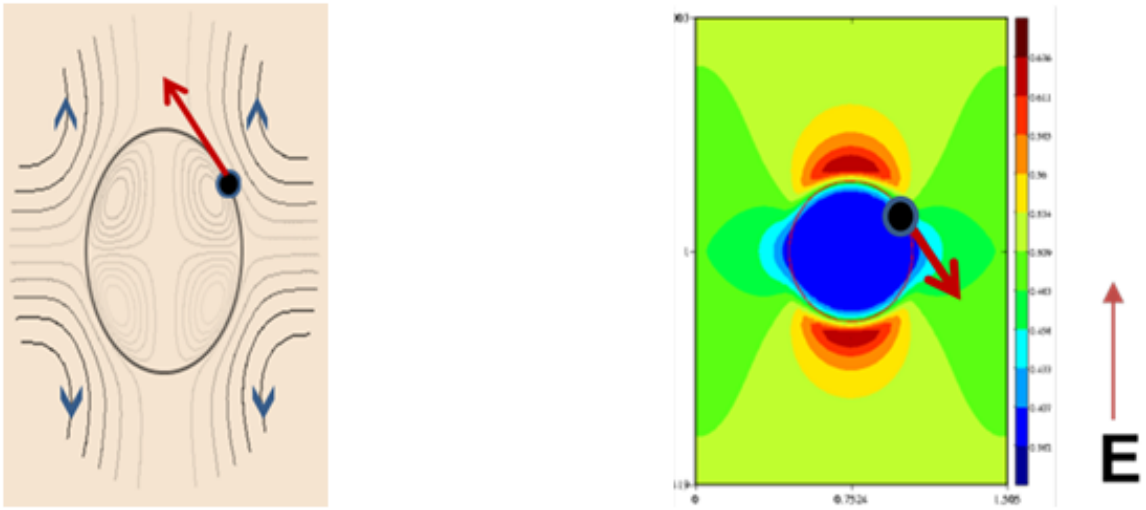

(a) $(R_r q < 1)$ (b) $(\beta\beta' < 0)$

Figure 3.1 Streamlines of EHD flow in a leaky dielectric fluid which determine the direction of EHD force and isovalues of electric field intensity which determine the direction of DEP force: (a) streamlines of EHD flow for $R_r q < 1$, (b) isovalues of the electric field intensity around a drop subjected to a uniform electric field generated by the electrodes placed at the top and bottom of the domain for $\beta\beta' < 1$ (see ref. [16] for details). Notice that the EHD and DEP forces are not in the same direction.

Therefore, there is a critical frequency (ω_c) such that below it the EHD force dominate and above it the DEP force dominate. The equilibrium location of a particle depended on the direction of the dominant force. At small frequencies, the first term in the square brackets of Equation (3.8) was larger, and so, it determined where the particles adsorbed on the surface of a drop would collect. Above the critical frequency, the second term became the dominant term, and so it determined where the particles collected. The critical frequency is given by

$$\omega_c = \left(\frac{1}{a^2 (q+2)^2} \frac{9R_r (R_r q - 1)}{4\beta\beta'(2+\beta)} \left[\left(\frac{b}{R} \right)^2 - \frac{40\beta\beta'(2+\beta)}{9R_r (R_r q - 10)} (2R_r + 1)^2 \right] \right)^{\frac{1}{2}} \tag{3.9}$$

This dependence on the frequency of ac electric field can be exploited to manipulate particles on the surface of drop. Notice that the critical frequency for a given drop and ambient fluid combination is not fixed, as it also depends on the ratio $\frac{b}{R}$.

The drop and ambient liquids properties determine the direction of circulating flow. For $R_r q < 1$, the direction of the EHD flow is from equator to pole, and for $R_r q > 1$, it is from pole to equator. The DEP force moves particles to either pole or equator depending on the sign of the factor $\beta\beta'$, see Figure 3.1, and it is the dominant force at frequencies above the critical value. If the DEP and

EHD forces are in the same direction, the net force acting on particles does not change direction when the frequency is increased above the critical frequency. But, when the DEP and EHD forces are not in the same direction, the direction of the net force changes and this can be used to move particles as well as separate particles for which the critical frequencies are different.

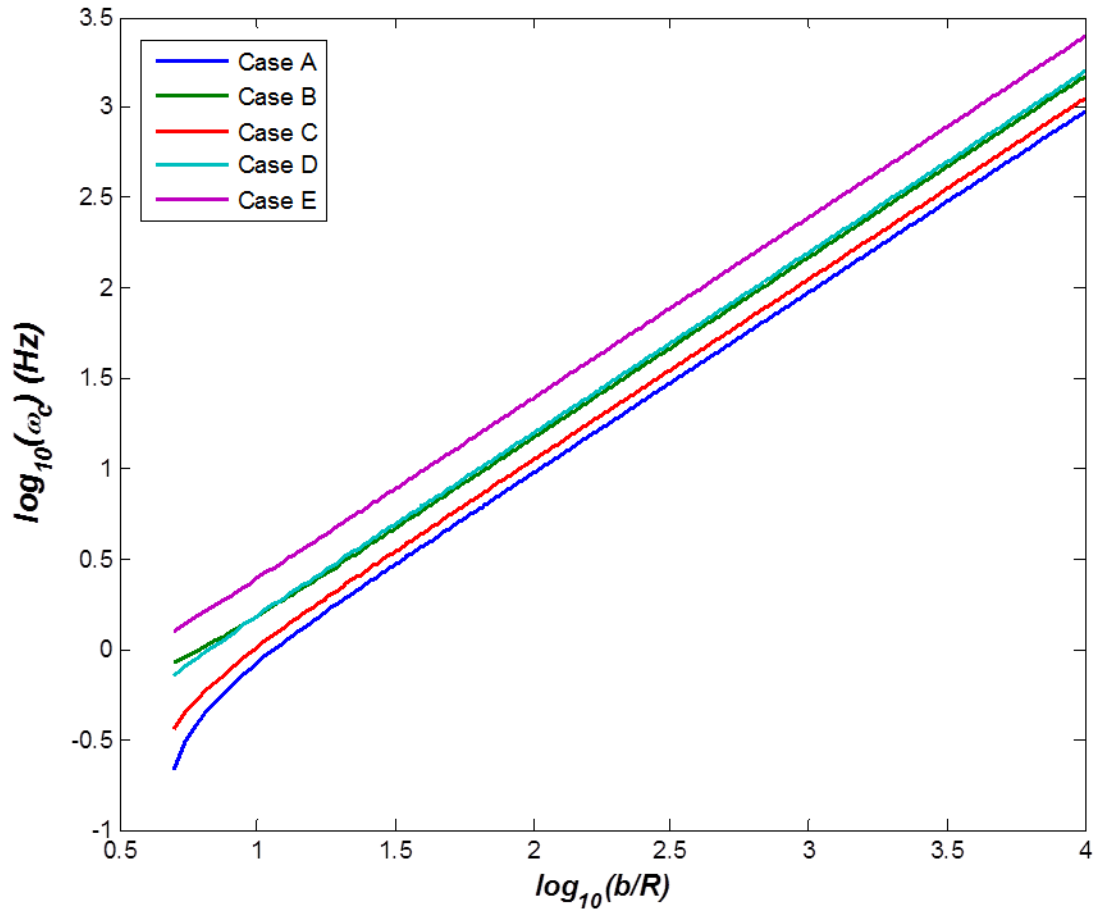

Figure 3.2 The critical frequency at which the EHD and DEP forces are equal as a function of $\frac{b}{R}$ for cases A-E described in Table 3.3.

The properties of the liquids and particles considered in our experiments are described in Tables 3.1-3.3. We considered five liquid-particle combinations which

are denoted as cases A-E. The properties for cases A, C and D were such that the EHD and DEP forces were in the opposite directions, and for cases B and E those two forces were in the same direction. The dependence on the critical frequency, ω_c, for these cases is shown in Figure 3.2. The parameter $\frac{b}{R}$ was varied between 5 and 10^4. The Figure shows that the critical frequency increases with increasing $\frac{b}{R}$. The EHD force varies directly with $\frac{b}{R}$ whereas the DEP force varies inversely with $\frac{b}{R}$. Therefore, if the particle radius is kept constant and the drop radius is decreased, the DEP force increases while the EHD force decreases. For the DEP force to dominate the EHD force at a fixed $\frac{b}{R}$, the EHD force can be reduced by increasing the frequency. Thus, the frequency of the electric field is a convenient control parameter. Furthermore, larger particles have a lower ω_c than smaller particles, and thus they can be separated by varying the frequency even when they are of the same type.

3.3 Experimental Setup

Experiments were conducted in a rectangular prism-shaped device shown in Figure 3.3. The voltage was applied using transparent electrodes placed on the top and bottom surfaces so that the motion of particles could be monitored using a microscope camera. The electric field inside the device was uniform and in the

vertical direction. The distance between the electrodes was 5.5 mm, which was the same as the depth of the ambient liquid. An insert which matched the dielectric properties of the ambient fluid was placed at the bottom of the device to help maintain uniform electric field. A variable frequency ac signal generator (BK Precision Model 4010A) was used along with a high voltage amplifier (Trek Model 5/80) to apply voltage to the electrodes. The motion/deformation was recorded using a digital color camera connected to a Nikon Metallurgical MEC600 microscope.

The drop and ambient liquids were chosen so that the drop density was slightly larger, which ensured that the drop did not float or move freely. The properties of the liquids are shown in Table 3.1 (as provided by the supplier). A drop with particles distributed on its surface was formed using the following procedure. The first step was to form a dilute suspension by mixing particles in the liquid that was to be used to form the drop. Concentration of particles in the suspension was kept small to ensure that the concentration of particles on the surface of the formed drop was small. Drops of various sizes were formed at a small distance from the bottom surface by injecting a given amount of the drop liquid into the ambient liquid with a micropipette. Since the drop liquid was denser than the ambient liquid, the drop, along with particles inside the drop, sedimented to

the bottom surface. The bottom surface and the drop were in contact along an approximately circular contact line as seen through the microscope. We then waited several minutes until all particles suspended inside the drop reached either the bottom or the top surface of the drop, depending on the density of the particles compared to that of the drop. Once a particle was confined at the two-fluid interface, it remained confined at the interface due to the interfacial tension, even when the electric field was switched on. The position of a particle within the interface was determined by the three-phase contact angle on its surface and its buoyant weight.

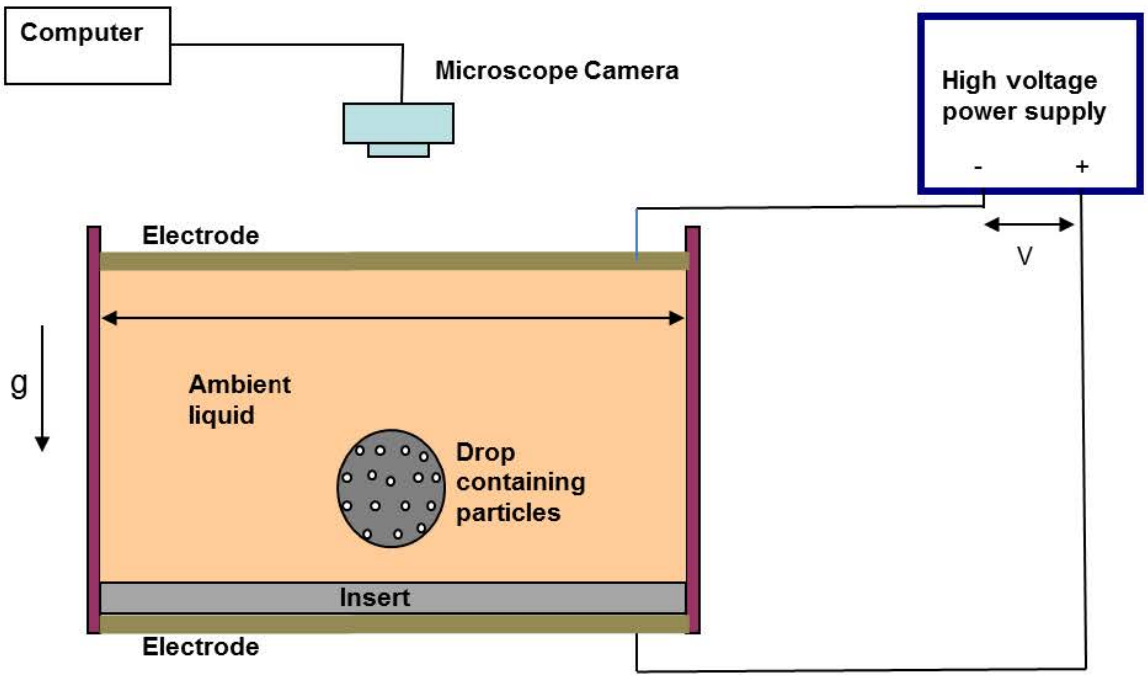

Figure 3.3 A schematic of the setup used in our experiments. The electrodes were mounted on the top and bottom of the device. The resulting electric field was in the vertical direction.

Table 3.1 Liquid Properties

Liquid	**Density** $\boldsymbol{\rho}$ $(\mathrm{kg\,m^{-3}})$	**Viscosity** μ $(\mathrm{Pa\,s})$	**Dielectric constant** k_p	**Conductivity** σ $(\mathrm{S\,m^{-1}})$	**Supplier**
Castor oil	961	1	4.7	32×10^{-12}	Sigma-Aldrich, (83912)
Silicone-I oil	1270	0.30	6.85	56×10^{-12}	Dow Corning, (FS 1265)
Silicone-II oil	960	0.05	2.75	3.6×10^{-12}	United Chemical Technology (UCT), (PS040)

Table 3.2 Properties of the particles used in experiments.

Type	**Density** ρ_p $(\mathrm{kg\,m^{-3}})$	**Diameter** $2r$ $(\mu\mathrm{m})$	**Dielectric constant** k_p	**Supplier**
Soda lime glass	2500	$1-3$	6.9	MO-SCI, (GL-0191)
Hollow glass	600	$6-32$	1.2	Potters Industries, (60P18)
Polystyrene	1000	4	2.0	Invitrogen, (580/605)

*Particles were approximately spherical in shape

Table 3.3 Properties for the cases considered in our experiments

	Case A	**Case B**	**Case C**	**Case D**	**Case E**
Ambient liquid	castor oil	castor oil	castor oil	castor oil	castor oil
Drop liquid	silicone oil-I	silicone oil-I	silicone oil-I	silicone oil-II	silicone oil-II
Particle	Hollow glass	Soda lime glass	Polystyrene	Hollow glass	Soda lime glass
$R_r q$	0.832	0.832	0.832	5.20	5.20
β	0.132	0.132	0.132	-0.160	-0.160
β'	-0.330	0.135	0.237	-0.330	0.135
$\beta\beta'$	-0.044	0.018	-0.031	0.053	-0.022

3.4 Results

As discussed on Section 3.2, an EHD flow arises on the surface of a drop suspended in an ambient fluid when it is subjected to a uniform ac electric field. The flow is driven by an electric stress imbalance on the surface that arises because of the accumulation of electric charge on the surface. The particle laden drops in our experiments were denser than the ambient liquids and so they along with the suspended particles settled to the bottom of the device and formed a contact line with the bottom surface. Thus, the EHD flow near the bottom surface was weaker and particles could not migrate to the bottom pole since the velocity on the drop's surface surrounded by the contact line, which was in contact with the bottom surface, was zero. Although the presence of a solid boundary altered the EHD flow around the drop, there was a poles-to-equator or equator-to-poles EHD flow depending on the properties of the drop and ambient liquid similar to that for a freely suspended drop.

Our aim is to study how this flow and the DEP force influence the distribution of particles adsorbed on the surface of the drop. As the drops in our experiments were stationary on the bottom surface, we were able to observe the migration of particles adsorbed on their surfaces under the action of an applied electric field over longer periods of time compared to that for the case of

approximately matched density where the drop slowly sediments in the ambient liquid. The motion of an adsorbed particle consisted of steady and time periodic components as the EHD flow and the electric field intensity were time periodic. Furthermore, the particles adsorbed on the surface also moved because the drop shape pulsated with time. The size of the drop, the properties of the liquids, and the electric field intensity determined the strengths of the periodic and steady flow components. The EHD flow and the pulsations of the drop shape diminished as the frequency of electric field was increased.

3.4.1 Drops Containing a Single Type of Particles

We first describe the results for the cases in which only one type of particle was present. We considered the five different combinations of liquids and particles described in Table 3.3. These cases were selected to understand the dependence of the distribution of adsorbed particles on the frequency of electric field. The EHD flow for cases A, B, and C was towards the poles. The DEP force for case B was also towards the poles, but for cases A and C, it was towards the equator. For cases D and E, the EHD flow was towards the equator. For case D, the DEP force was towards the poles and for case E it was towards the equator.

The critical frequency for the cases considered in our experiments was O(10-100), and so the frequency was varied between 0.01 to 1000 Hz. The periodic

component of flow varied with a frequency that was twice the frequency of the applied electric field. Since the critical frequency (ω_c) depends on the particle size, when particles were not monodispersed there was a range of ω_c; for smaller particles, ω_c was larger and for larger particles ω_c was smaller. Similarly, non-spherical particles moved to the equator or the poles depending on the direction of the net force which depended on their size.

3.4.1.1 Silicone Oil-I Drop in Castor Oil. We first discuss cases A, B and C which have silicone oil-I as the drop liquid and castor oil as the ambient liquid. For this liquid combination, the EHD flow was towards the poles. This is in agreement with Equation (3.1) since for this case $R_r q < 1$. Thus, at small frequencies particles migrated to the poles because the drag due to the EHD flow was the dominant force. The critical frequencies for the three types of particles depended on the properties of the liquids and particles, and $\frac{b}{R}$. Above the critical frequency, the motion of particles was dominated by the DEP force.

In case A, the silicone oil-I drop contained hollow glass particles which were less dense than the drop and ambient liquids. Thus, initially, before the field was applied, particles rose to the top of the drop. The diameter of the silicone oil drop in Figure 3.4 was approximately 436 μm. Taking a mean particle size of 18 μm, our theoretical analysis predicted $\omega_c = 2.12$ Hz. After a voltage was applied at a

frequency less than about 2 Hz, the EHD drag dominated the DEP force for all particle sizes. Below this critical frequency, particles were drawn towards the pole since the direction of flow circulation was equator-to-pole, as shown in Figure 4(b). The frequency in Figure 4(b) was 0.4 Hz. The particle velocity contained a steady component and a periodic component.

The strength of the EHD flow diminished with increasing frequency. When the frequency was larger than about 2 Hz, the DEP force started to dominate the EHD flow induced drag for the larger sized hollow glass particles causing them to move towards the equator. Since $\beta\beta'$ was negative, this implied that the DEP force was greater than the EHD flow induced drag. However, only when the frequency was increased to about 5 Hz smaller particles moved to the equator. This can be seen in Figure 3.4(e) where the dimensionless radius of the region around the pole within which particles were confined is plotted as a function of the frequency. Notice that the radius increases with increasing frequency as particles progressively move towards the equator. This is a consequence of the fact that when the DEP and EHD forces exactly balance each other the buoyant weight of particles cannot be neglected. The tangential component of the buoyant weight which is zero at the poles increases as a particle moves towards the equator, and therefore the DEP force must overcome this increase in the buoyant weight. The DEP and EHD

forces also vary with the angular position but they have a different functional dependence (see Equation (3.8)).

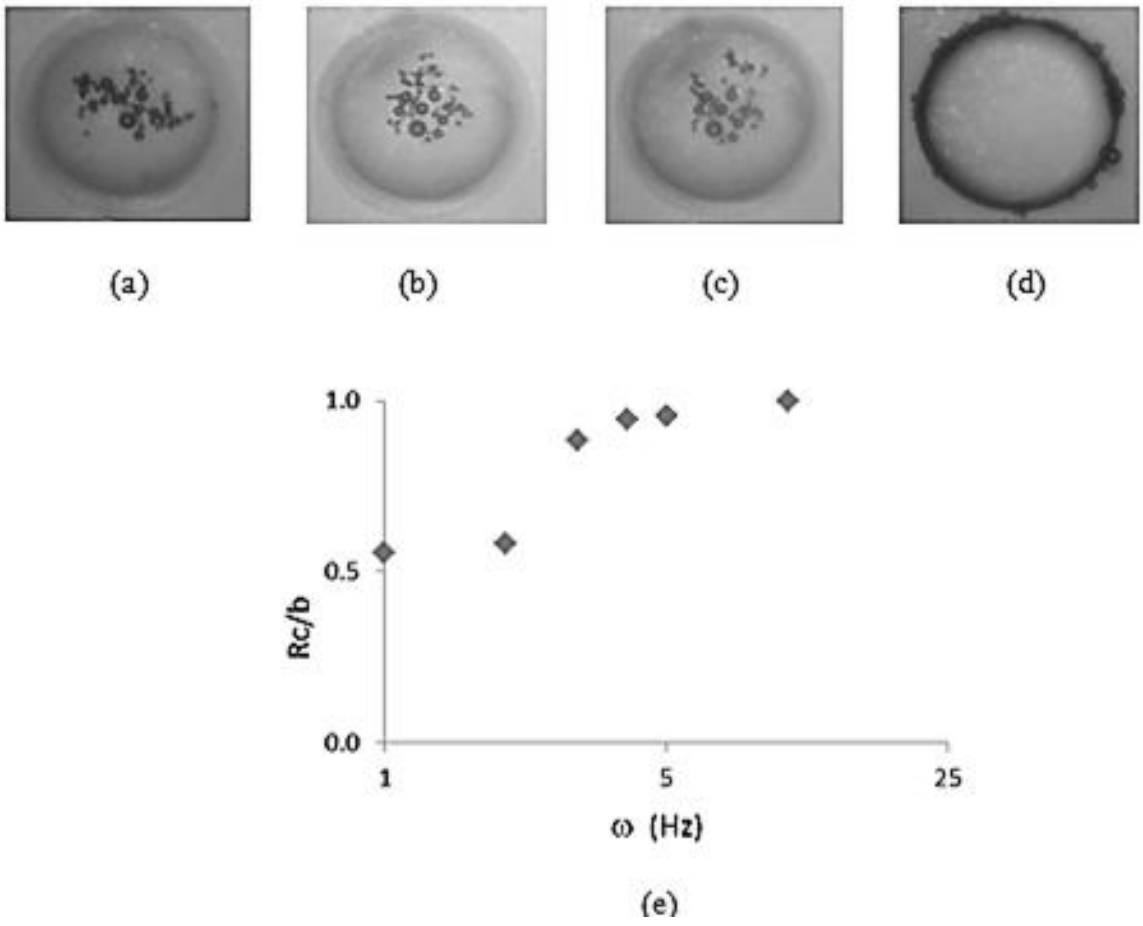

Figure 3.4 Distribution of hollow glass particles on silicone oil-I drop in castor oil. The mean particle diameter was 18 μm and the drop diameter was 436 μm. The voltages and frequencies were (a) 0 V; (b) 2000 V at 0.4 Hz; (c) 3000 V at 3 Hz; (d) 3000 V at 20 Hz; (e) the radius of the region around the equator within which particles were confined (Rc) nondimensionalized with the drop radius is shown as a function of the frequency.

In case B, the silicone oil drop contained spherical soda lime glass particles which were denser than the drop and ambient liquids. Thus, particles sedimented

to the bottom of the drop, as shown in Figure 3.5. The diameter of the drop was approximately 400 μm. After a voltage was applied, as shown in Figure 3.5, particles collected at the poles at both low and high frequencies. This was because the EHD flow was from equator to pole, and so it dragged particles to the poles. In addition, since $\beta\beta' > 0$, the DEP force also moved particles to the poles. Therefore, at higher frequencies, particles continued to collect at the poles as the two forces were directed toward the poles. An increase in the frequency above the critical value did not change the distribution since the direction of the net force on the particles did not change. Using a mean particle diameter of 2 μm, our analysis predicted that the critical frequency at which the DEP force became the dominant force was around 33.0 Hz, but this could not be measured experimentally as the EHD flow and the DEP force were in the same direction. However, unlike in the EHD flow dominated regime, the DEP force moved particles to poles in a steady manner, without a significant periodic component.

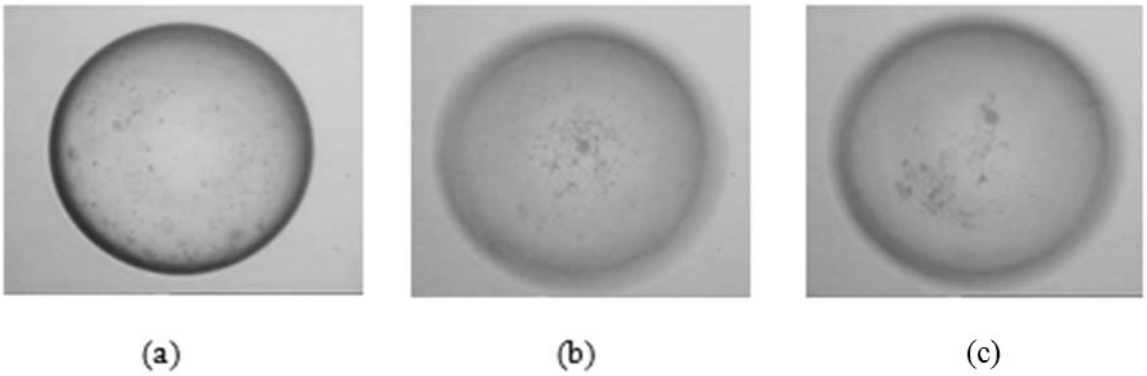

Figure 3.5 Distribution of soda lime glass particles on silicone oil-I drop in castor oil. The mean particle diameter was about 2 μm and the drop diameter was 400 μm. Particles appear as small dots in the photographs due to their small size. Particles collected at the poles as both the DEP and EHD forces are towards the poles. The voltages and frequencies are (a) 0 V; (b) 2 kV at 0.4 Hz; and (c) 3 kV at 60 Hz. In (b) and (c), particles collected at the poles.

Next, we describe case C for which the silicone oil drop contained polystyrene particles which were denser than silicone oil-I and so they sedimented to the bottom of the drop. The diameter of the silicone oil drop in Figure 3.6 was approximately 400 μm. After a voltage was applied at small frequencies, the EHD flow induced drag dominated and so particles were drawn towards the poles. The critical frequency in this case was around 10 Hz, above which the DEP force dominated. Since $\beta\beta' < 0$, particles were moved from the pole to the equator, as shown in Figure 3.6(b). In comparison to the experimental value, our theoretical analysis predicted $\omega_c = 15.8$ Hz.

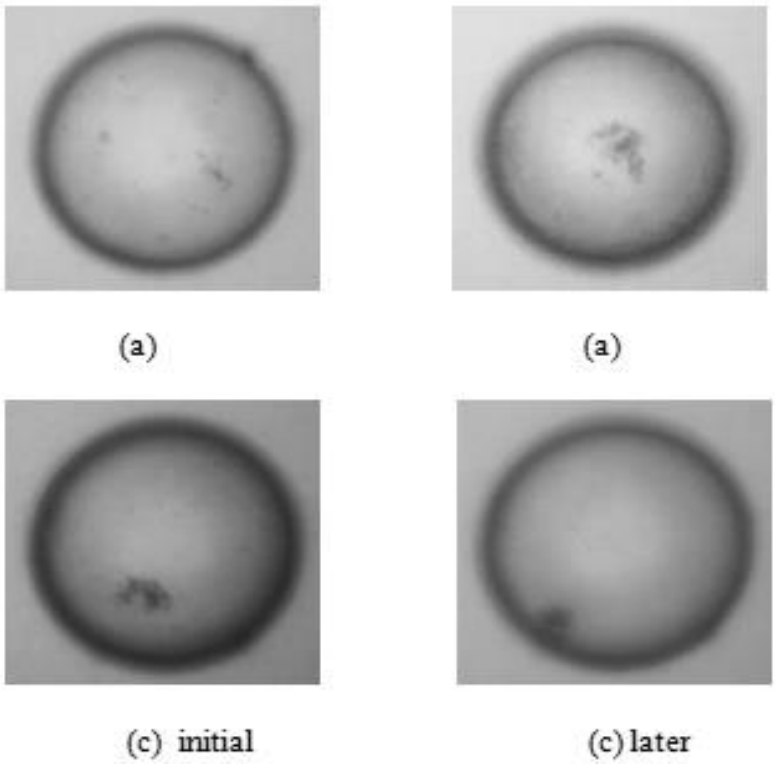

Figure 3.6 Distribution of polystyrene particles on silicone oil-I drop in castor oil. The mean particle diameter was 4 μm and the drop diameter was around 400 μm. Due to their small size, particles appear as dots in the images. The voltages and frequencies are (a) 0 V; (b) 4 kV at 4 Hz; (c) 4 kV at 40 Hz. The two photographs show particles migrating towards the equator.

It is noteworthy that the critical frequency for case A was about 2 Hz, but for case C, it was about 15.8 Hz. This is due to the fact that the size of hollow glass particles was larger and the critical frequency decreases with increasing particle size (see Figure 3.3). Also, the critical frequency depends on the value β' for the particle which was different for hollow glass particles and polystyrene particles.

3.4.1.2 Silicone Oil-II Drop in Castor Oil. For cases D and E, silicone oil-II was used as the drop liquid and castor oil as the ambient liquid. Unlike the cases discussed in the previous subsection, for these cases $R_\tau q > 1$ since the two silicone oils have different physical properties. Thus, the EHD flow was towards the equator, and so at small frequencies for which the EHD flow provided the dominant force particles migrated to the equator. Also, as before, the motion of particles towards the equator had a steady and a periodic component. Both of these components diminished as the frequency was increased.

In case D, a silicone oil-II drop with hollow glass particles was suspended in castor oil. Initially, hollow glass particles rose to the top of the drop, since they were less dense, as shown in Figure 3.7(a). The diameter of the drop was approximately 400 μm.

Figure 3.7(b) shows a snapshot of the particles as they moved from the poles to the equator at a frequency of 0.2 Hz. This was due to the fact that the EHD flow in this case was from poles-to-equator. In Figure 3.7(b), particles have moved to the equator, but are not clearly visible because of the drop's curvature. We observed that below ~ 10 Hz, the EHD flow induced drag force was the dominant force and so all particles were dragged towards the equator.

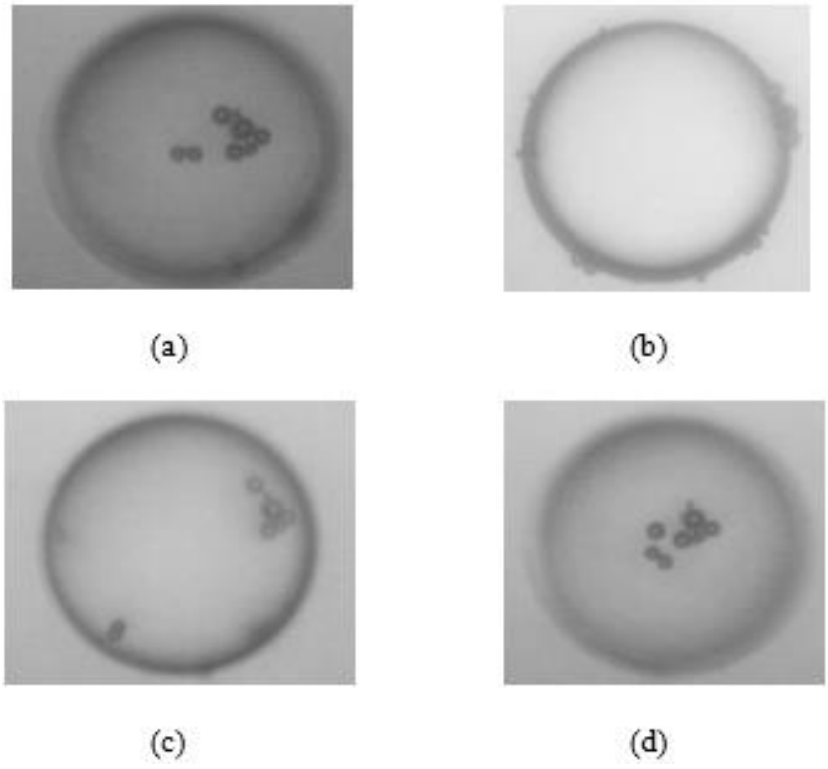

Figure 3.7 Distribution of hollow glass particles on silicone oil-II drop in castor oil. The mean particle diameter was 18 μm and the drop diameter was around 400 μm. The voltages and frequencies were (a) 0 V; (b) 3 kV at 0.2 Hz; (c) 3 kV at 16 Hz; (d) 8 kV at 20 Hz.

The value of $\beta\beta'$ for hollow glass particles was positive and so the DEP force was towards the poles. Thus, above **10 Hz**, for which the DEP force became the dominant force, all particles were dragged towards the poles. Figure 3.7(c) shows that particles moved away from the equator when the frequency was increased to 16 Hz. Our theoretical analysis predicted ω_c to be 7.65 Hz for a mean particle size of 18 μm (Note that the hollow glass particles were not

monodispersed). Figure 3.7(d) shows that particles moved to the poles when the frequency was 20 Hz.

For case E, the silicone oil-II drop contained soda lime glass particles. Initially, before an electric field was applied, the particles sedimented to the bottom surface of the drop, as shown in Figure 3.8(a). The diameter of the drop was approximately 430 μm. The EHD flow and the DEP forces in this case were in the same direction, i.e., from pole-to-equator. Therefore, as can be seen in Figures 3.8(b) and 3.8(c), the particles moved towards the equator for both low and high frequencies. According to our analysis the critical frequency at which the DEP force became the dominant force was around 110 Hz, but this could not be verified experimentally, as the two forces were in the same direction.

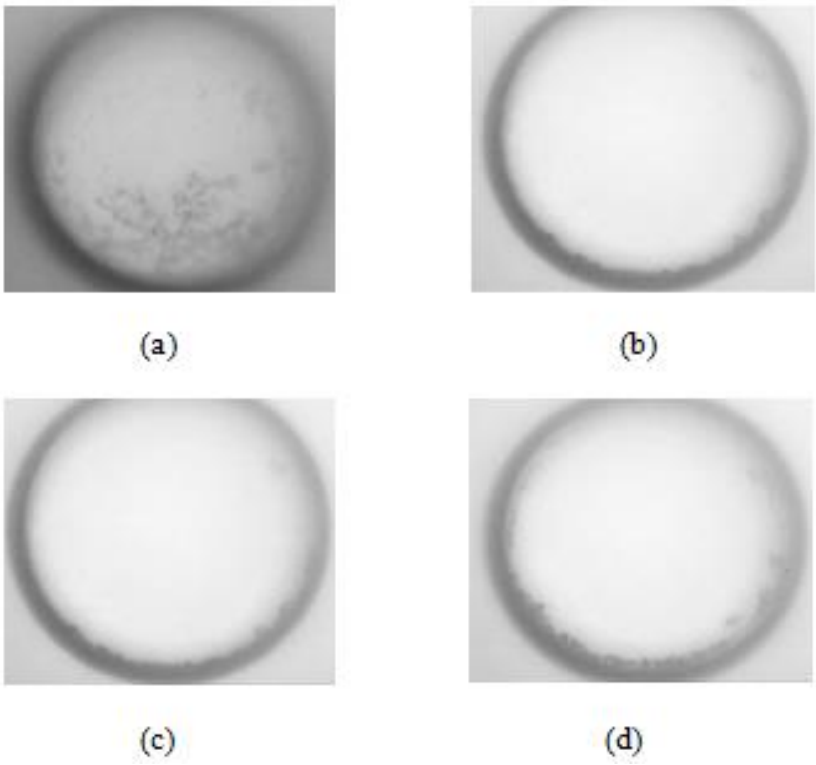

Figure 3.8 Distribution of solid glass particles on silicone oil-II drop in castor oil. The mean particle diameter was 4 μm and the drop diameter was around 430 μm. Due to their small size, particles appear as dots in the images. The voltages and frequencies are (a) 0 kV; (b) 2 kV at 0.2 Hz; (c) 4 kV at 1 Hz; (d) 4 kV at 120 Hz. The photographs show that in (b) – (d) particles collected at the equator.

An increase in the frequency above the critical value did not change the distribution since the direction of the net force on the particles did not change. In this sense, this case was similar to the case reported in Figure 3.5, where position of the particles did not change when the frequency was increased above the critical value. Particles collected at the poles for both low and high frequencies. The values of $R_r q$ and $\beta\beta'$ for the two cases were such that the EHD and DEP forces acted from equator-to-pole in Figure 3.5 and from pole-to-equator in Figure 2.8.

3.4.2 Drop Containing Two Types of Particles

We next consider cases in which two different types of particles were placed on the surface of a drop. First, we consider the case of a silicone oil-I drop in castor oil. The aim was to determine when the two types of particles can be separated and concentrated in different regions on the surface of the drop by adjusting the frequency of electric field. This is analogous to fractional distillation of a mixture into its components parts based on their boiling points. But, in this case, particles are separated based on their critical frequencies.

3.4.2.1 Silicone Oil-I Drop with Mixture of Spherical Hollow Glass Particles and Polystyrene Particles in Castor Oil. A silicone oil-I drop, with mixture of hollow glass particles and polystyrene particles, was suspended in castor oil as shown in Figure 3.9. The diameter of the drop was approximately 410 μm. Initially, prior to the application of electric field, both hollow glass particles and polystyrene particles rose to the drop's top surface since they were less dense than the drop.

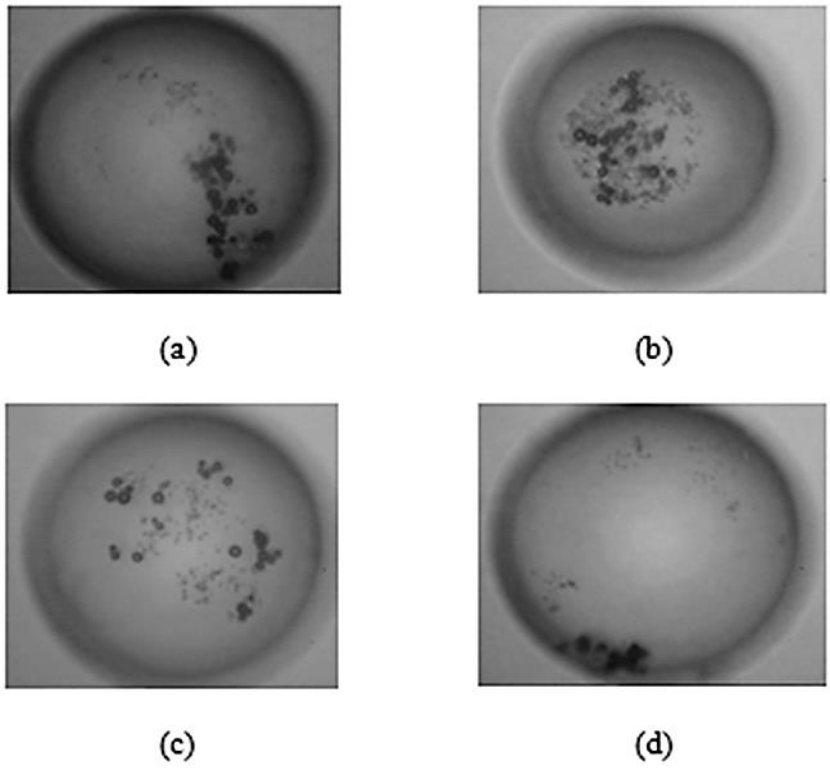

Figure 3.9 Distribution of a mixture of hollow glass and polystyrene particles on a silicone-I oil drop immersed in castor oil. The mean diameter of glass and polystyrene particles was 18 μm and 4 μm, respectively, and the drop diameter was 410 μm. The voltages and frequencies were (a) 0 V; (b) 2.5 kV at 0.1 Hz; (c) 3 kV at 6 Hz (d) 3 kV at 20 Hz.

After a voltage was applied at a frequency of 0.1 Hz, as shown in Figure 3.9, particles collected at the poles. This was because the EHD flow was directed from equator to pole, and so it dragged both types of particles to the poles. This case was interesting because $\beta\beta' < 0$ for both type of particles and so the DEP force caused particles to move towards the equator, but the two types of particles had different critical frequencies. From Subsection 3.4.1.1, we know that the critical

frequency at which the DEP force became the dominant force was about 2.12 Hz for hollow glass particles and about 15.8 Hz for polystyrene particles.

Thus, when the frequency was increased to 6 Hz the hollow glass particles began moving to the equator, but the polystyrene particles remained at the poles. When the frequency was increased to 20 Hz, above the critical frequency of about 15.8 Hz for polystyrene particles, the polystyrene particles also started to move towards the equator and both types of particles collected at the equator. This shows that the frequency of the applied electric field can be used to selectively move particles to the different regions on the surface of a drop.

3.4.2.2 Silicone Oil-I Drop with Mixture of Spherical Hollow Glass Particles and Soda Lime Glass Particles in Castor Oil. We next considered the case of silicone oil-I drop with a mixture of hollow glass particles and soda lime glass particles suspended in castor oil. The diameter of the drop was approximately 430 μm. The aim was to separate the two types of particles from each other by varying the frequency. This case is different from the previous case as the DEP force on hollow glass particles was towards the equator, while the force on solid glass particles was towards the poles.

At small frequencies, as Figure 3.10(b) shows, both particle types collected at the poles, since the motion of particles in this regime is determined by the EHD

flow. When the frequency was increased to 6 Hz, all particles started to move away from the poles, and some hollow particles collected at the equator. Notice that solid glass particles became attached to hollow glass particles (see Figure 3.8(c)). This happened because glass particles were positively polarized and hollow glass particles were negatively polarized. The DEP force between them was attractive, and the net force on a pair containing a solid glass particle and a hollow glass particle was small, and, thus, the pairs remained between the pole and the equator. This, however, changed when the frequency was increased to 20 Hz. Both individual particles and the pairs moved to the equator. This behavior was different from what happened in Figure 3.9 where both types of particles were negatively polarized and did not attract each other.

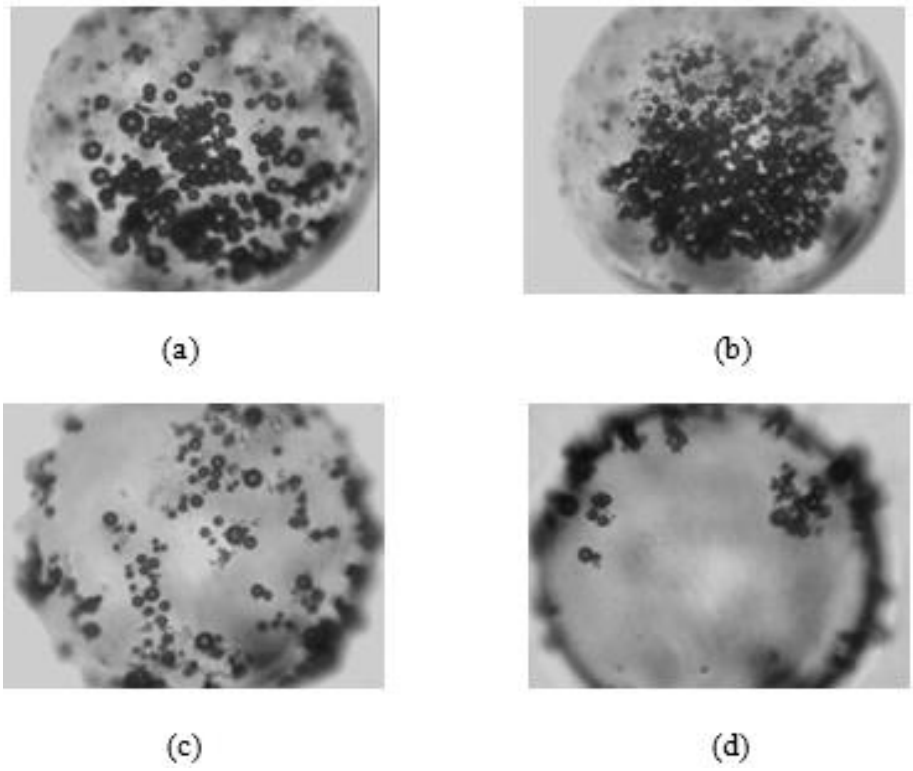

Figure 3.10 Distribution of hollow and solid glass particles on the surface of a silicone oil-I drop immersed in castor oil. The mean diameter of hollow and solid glass particles was 18 μm and 2μm, respectively, and the drop diameter was 430 μm. The voltages and frequencies are (a) 0 V; (b) 2 kV at 0.4 Hz; (c) 3 kV at 6 Hz (d) 3 kV at 20 Hz.

3.4.2.3 Silicone Oil-II Drop with Mixture of Spherical Hollow Glass Particles and Soda Lime Glass Particles in Castor Oil. Finally, the case of a silicone oil-II drop with a mixture of hollow glass particles and soda lime glass particles suspended in castor oil was considered. The diameter of the drop was approximately 405 μm. The aim was not just to separate the two types of particles from each other by varying the frequency, but also to observe the opposite of what was described in Figure 3.10 in terms of where particles collect, as

seen in Figure 3.11. This is because the use of silicone oil-II as drop liquid caused both EHD and DEP forces on both particle types to act in directions opposite to their previous directions when the drop liquid was silicone oil-I, as shown in Figure 2.10, due to differences in the properties of the two silicone oils.

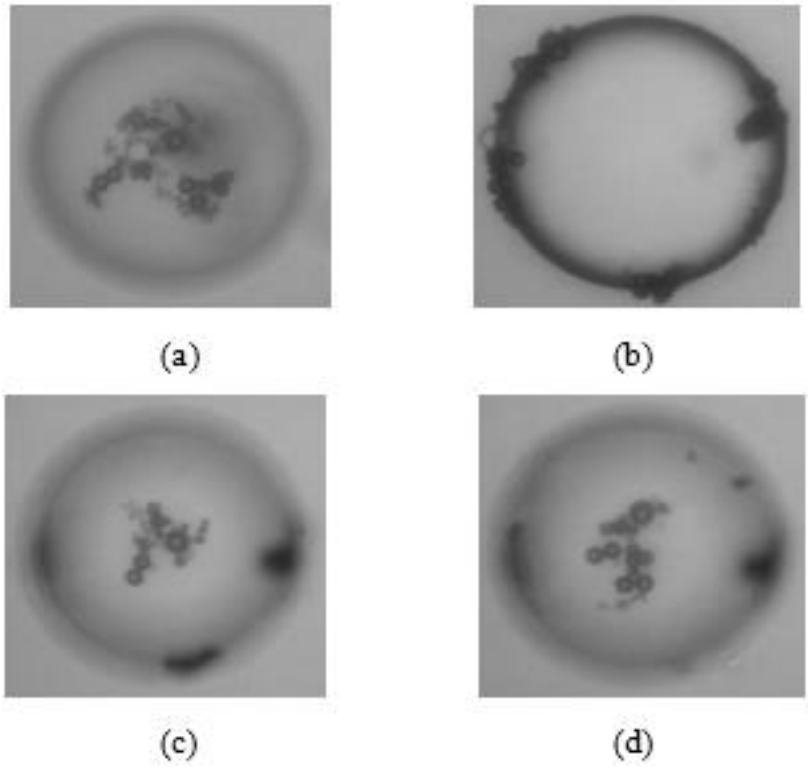

Figure 3.11 Distribution of hollow and soda lime glass particles on the surface of silicone oil-II drop immersed in castor oil. The mean diameter of hollow and solid glass particles was 18 μm and 2 μm, respectively, and the drop diameter was 405 μm. The voltages and frequencies are (a) 0 V; (b) 2 kV at 0.2 Hz; (c) 4 kV at 10 Hz (d) 4 kV at 20 Hz.

Initially, before applying voltage, the hollow glass particles rose to the pole and solid glass particles sedimented to the bottom. At frequencies below ~10 Hz, both particles moved away from the pole and collected at the equator as shown in

Figure 3.11(b), since the motion of particles was determined by EHD flow in this regime. As the frequency was increased to 10 Hz and above, hollow particles collected at the poles, as shown in Figures 3.11(c)-(d), while the soda lime glass particles remained at the equator as seen in Figure 3.11(c). However, the opposite polarizations of the two types of particles, as mentioned above, also created an attraction between the two particle types; some solid particles became attached to hollow particles and moved to the pole in Figure 3.11(c), meanwhile the soda lime glass particles are expected to be at the equator because its corresponding $\beta\beta'$ value is negative, as shown in Table 3.3.

3.5 Summary

We have shown that the distribution of particles adsorbed on the surface of a weakly conducting drop, immersed in another weakly conducting liquid, can be modified by subjecting it to an ac electric field. The problem of manipulation of particles on liquid-liquid interfaces has received considerable attention in recent years because of its importance in a wide range of applications. For example, several recent studies have been conducted in which a dc electric field is applied to manipulate the distribution of particles. The field gives rise to an EHD flow on the surface of the drop. The direction of the EHD flow can be pole-to-equator or

equator-to-pole depending on the properties of the drop and ambient liquids. The flow causes particles adsorbed on the surface of the drop to move in its direction, and so the approach can be used to concentrate particles near the poles or the equator of the drop depending on the direction of flow.

In our earlier studies, we have shown that when the drop and ambient liquids are perfect dielectric liquids, particles can be concentrated around the poles or equator of the drop by applying a uniform electric field. This happens because even when a uniform electric field is applied to a drop the field on the surface of the drop is non-uniform, and thus particles adsorbed on its surface are subjected to dielectrophoretic (DEP) forces. The motion of particles in this case is driven by the DEP forces alone because when the drop and ambient liquids are perfect dielectrics the electric field does not cause any fluid flow.

The focus of this chapter is on the forces that act on a particle when the drop and ambient liquids are weakly conducting and the drop is subjected to a uniform ac electric field. The forces that act in an ac electric field are: (i) DEP force; (ii) buoyancy force; and (iii) EHD flow induced drag force. The net force acting on a particle, which is the sum of these three forces, determines the particle's direction of motion.

The frequency of electric field is an important parameter which can be used to adjust the magnitude of the EHD flow induced drag such that it is larger or smaller than the DEP force. This is due to the fact that the EHD flow diminishes with increasing frequency and that there is a critical frequency at which the EHD flow induced drag on a particle becomes equal to the DEP force. For a frequency above the critical value, the DEP force dominates. When the fluid and particles properties are such that the EHD and DEP forces are in the opposite directions particles can be collected at the poles or the equator, and also can be moved between the poles and the equator by varying the frequency of electric field. For example, in the experiments conducted in this study, the EHD flow for cases A, B, and C was towards the poles, and for cases D and E, the EHD flow was towards the equator. All of the cases considered were such that the influence of buoyancy force was negligible when a sufficiently intense electric field was applied. At low frequencies particles movements were determined by the EHD flow. However, as the frequency was increased, the EHD flow diminished and the DEP force started to influence the motion of particles. The critical frequency at which the transition occurred was different for each of the cases; since the critical frequency is a function of particle and fluids properties. The experimentally measured critical frequency ω_c values were in good agreement with the theoretical values given by

Equation (3.9), especially considering that the drops in our experiments were in contact with the bottom surface whereas in deriving Equation (3.9) it is assumed that the drops are suspended in the ambient liquid. We demonstrated that particles can be manipulated to move in different directions on the drop surface in a certain frequency regime as determined by ω_c, provided the DEP force and the EHD drag force are not in the same direction.

It was also shown that it is possible to separate the particles of a binary mixture when the critical frequencies for the two types of particles are different. However, it was not possible to separate the particle pairs in which one type of particle was positively polarized and the other negatively as in this case there was dipole-dipole attraction between the particles which prevented them from moving apart. We were able to separate a mixture of polystyrene particles and hollow glass particles. The critical frequency ω_c for the latter particles was smaller, and so they were moved away from the poles by applying a frequency that was larger than the critical frequency for hollow glass particles, but smaller than that for polystyrene particles. It is also possible to separate particles based on their sizes. This is possible because larger particles have a lower ω_c. Larger particles were separated from smaller particles by using a frequency that caused larger particles to move away from the poles while smaller particles remained at the poles. The approach is

thus superior to traditional dielectrophoresis for which the frequency dependence is weak.

In conclusion, we have shown that when the directions of the EHD flow and the DEP force are different it is possible to collect particles at the poles or the equator of a drop by selecting a suitable frequency and that particles can be moved from the poles to the equator, or vice versa, by selecting a suitable frequency. Also, when the critical frequencies of the particles forming a binary mixture in a particular combination of drop and ambient liquids are known, the two types of particles can be separated, in a fractional manner, by tuning to corresponding critical frequencies of particle types that make up the mixture.

CHAPTER 4

NUMERICAL SIMULATIONS OF ELECTRIC FIELD DRIVEN HIERARCHICAL SELF-ASSEMBLY OF MONOLAYERS OF MIXTURES OF PARTICLES

4.1 Introduction

In recent years many studies have been conducted to understand the behavior of particles trapped at fluid-liquid interfaces because of their importance in a range of physical applications and biological processes, e.g., formation of pollen and insect egg rafts, self-assembly of particles at fluid-fluid interfaces resulting in novel nano-structured materials, stabilization of emulsions, and the formation anti-reflection coatings for high-efficiency solar cells, photonic crystals and biosensor arrays [30,58-60].

Particles trapped in fluid-liquid interfaces interact with each other via lateral capillary forces that arise because of their weight, and when present also by other forces such as electrostatic forces, to form monolayer arrangements [61-65,117-120]. A common example of capillarity-driven self-assembly is the clustering of breakfast-cereal flakes floating on the surface of milk. The deformation of the interface by the flakes gives rise to lateral capillary forces which causes them to cluster. However, capillarity-driven self-assembly produces monolayers which have

defects and lack long-range order. More so, for monolayers containing two or more different types of particles, the technique does not allow for any control of the particle-scale structure as capillary forces simply causes the particles to cluster.

It has been shown that monolayers containing two or more types of particles with different dielectric properties can be self-assembled by applying an electric field in the direction normal to the interface [65]. The technique exploits the fact that the lateral dipole-dipole force between two particles adsorbed in an interface can either be repulsive or attractive depending on their polarizabilities, and that the intensity of the force can be varied by selecting suitable upper and lower fluids. The force is repulsive when both particles are positively or are negatively polarized, but attractive when one particle is positively polarized and the other is negatively polarized. The force also depends on the sizes of the particles and the electric field intensity. The lateral capillary force between two particles of the same type is attractive, but it can be repulsive between particles of different types when the vertical force on one of them is positive and on the other is negative.

The differences in the polarizabilities and the sizes of the particles derive a hierarchical self-assembly process analogous to that which occurs at atomic scales [65]. First, groups of particles combine to form composite particles (analogous to molecules) and then these composite particles self-assemble in a pattern (like

molecules arrange in a material). The force between similar particles is repulsive (because they have the same polarizabilities), and so they move apart which allows particles that attract to come together relatively unhindered to form composite particles. The net force among the particles forming a composite particle is attractive, and so after a composite particle is formed it remains intact while the electric field is kept on.

Here, it is worth noting that the energy a particle requires to desorb from a fluid-liquid interface is several orders of magnitude larger than the thermal energy, and therefore once nano-to-micron sized particles are adsorbed, they remain adsorbed while moving laterally in the interface in response to lateral capillary and dipole-dipole forces. Furthermore, since particles adsorbed in a fluid-liquid interface are free to move laterally, they self-assemble even when the lateral forces driving the assembly are small. The only resistance to their lateral motion is hydrodynamic drag which can slow the motion but cannot stop it. This is obviously not the case for a monolayer assembled on a solid substrate, since particles are not free to move laterally because of the presence of adhesion and friction forces.

However, very-small particles do not self-assemble, even on a fluid-liquid interface, when the lateral capillary forces acting on them become comparable to Brownian forces. For example, on an air-water interface, lateral capillary forces in

the absence of an electric field become comparable to Brownian forces for particles smaller than about 10 nm, and so particles smaller than this limiting size undergo Brownian motion on the interface and do not cluster [66,121-123]. In our experiment, a sufficiently strong electric field was applied to ensure that the electrically induced lateral forces remained stronger than Brownian forces; thus making self-assembly of nano-particles possible.

The availability of liquids and particles with the specific dielectric properties limited the parameter values that could be investigated experimentally. This is obviously not the case for the numerical simulations presented in this chapter of the dissertation; which have been used to discover new self-assembled arrangements and to study the influence of Brownian force on the self-assembled monolayer as the electric field intensity is varied.

The remainder of the chapter is organized as follows. We next describe the forces that act on particles trapped at fluid-liquid interfaces and the governing equations of motion when an electric field is applied normal to the interface and the numerical method used. This is followed by a brief description of the experimental method and the experimental results for the self-assembly of binary mixtures. Then the simulation results showing other hierarchal arrangements of binary mixtures are described.

4.2 Governing Equations and Numerical Method

The lateral force F_l between two particles, i and j, adsorbed at a fluid-liquid interface in the presence of an electric field in the direction normal to the interface is given by [65]:

$$F_l = \frac{w_i w_j}{2\pi\gamma}\frac{1}{r} \quad \frac{3p_i p_j}{4\pi\varepsilon_o\varepsilon_L}\frac{1}{r^4} \tag{4.1}$$

Here w_i is the vertical force acting on the i^{th} particle, p_i is the induced dipole moment of i^{th} particle, e_0 is the permittivity of free space, e_L is the permittivity of the lower liquid, g is the interfacial tension, and r is the distance between the particles. As described in the Supplementary Information of [65], $w_i = \left(-\varepsilon_0\varepsilon_a\left(\frac{\varepsilon_L}{\varepsilon_a}-1\right)a_i^2E_0^2 f_{vi} + \frac{4}{3}\pi a_i^3\rho_{pi}g\, f_{bi}\right)$ and $p_i = 4\pi\varepsilon_o\varepsilon_L\, a_i^3\beta_i E_0$. Here E_0 is the electric field intensity (or the rms value of the electric field in an ac field), e_a is the permittivity of the upper fluid, a_i and r_{pi} are the radius and density the of i^{th} particle, and β_i is Clausius-Mossotti (CM) factor of the particle in the interface which depends on the dielectric constants of the upper and lower fluids and the particle, as well as on the position of the particle in the interface, and f_{vi} and f_{bi} are the dimensionless electric force and buoyant weight, respectively.

Notice that the first term on the right side of Equation (4.1) dominates when r is large and the second when r is small. Also, if both of these terms are

negative, the particles attract and come together so that they will physically touch each other. However, when the first term is negative and the second term is positive it is possible to have an equilibrium in which the particles do not physically touch each other. The equilibrium distance r_{eq} between the particles can be obtained by setting the total force in Equation (4.1) to zero and solving the equation for r which gives $r_{eq} = \left(\frac{3p_i p_j \gamma}{2\varepsilon_0 \varepsilon_L w_i w_j} \right)^{1/3}$. This expression assumes that the second term on the right hand side of Equation (4.1) is positive, i.e., $p_i p_j > 0$, and the first term is negative. Also, since the particles cannot overlap, r_{eq} is constrained to be greater than or equal the sum of the two particles radii because that is the closest possible approach of the two particles. In our numerical simulations, a hard sphere potential was used to enforce this constraint [75-77].

We may define the following dimensionless inter-particle equilibrium spacing parameter, $\overline{r}_i = \frac{r_{eq}}{2R_i} = \frac{1}{2R_i} \left(\frac{3p_i p_i \gamma}{2\varepsilon_0 \varepsilon_L w_i w_i} \right)^{1/3}$ to quantify the equilibrium spacing between two particles of type i. When $\overline{r}_i \leq 1$, two isolated particles of this type would be in contact in equilibrium. In a binary mixture there are two characteristic dimensionless inter-particle spacing parameters, namely $\overline{r}_1$ and $\overline{r}_2$.

The equilibrium inter-particle spacing in a monolayer containing more than two particles is smaller than r_{eq}. This is due to the fact that the force on a particle

is the net result of the multi-particle interactions among the particles of the monolayer, and the attractive capillary force decays more slowly with the distance than does the repulsive dipole-dipole force.

Let us assume that there are n particles in the interface. To numerically simulate the self-assembly process the total lateral force acting on particle i is computed by a pair-wise addition of the interaction forces. In spherical polar coordinates, the total lateral force acting on particle i can be written as

$$\mathbf{F}_{li} = \sum_{j=1, j\neq i}^{n} \left(-\frac{w_i\, w_j}{2\pi\gamma} \frac{\mathbf{e}_{ij}}{r_{ij}} + \frac{3 p_i p_j}{4\pi\varepsilon_o \varepsilon_L} \frac{\mathbf{e}_{ij}}{r_{ij}^4} \right) \tag{4.2}$$

Here, $\mathbf{e}_{ij}$ is the unit vector from the center of particle i to the center of particle j, and r_{ij} is the distance between the centers of particle i and particle j.

The particle also experiences a drag force when it moves in the fluid-liquid interface under the action of the inter-particle forces. The velocity during the self-assembly process remains small, and so we can use the Stokes equation to estimate the drag

$$\mathbf{F}_{di} = -6\pi\mu\varsigma a_i \mathbf{u}_i\,, \tag{4.3}$$

where $\mathbf{u}_i$ is the particle velocity, m is the viscosity of the lower fluid and ς is a parameter which accounts for the fact that the particle is immersed in both upper and lower fluids[8]. The fluid velocity is assumed to be zero, and so the drag acts

only when the particle moves and decreases with decreasing particle velocity. After the particles of a monolayer reach their respective equilibrium positions and stop moving, the drag acting on them becomes zero. Thus, the drag does not alter the monolayer arrangement.

Brownian motion due to thermal fluctuations at molecular scales is important for sub-micro meter sized particles. These fluctuations at molecular scales induce significant random forces on the particles of a monolayer. We will follow the approach derived from the Langevin model for Brownian motion to model the Brownian force that acts on a particle as

$$\mathbf{F}_{Bi} = \boldsymbol{\xi}(12\pi\mu a k_B T / \tau)^{1/2} \tag{4.4}$$

where k_B is the Boltzmann's constant, T is the absolute temperature and τ is the time step used in the numerical integration scheme. $\boldsymbol{\xi}$ is a random vector of a Gaussian distribution. In the numerical simulation study, the range of the values of $\boldsymbol{\xi}$ is [-0.5,0.5] [23,77-78].

The momentum equation governing the motion of particle i can be obtained by setting the mass times the acceleration of the particle equal to the total force, which is the sum of the forces given by Equations (2)-(4).

$$m_i \frac{d\mathbf{u}_i}{dt} = \sum_{j=1, j\neq i}^{n} \left(-\frac{w_i\, w_j}{2\pi\gamma} \frac{\mathbf{e}_{ij}}{r_{ij}} + \frac{3 p_i p_j}{4\pi\varepsilon_o \varepsilon_L} \frac{\mathbf{e}_{ij}}{r_{ij}^4} \right) - 6\pi\mu\xi a_i \mathbf{u}_i + \boldsymbol{\xi}(12\pi\mu a k_B T / \tau)^{1/2},\ i = 1,\ldots,\mathrm{n}, \tag{4.5}$$

where m_i is the effective mass of the i^{th} particle which includes the added mass contribution.

The self-assembly process was numerically simulated by placing n particles on a regular grid, and then these positions were moved randomly such that the particles did not overlap. Starting from this configuration, the governing equations were integrated in time until the particles stopped moving and a stable monolayer arrangement was formed. For nanoparticles, the simulations were stopped when the microstructural arrangement stopped evolving, although the particles as well composite particles continued to move because of the Brownian forces. A hard sphere potential was used to avoid the particles from overlapping [75-76]. The system of equations for n particles was discretized using an implicit second order scheme in time [79-80]. The time step used in the simulations was selected by verifying that the simulation results did not change when the time step was reduced.

4.3 Experimental Results

In our experiments, a monolayer of a mixture of particles on an air-liquid interface was formed by sprinkling the mixture onto the liquid surface, and then covering the chamber with a transparent upper electrode and applying an electric field to drive the self-assembly process.

Three distinct size dependent regimes were identified for the mixtures of glass and copolymer particles on corn, castor and silicone oils [65]. Glass particles were positively polarized and copolymer particles were negatively polarized; this was ensured by selecting suitable lower and upper fluids.

When glass particles were about two times larger than copolymer particles, the former attracted the copolymer particles to form composite particles on a mixture of corn and castor oils (see Figure 4.1(a)). The composite particles consisted of a glass particle at the center which was surrounded by a ring of copolymer particles. In this case, the spacing between the composite particles increased with increasing electric field intensity, but the spacing between the copolymer particles in the rings remained unchanged. However, when the monolayer was formed on the surface of silicone oil, the particles on the rings did not touch as they were more intensely polarized than in the mixture of corn and castor oils.

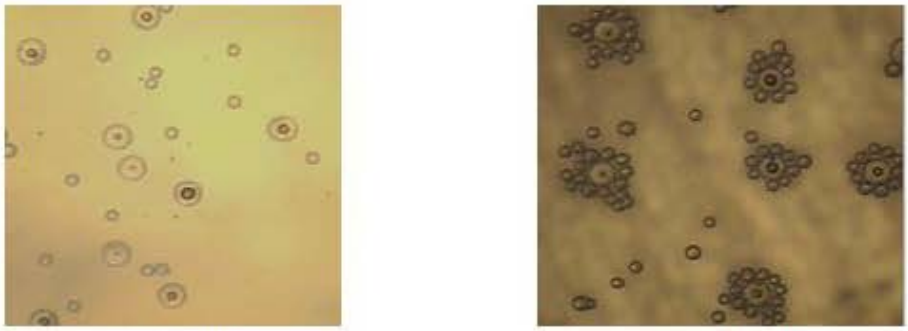

(a) Initial (b) Final

Figure 4.1 Monolayers of mixtures of 71 μm copolymer and 150 μm glass particles on the surface of a 30% castor oil and 70% corn oil mixture. The magnification is 50X and the applied electric field was 5000 V.

A second regime was obtained when the size of glass particles was about three times smaller than that of the copolymer particles (see Figure 4.2). Although smaller in size, the glass particles formed a triangular lattice in which the copolymer particles were imbedded, as the former were more intensely polarized and thus repelled each other more strongly. The copolymer particles attracted nearby glass particles to form composite particles. In this regime, the intra-composite particle forces were weaker than for the first regime. The particles forming the rings did not touch each other and interacted strongly with the lattice of glass particles. In fact, some of the glass particles escaped from the rings to occupy positions in the lattice when the field strength was increased above a

critical value. The number of particles in the rings of copolymer particles decreased as the electric field intensity was increased.

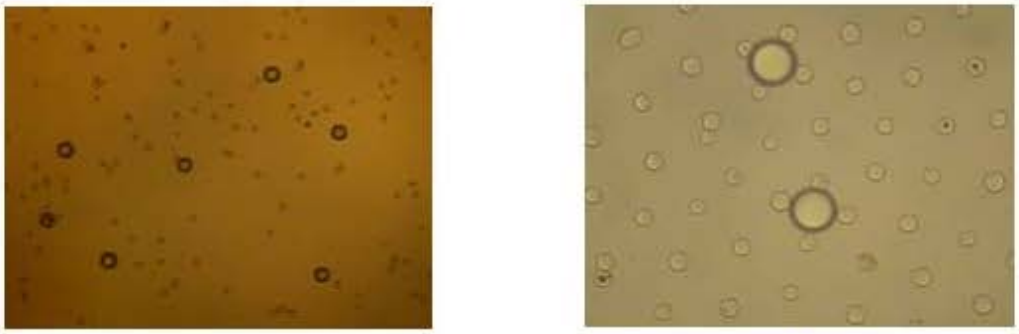

(a) Initial (b) Final

Figure 4.2 Monolayers of mixtures of 20 μm glass and 71 μm copolymer particles formed on the surface of a 30% castor oil and 70% corn oil mixture. The magnification for the first photograph is 50X and for the second 200X. The electric field was 5300 V.

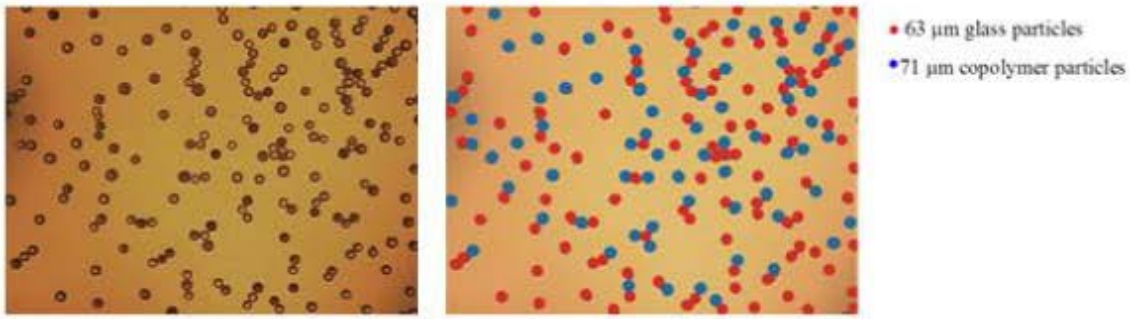

Figure 4.3 Monolayer of a mixture of 63 μm glass and 71 μm copolymer particles on the surface of silicone oil. The magnification is 50X. The graphical representation (right image) of the monolayer showing glass and copolymer particles in different colors is also included.

A third regime was obtained when the sizes of glass and copolymer particles were comparable (see Figure 4.3). Here, instead of forming ring-like arrangements,

particles arranged in chains in which the positively and negatively polarized particles alternated. In some instances, the chains contained sub-branches. This formation of chains is analogous to the formation of long chained polymeric molecules, except that the former were formed by particles in two dimensions on the surface of a liquid.

4.4 Simulation Results

The aim of this study is to explore the various monolayer arrangements that can be self-assembled on a liquid surface by applying an electric field in the direction normal to the surface. We first describe the simulation results for the cases in which the model parameters were selected to match the values in our experiments. Then, to further explore the parameter space, other parameter values for which we currently do not have experimental results are presented.

For our simulations, unless otherwise stated, the properties of the larger and smaller particles will be denoted by the variables with subscripts "1" and "2", respectively. Also, in our simulations, without loss of generality, we may assume that the larger particles are positively polarized and the smaller particles are negatively polarized. The ratio of their intensities of polarizations $\frac{\beta_1}{\beta_2}$ is allowed to take values either greater or smaller than unity. For the binary mixtures considered, the sign of $\frac{\beta_1}{\beta_2}$ was negative as the particles of one type were positively polarized and those of the other type were negatively polarized. The dipole-dipole force between two particles of different types was attractive, and so the mixture particles combined to form composite particles. The primary focus of this chapter is to study monolayers of such mixtures. When the polarizabilities of two particles of different types have the same sign the dipole-dipole forces between them are

repulsive, and so the particles of different types also move apart and composite particles are not formed. The ratio of the number of larger to smaller particles for the majority of cases considered was 1:7, but it was varied to study its role in the self-assembly process.

For particle mixtures adsorbed on the corn oil surface, the fluid and particle properties appearing in the equations were: $\varepsilon_a = 1.0$, $\varepsilon_L = 2.87$; the dielectric constants of glass and copolymer particles were 6.5 and 2.5, respectively; and the specific densities of glass and copolymer particles were 2.5 and 1.05, respectively. The corn oil viscosity was assumed to be 65 cP. Based on these values, the theoretical estimates of the Clausius-Mossotti (CM) factors of the particles were β_1 = 0.297 and β_2 = -0.045. Here the subscripts "1" and "2" refer to glass (larger) and copolymer (smaller) particles respectively. The values of the remaining parameters were estimated to be $fv_1 = 0.02$, $fv_2 = 0.02$, $fb_1 = 1.0$, $fb_2 = 0.05$ and ξ = 0.5 (see [65]) The particle sizes were assumed to be equal to the values in our experiments and the electric field strength E_0 was obtained in terms of the applied voltage (V) and the gap between the electrodes (L). Using these parameter values, the values of p_1, p_2, w_1 and w_2 were obtained for the simulation.

The number of particles for most of our simulations was held fixed at 144. The lengths have been nondimensionalized such that the size of larger particles is 0.1. The diameters of the circles used to represent the particles were proportional to the sizes of the particles. Also, the circles representing particles were color-coded to differentiate the two types of particles; red color depicts the larger-sized particles, while blue color depicts the smaller-sized particles.

4.4.1 Validation of Numerical Results

The three distinct size dependent regimes identified in our experiments for the mixtures of glass and copolymer particles on corn oil were also found and validated in our numerical simulations. The ratio of the number of larger to smaller particles was varied in each regime to resemble the corresponding experimental setup. Figures 4.4-4.6 show the numerical results for the three regimes identified in our experiment. Also, we have verified that the numerical results reported in this chapter were independent of the time step used. Furthermore, although the exact distribution depended on the initial distribution of particles, the qualitative arrangement was independent of the initial distribution. The Brownian force was not included in these simulations since the particles were relatively large in size.

Figure 4.4 shows the numerical result for a mixture of 71 μm copolymer and 150 μm glass particles. The ratio of the number of larger (red) to smaller (blue)

particles is 1:7. As stated earlier, the larger particles are positively polarized and the smaller particles are negatively polarized. The larger particles attracted the smaller ones to form composite particles, similar to those seen in the experiments (see Figure 4.1). Figure 4.4(a) and Figure 4.4(b) show that the spacing between the composite particles increased when the electric field intensity was increased, which agrees with the experimental observations. The inter-composite particle spacing between the smaller particles in the rings remained unchanged as the electric field intensity was increased. The reason behind this was that the larger particles were more intensely polarized than the smaller particles, such that the dipole-dipole attraction between a smaller particle and the larger particle of a composite particle was much greater than the dipole-dipole repulsion among the smaller particles of the same ring.

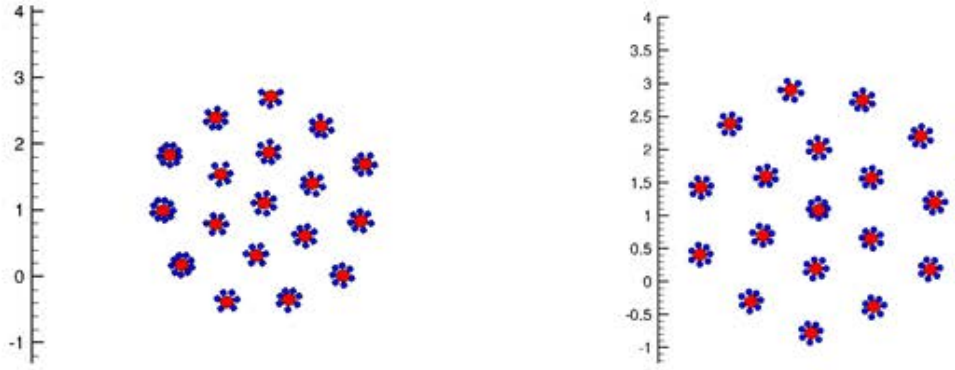

Figure 4.4 Numerical simulation of self-assembly of mixtures of particles on liquid surfaces. The parameters were selected to match 71 μm copolymer and 150 μm glass particles on corn oil. The applied electric field was 560 kV/m in (a), 700 kV/m in (b).

In Figure 4.5, the smaller particles were more intensely polarized, which is the case for the mixture of 71 μm copolymer and 20 μm glass particles. This case corresponds to Figure 4.2 where the glass particles were about three times smaller than the less intensely polarized copolymer particles. The ratio of the number of larger to smaller particles is 1:15. As in the experiments, the smaller particles formed a triangular lattice in which the larger particles were imbedded. The larger particles attracted nearby smaller particles in the lattice and together they formed composite particles. To examine the strength of inter-particle forces, the electric field strength was increased from 530 kV/m in Figure 4.5(a) to 900 kV/m in Figure 4.5(b). As seen in Figure 4.5(b), the inter-composite particles spacing

increased due to an increase in the inter-composite particles repulsive force. The lattice spacing of the smaller particles also increased.

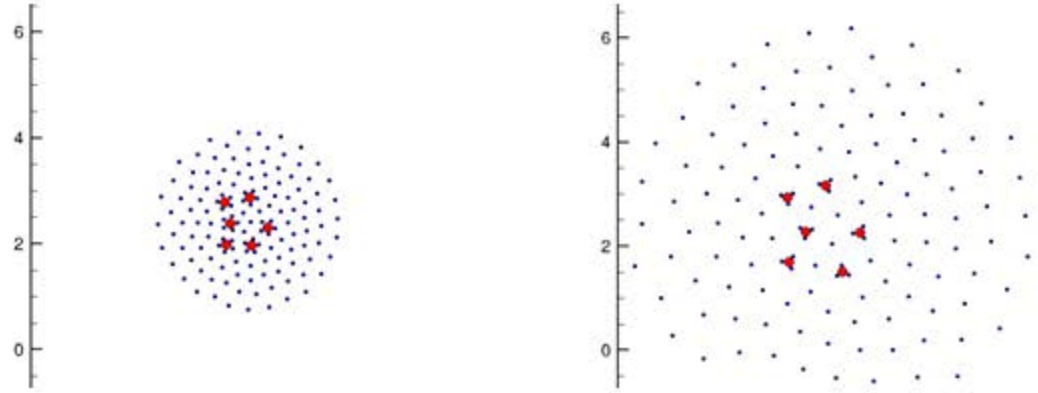

(a) $\bar{r}_1 = 16.60$, $\bar{r}_2 = 19.47$ (b) $\bar{r}_1 = 23.54$, $\bar{r}_2 = 8.67$

Figure 4.5 Numerical simulation of self-assembly of mixtures of particles on liquid surfaces. The parameters have been selected to match 71 µm copolymer and 20 µm glass particles on corn oil. The applied electric field was 530 kV/m in (a), and 900 kV/m in (b).

Unlike in the previous case shown in Figure 4.4, the dipole-dipole attractive force between a smaller particle and the larger particle of a composite particle was weaker than the repulsive force between the smaller particles in the ring of the composite particle. Due to this force imbalance, smaller particles escaped from the rings, thereby reducing the number of particles from 5 to 3. The escaped particles were absorbed in the lattice which expanded to accommodate them. In this regime, the inter-composite particle forces were weaker than in the first regime and the particles forming the rings did not touch each other.

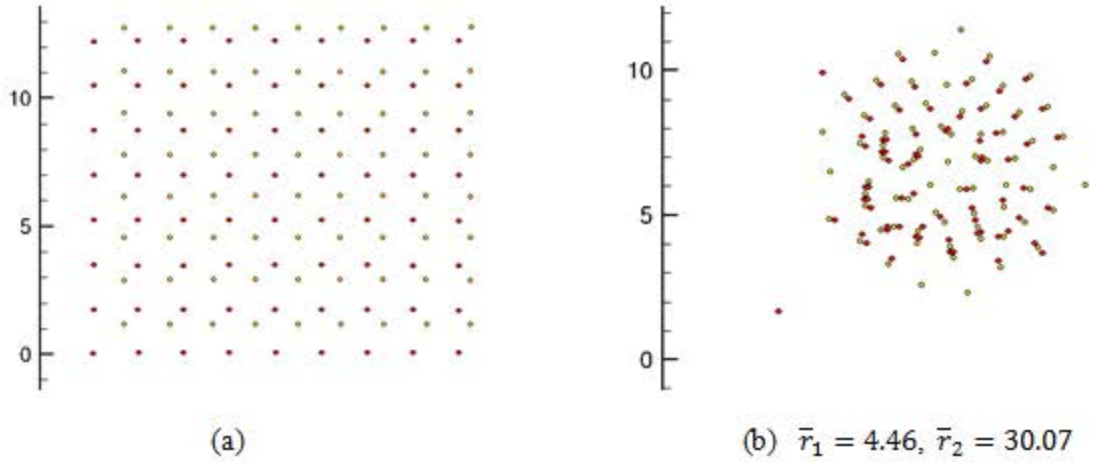

Figure 4.6 Numerical simulation of self assembly of mixtures of particles on liquid surfaces. The parameters have been selected to match 71 μm copolymer (red) and 63 μm glass (yellow) particles on corn oil. The applied electric field was 500 kV/m; (a) Initial distribution, (b) final distribution.

Figure 4.6 shows a third regime for which the sizes of positively and negatively polarized particles were comparable, where the mixture consists of 71 μm copolymer (red) and 63 μm glass (yellow) particles. The ratio of the number of small to larger particles is 1:1. In this case, instead of forming ring-like arrangements, the particles arranged in chains in which the positively and negatively polarized particles alternated. Initially, the particles formed doublets of positively and negatively polarized particles, and then these doublets merged to form longer chains. These simulation results are similar to the experimental results shown in Figure 4.3 for a mixture of glass and polymer particles. When the positively and negatively polarized particles are of comparable sizes and concentrations, they self assemble to form particle chains. The results presented above show that Equation (4.5) correctly models inter-particle forces, and therefore we may use it to explore the parameter space.

4.4.2 Dependence of Assembled Monolayer on $\frac{r_1}{r_2}$ and $\frac{\beta_1}{\beta_2}$

To study the parameter space that was limited by the availability of particles with specific dielectric constants and sizes, simulations were conducted for different size ratios $\frac{r_1}{r_2}$ and CM factor ratios $\frac{\beta_1}{\beta_2}$. While changing these ratios, the size of the larger particles r_1 and the CM factor of the smaller particles β_2 were fixed at 150 μm and -0.05, respectively. The electric field strength was set at 365 kV/m. For the results presented in Figures 4.7–4.9, all other parameter values were held fixed. The dimensionless inter-particle spacing parameters $\bar{r}_1$ and $\bar{r}_2$ for the two-particle pairs "1-1" and "2-2" respectively are listed in the figures for each of the simulated cases.

For the results shown in Figure 4.7, $\frac{r_1}{r_2} = 1.2$ and $\frac{\beta_1}{\beta_2}$ was varied between -0.5 and -7.5. The Figure shows that the lattice arrangement changes significantly with increasing $\frac{\beta_1}{\beta_2}$. In Figure 4.7(a), the smaller particles formed an approximate triangular lattice, while the larger particles clustered at the center. This was due to the fact that the capillary force among the larger particles was the dominant force and ($\bar{r}_1 = 0.28$), which caused them to cluster near the center of the domain. The larger particles were also attracted to the smaller particles, but the force between them was relatively weaker. The smaller particles formed a lattice, but the spacing between them was larger as $\bar{r}_2 = 5.19 > \bar{r}_1$. Notice that in Figure 4.7(a), there were a few smaller particles trapped in-between the larger particles and some

smaller particles were near the outer boundary of the cluster of larger particles as they were attracted to the larger particles. The arrangement changed with increasing $\frac{\beta_1}{\beta_2}$. When $\frac{\beta_1}{\beta_2}$ was increased to -1.0, the repulsive dipole-dipole force among the larger particles increased, which increased the equilibrium spacing amongst the larger particles ($\overline{r}_1 = 0.45$).

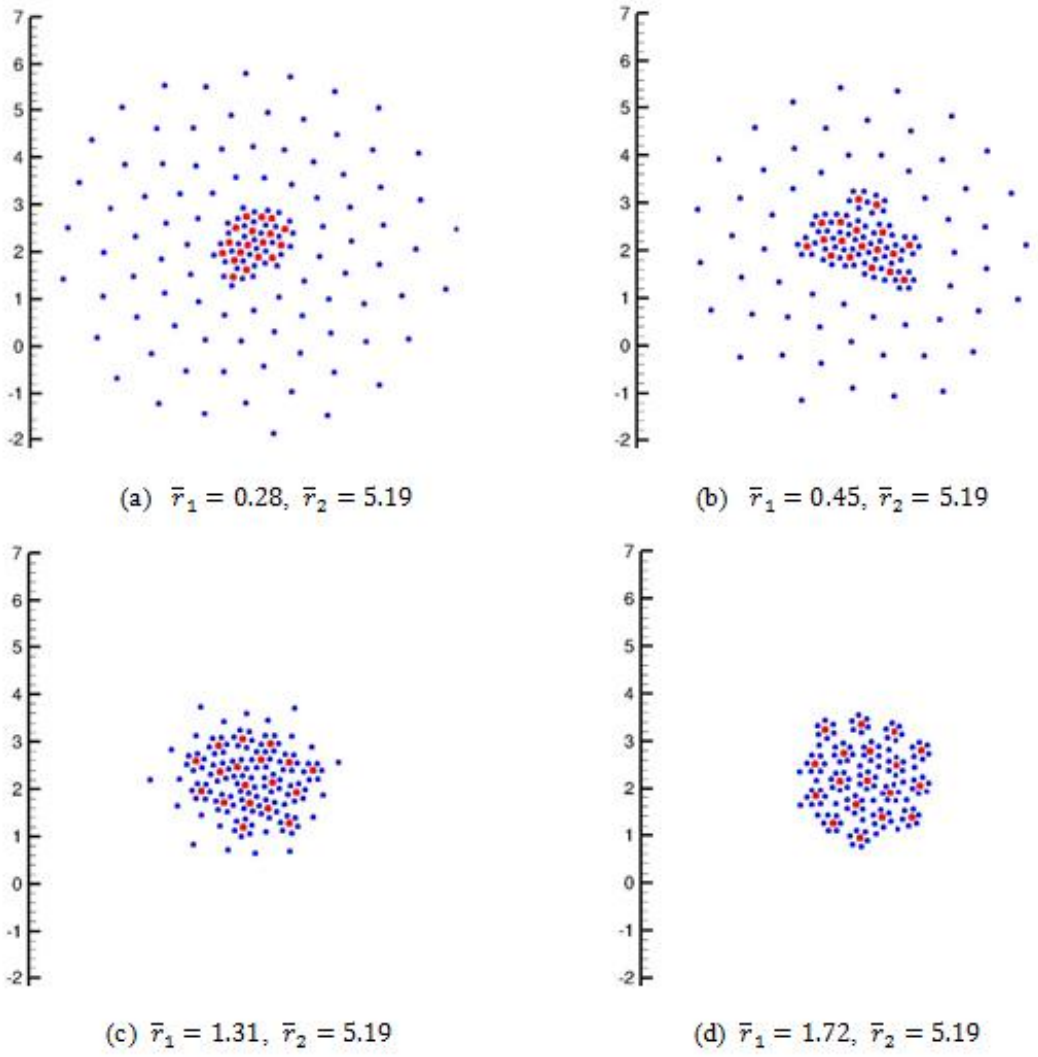

Figure 4.7 Numerical simulation of self-assembly of mixtures of particles on liquid surface for $\frac{r_1}{r_2} = 1.2$. The ratios of $\frac{\beta_1}{\beta_2}$ are: (a) -0.5, (b) -1.0, (c) -5.0, and (d) -7.5.

The attractive force between the smaller and larger particle also increased causing more of the smaller particles to be trapped in the cluster of larger particles and become attached to the larger particles. Together they formed a cluster near the center of the domain with the particles touching each other. When $\frac{\beta_1}{\beta_2}$ was increased further, the repulsive force between the larger particles increased and so the spacing between them also increased; $\overline{r}_1 = 1.31$ in Fig 4.7(c) and $\overline{r}_1 = 1.71$ in Figure 4.7(d). The force between the larger and smaller particles also increased, and so they joined together to form composite particles as seen in Figures 4.7(c)-(d). The average number of smaller particles in the rings of the composite particles increased with increasing $\frac{\beta_1}{\beta_2}$. This is due to the increased spacing between the larger particles which allowed additional smaller particles to enter in the space between the larger particles to form composite particles.

Figure 4.8 shows the results for $\frac{r_1}{r_2} = 2.0$. A larger value of $\frac{r_1}{r_2}$ compared to that in Figure 4.7 was obtained by reducing r_2, while keeping r_1 fixed. Thus, $\overline{r}_1$ values are the same as in Figure 4.7, but $\overline{r}_2 = 11.52$. The simulation results are shown for the same initial particle distributions after the same time interval as in Figure 4.7 which allowed us to compare the magnitudes of capillary and dipole-dipole forces acting on the particles based on the assembled monolayers for the two cases. In Figure 4.8, the changes in the lattice arrangement with increasing $\frac{\beta_1}{\beta_2}$ were

qualitatively similar to those in Figure 4.7. The capillary force amongst the larger particles was the dominant force which caused them to cluster near the center of the domain. Since the smaller particles were two times smaller than in Figure 4.7, the capillary and dipole-dipole forces for them were weaker and so they did not arrange on a triangular lattice as they moved relatively slowly.

In Figures 4.8(c)-(d), $\frac{\beta_1}{\beta_2}$ was increased by the same proportions as in Figures 4.7(c)-(d). This increased the repulsive force among the larger particles, and as in Figures 4.7(c)-(d), enabled the formation of composite particles. One major difference was that the average number of smaller particles in the rings of the composite particles was fewer. This was due to the fact that the attractive force among the particles was weaker and so fewer smaller particles were pulled closer to the center of the domain where the larger particles were clustered. This limited the number of smaller particles in the ring of a composite particle.

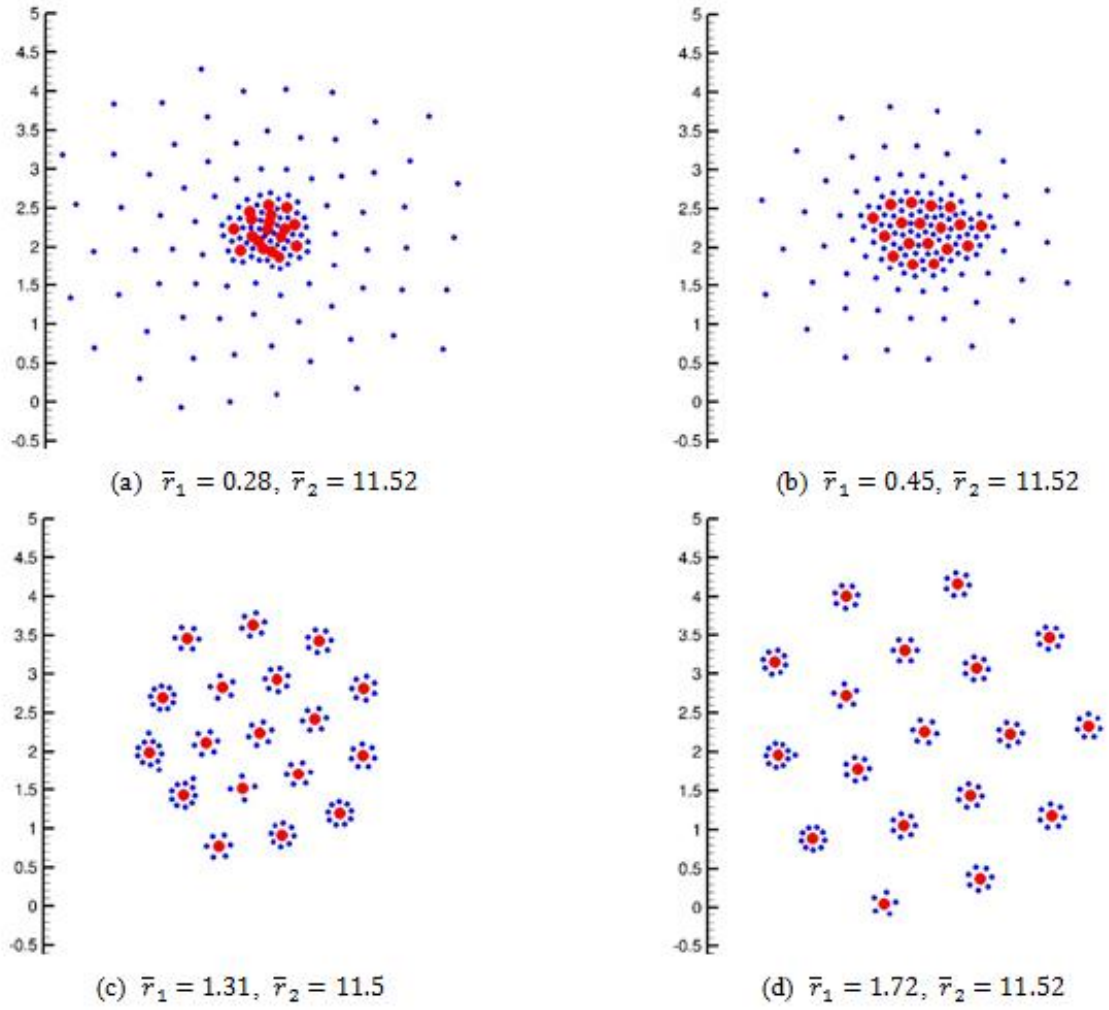

Figure 4.8 Numerical simulation of self-assembly of mixtures of particles on liquid surface for $\frac{r_1}{r_2} = 2.0$. The ratios of $\frac{\beta_1}{\beta_2}$ are: (a) -0.5, (b) -1.0, (c) -5.0, and (d) -7.5.

Also in comparison to the results in Figures 4.7(c)-(d), the increased inter-particle spacing among the composite particles in Figures 4.8(c)-(d) was due to the increased dipole-dipole repulsion among them as the oppositely polarized smaller particles forming the rings were smaller and fewer.

In Figure 4.9, the results are for the case where the ratio $\frac{\beta_1}{\beta_2}$ was fixed at -10, while $\frac{r_1}{r_2}$ was varied from 1.2 to 2.0 by changing r_2. Thus, $\bar{r}_1 = 2.08$ and $\bar{r}_2$ is varied. The aim was to study the dependence on the size of the smaller particles. From the figures, it can be seen that as $\frac{r_1}{r_2}$ is increased, the inter-composite particle spacing increases and a larger fraction of smaller particles is left out from the formation of composite particles.

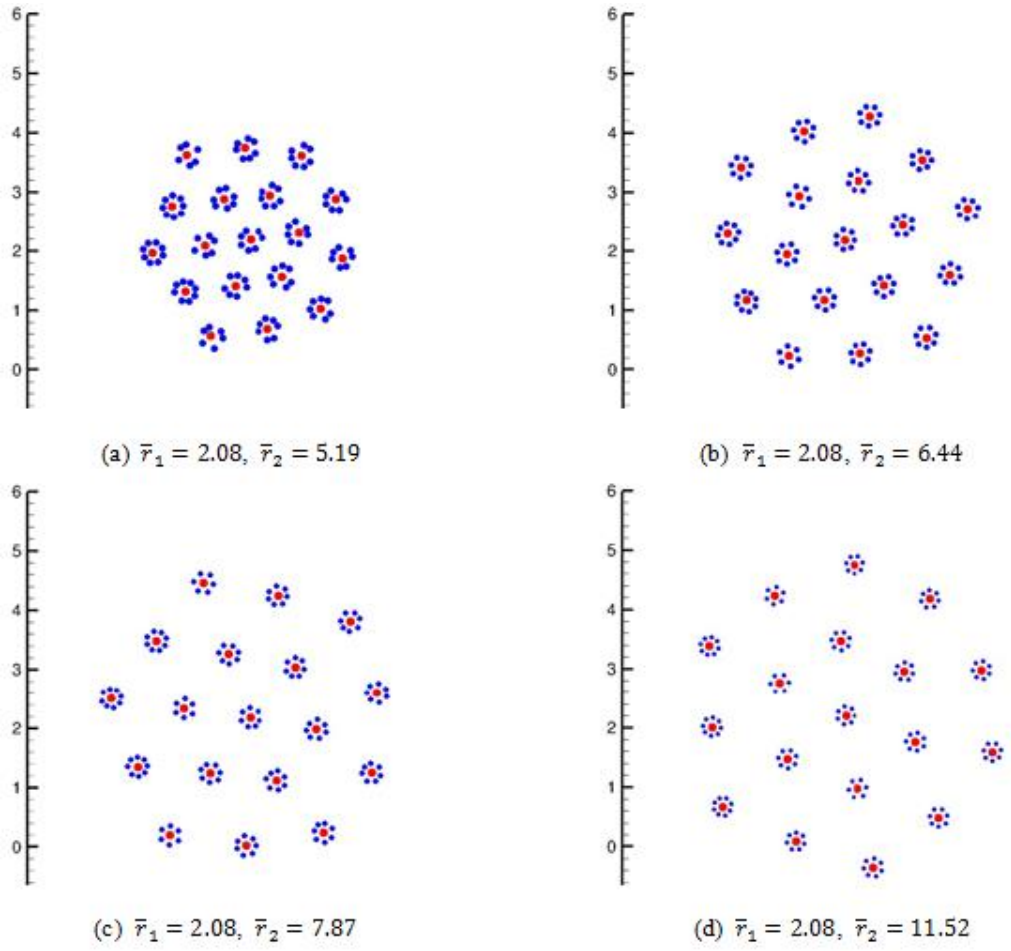

Figure 4.9 Numerical simulation of self-assembly of mixtures of particles on liquid surface for $\frac{\beta_1}{\beta_2} = -10.0$. The ratios $\frac{r_1}{r_2}$ are: (a) 1.2, (b) 1.4, (c) 1.6, and (d) 2.0.

The same reason as given in Figures 4.7 and 4.8 is applicable here: as the size ratio was increased, the smaller particles forming the rings were less effective in reducing the dipole-dipole repulsion among the composite particles. The increased dipole-dipole repulsive force among the composite particles caused an increase in the inter-composite particle spacing. The decreased strength of the capillary force among the smaller and larger particles affected their motion towards the center of the domain. Thus, as shown in Figure 4.8, there were fewer particles near the center of the domain to attach to the larger particles to form composite particles.

4.4.3 Effect of electric and buoyancy induced capillary forces on monolayer

We next study the roles of $\frac{f_{v1}}{f_{v2}}$ and $\frac{f_{b1}}{f_{b2}}$ in determining the nature of assembled monolayers when the two types of particles were of the same size $\left(\frac{r_1}{r_2} = 1.0\right)$, and the same number of each type of particles were present. The former parameter determines the relative magnitudes of the electric field induced capillary force between the two types of particles, and $\frac{f_{b1}}{f_{b2}}$ of the buoyancy induced capillary forces. For the results presented in Figures 4.10-4.11, the ratios were varied by changing f_{v2} and f_{b2} for the blue particles, while the values for the red particles were fixed at f_{v1}=0.1 and f_{b1} =1. The particles diameter was 150 μm. The CM

factors were β_1= 0.297 and β_2= -0.045, and $\frac{\beta_1}{\beta_2} = -6.6$. The electric field strength was fixed at 500 kV/m and the remaining parameter values were held fixed.

In Figure 4.10, the results are shown for a case where $\frac{f_{v1}}{f_{v2}}$ was varied while holding $\frac{f_{b1}}{f_{b2}} = 8.0$ fixed. The latter means that the blue particles were less dense. The Figure shows a gradual change in the structure of the assembled monolayers as $\frac{f_{v1}}{f_{v2}}$ was increased by decreasing f_{v2}. As f_{v2} was decreased, the electric field induced vertical force on the blue particles decreased, and since in Figure 4.10 the vertical electric force is in the opposite direction to the buoyant weight and it is the dominant vertical force, the lateral capillary on the particles decreased. Consequently, $\overline{r}_2$ increased from 0.46 to 11.47 because the repulsive dipole-dipole forces pushed the blue particles farther apart. It is noteworthy that the capillary force between a red and a blue particle in Figure 4.10 is repulsive, but its magnitude decreases with $\frac{f_{v1}}{f_{v2}}$. The dipole-dipole force between them is attractive for all of the cases. Also, the capillary force is long ranged but the dipole-dipole forces decays much faster with the distance.

In Figure 4.10(a), about half of the particles assembled to form binary particle pairs but some formed 3-6 particle clusters. There was one red (positively polarized) and one blue particle (negatively polarized) in the pairs, and two blue

and two red in the four particle clusters. These particle clusters were arranged on a radially symmetric lattice. The tendency of the red and blue particles to come together was due to the dipole-dipole forces which decay rapidly with the distance; the capillary forces between them were repulsive since $w_1 > 0$ and $w_2 < 0$.

In Figures 4.10(b)-(c), as $\frac{f_{v1}}{f_{v2}}$ was increased, the capillary force between the blue particles decreased and dipole-dipole repulsive force between the blue particles remained the same. The repulsive capillary force among the red and blue particles decreased allowing dipole-dipole attractions to dominate which caused the inter-particle distance to decrease. This decrease in the lattice spacing caused the binary particle pairs to coalescence to form longer chains. Also, increasing $\frac{f_{v1}}{f_{v2}}$ caused the repulsive capillary force between the red and blue particles to decrease, and thus the distance between the particles decreased and the area over which the particles were spread decreased.

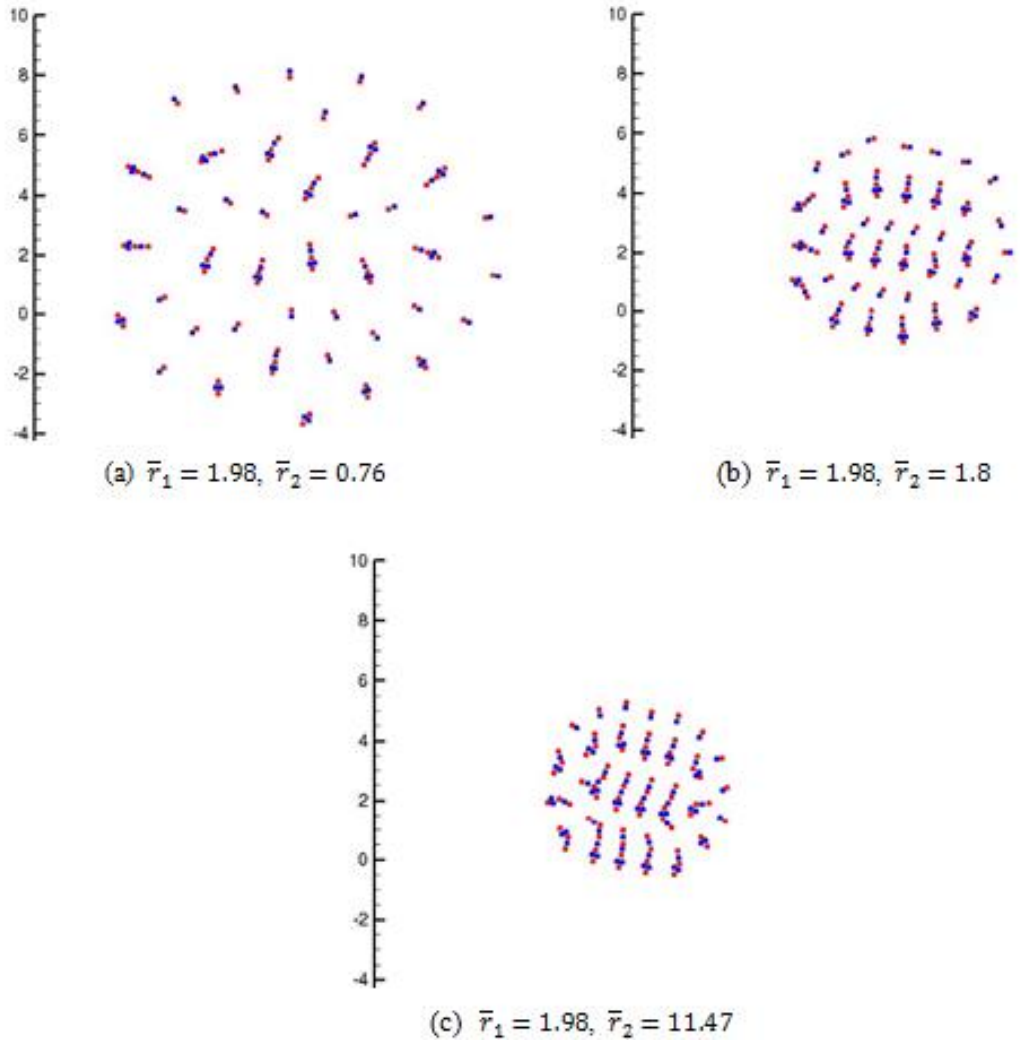

Figure 4.10 Numerical simulation of self-assembly of mixtures of particles on liquid surface for $\frac{f_{b1}}{f_{b2}} = 8.0$ and $\frac{r_1}{r_2} = 1.0$. The ratio $\frac{f_{v1}}{f_{v2}}$ is: (a) 0.2, (b) 0.5, and (c) 2.0.

Figure 4.11 shows the results for the cases where $\frac{f_{v1}}{f_{v2}} = 0.5$ was kept fixed, while $\frac{f_{b1}}{f_{b2}}$ was increased by decreasing f_{b2}. The net vertical force on the blue particles is negative and so the capillary force between a red and a blue particle was repulsive, and among the blue particles was attractive.

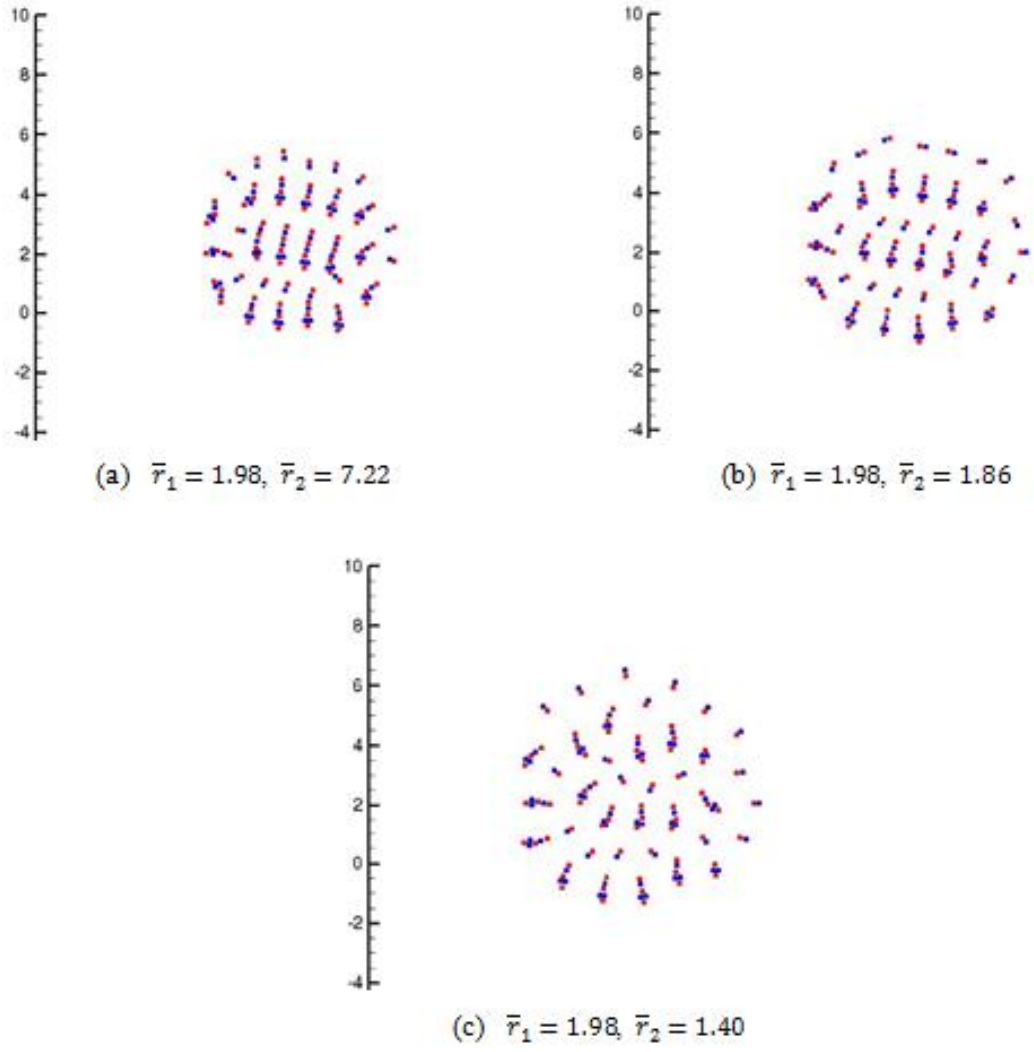

Figure 4.11 Numerical simulation of self-assembly of mixtures of particles on liquid surface for $\frac{f_{v1}}{f_{v2}} = 0.5$ and $\frac{r_1}{r_2} = 1.0$. The ratio $\frac{f_{b1}}{f_{b2}}$ is: (a) 4.0, (b) 8.0, and (c) 20.0.

Furthermore, the capillary forces among the red and blue particles decreased with increasing $\frac{f_{b1}}{f_{b2}}$. Thus, the lattice spacing increased, and the chains of particles started to break down into smaller chains. As in Figure 4.10(a), the monolayer arrangement in Figure 4.11(d) consisted of binary particle pairs and shorter chains.

4.4.4 Effects of particle sizes and distribution ratio on monolayer arrangement

The ratio of the number of larger particles to smaller particles $\frac{N_1}{N_2}$ also influences the monolayer arrangement. To study this, the total number of particles in the domain was kept constant, while $\frac{N_1}{N_2}$ was varied.

Figure 4.12 shows how the arrangement changes when $\frac{N_1}{N_2}$ was increased for a constant value of $\frac{r_1}{r_2} = 1.4$, with $2r_1 = 150\ nm$. The CM factors were β_1= 0.297 and β_2= -0.045, and $\frac{\beta_1}{\beta_2} = -6.6$. The electric field strength was fixed at 500 kV/m and all of the other parameter values were held fixed. In Figure 4.12(a), the ratio $\frac{N_1}{N_2}$ is $\frac{1}{7}$. The monolayer consists of composite particles which contained a larger sized particle at the center with 6-7 smaller particles forming a ring around the larger particle. Some of the smaller particles were left out in the formation of composite particles. The rings containing 6 particles tightly covered the particle at the center and those containing 7 particles did not tightly cover the center particle as their length was longer. There is a maximum number of smaller particles that can be in the ring of a composite particle which depends on the strength of the dipole-dipole attractive force between the larger and smaller particles and the strength of the dipole-dipole repulsive force between the smaller particles and the

size ratio. This is important because the number of particles in the ring of a composite particle can be controlled by selecting suitable parameter values; which in practice can be done by selecting suitable upper and lower fluids. Also notice that the distribution of composite particles in this case was not radially symmetric.

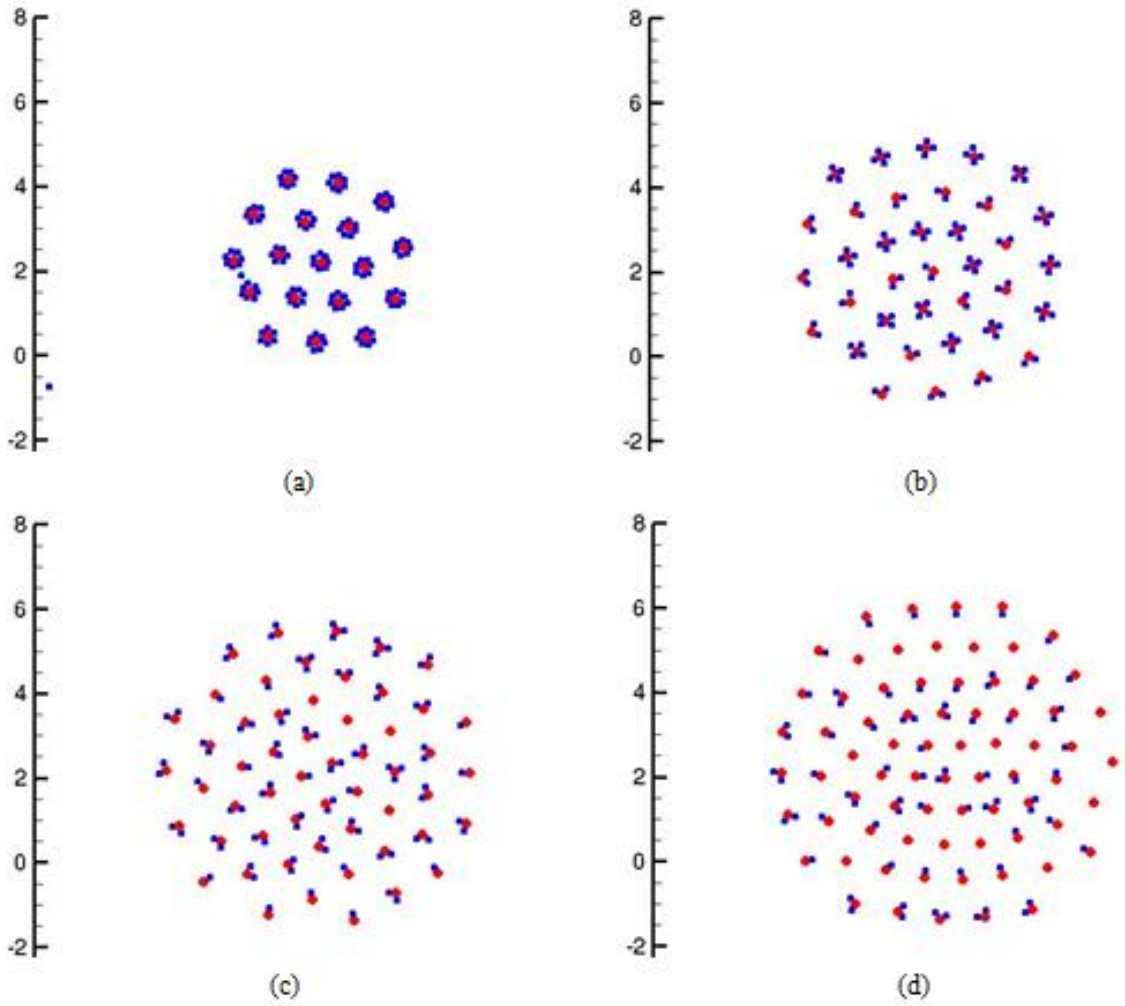

Figure 4.12 Numerical simulation of self-assembly of mixtures of particles on liquid surface for $\frac{r_1}{r_2} = 1.4$, $\bar{r}_1 = 1.98$, $\bar{r}_2 = 3.22$. The concentration ratio $\frac{N_1}{N_2}$ is: (a) $\frac{1}{7}$, (b) $\frac{1}{3}$, (c) $\frac{3}{5}$, and (d) 1.

When the ratio $\frac{N_1}{N_2}$ was changed to $\frac{1}{3}$, the average number of particles in the rings reduced to three and the assembled monolayer arrangement became radially symmetric. This was a result of an increase in the repulsive force among the composite particles which also caused the monolayer to spread over a larger area. The increase in the repulsive force was due to a reduction in the number of smaller

particles in the rings. This trend continued in Figures 4.12(c)-(d). When the concentration ratio was 1:1, as shown in Figure 4.12(d), the monolayer consisted mostly of binary particles and some longer chains since the concentrations of the two particle types in the domain were equal, and the area of the monolayer was the largest.

4.4.5 Effect of Brownian force on self-assembled monolayers

We next consider the effects of Brownian force on the monolayers as the electric field intensity, $\frac{r_1}{r_2}$, $\frac{\beta_1}{\beta_2}$ and $\frac{N_1}{N_2}$ are varied. For the simulation results presented so far, the Brownian force was not included in the equations of motion as the particles size was of O(100) m. The influence of Brownian force on particles becomes important only for micron and submicron sized particles.

As for the cases described earlier, red color is used to show the larger sized particles (or to show one type of particles when they are of equal size) and blue to show the smaller sized particles. The former are assumed to be positively polarized and the latter negatively. The diameter of the larger particles (r_1) was fixed at 150 nm and the CM factor of the smaller particles (β_2) was fixed at -0.05. The ratio of the number of larger to smaller particles unless otherwise noted is 1:7.

We first consider the changes in the assembled monolayers with $\frac{r_1}{r_2} = 1.2$ and $\frac{\beta_1}{\beta_2} = -7.5$, as the electric field intensity was increased. The particles distribution for the electric field intensity of 10 MV/m, shown in Figure 4.13(a), appeared mostly random with only some of the particles coming together to form composite particles. The Brownian force in this case was stronger than the electric field induced capillary and dipole-dipole forces which indicate that the field intensity was below the value that was needed to form composite particles.

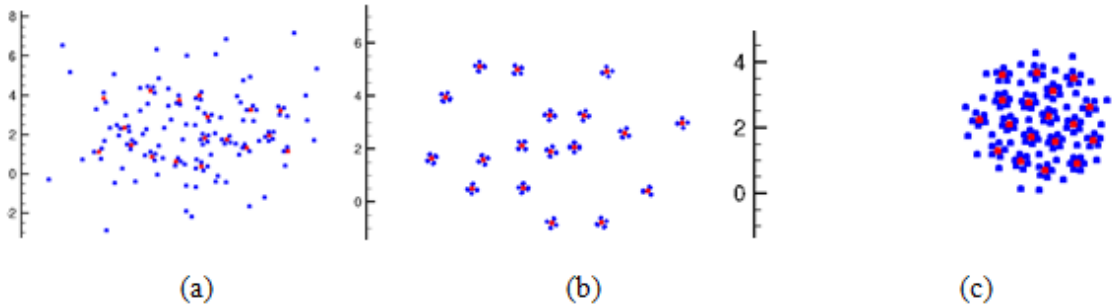

Figure 4.13 Numerical simulation of self-assembly of mixtures of particles for $\frac{r_1}{r_2} = 1.2$ and $\frac{\beta_1}{\beta_2} = -7.5$. The value of E_0 is: (a) 10 MV/m, (b) 60 MV/m, and (c) 95 MV/m.

When the electric field intensity was increased to 60 MV/m, the induced dipole-dipole and capillary forces increased (see Figure 4.13(b)), and there was a greater tendency for the two types of particles to form composite particles similar to those in Figures 4.7-4.9 for the micron sized particles. In fact, the compositions of composite particles here was relatively more uniform because of the presence of Brownian forces which caused mixing before the composite particles formed. The

tendency to form composite particles was even greater in Figure 4.13(c) where the field strength was 95 MV/m. Also, since the dipole-dipole forces were stronger, most of the smaller particles were captured in the rings of larger particles and the spacing between the composite particles decreased. The latter was a consequence of the fact that the effective repulsion among the composite particles decreased because they were surrounded by the oppositely polarized smaller particles. Furthermore, since the dipole-dipole forces were stronger, the smaller (blue) particles also arranged on a triangular lattice which was not the case in Figure 4.13(b).

We next present results which show how the influence of Brownian forces on the assembled monolayers changes when $\frac{r_1}{r_2}$, $\frac{\beta_1}{\beta_2}$ and $\frac{N_1}{N_2}$ are varied for a fixed electric field intensity. The ratio $\frac{N_1}{N_2}$ was $\frac{1}{7}$ in Figure 4.14 and it was 1 in Figure 4.15. The electric field intensity was $95\ \mathrm{MV/m}$. The Figures show the monolayer arrangements for three different values of $\frac{\beta_1}{\beta_2}$ for three fixed $\frac{r_1}{r_2}$ values. We remind the reader that when $\frac{\beta_1}{\beta_2}$ is increased the dipole-dipole repulsion among the larger particles increases, but the attraction between the larger and smaller particles also increases. The latter attraction results in the formation of composite particles. Consequently, when $\frac{\beta_1}{\beta_2}$ was larger the composite particles contained more particles

in their rings, especially when $\frac{r_1}{r_2}$ was closer or equal to one. As noted earlier, the formation of composite particles decreased the dipole-dipole repulsion among the larger particles and so the inter-composite-particle spacing decreased. This was more pronounced when the size of blue particles was equal to the size of red particles. As $\frac{r_1}{r_2}$ was increased, the capillary and repulsive dipole-dipole forces among the smaller particles decreased, and the Brownian forces caused some of the smaller particles to drift away from the monolayer. Thus, the composite particles contained fewer smaller particles which in turn increased the spacing between the composite particles. The degree of arrangement in the assembled monolayer diminished due to the presence of Brownian motion and the increased inter-composite-particle distance, and as a result they were not arranged periodically. The influence of Brownian forces on the monolayer arrangement increased with increasing $\frac{r_1}{r_2}$, but diminished with increasing $\frac{\beta_1}{\beta_2}$.

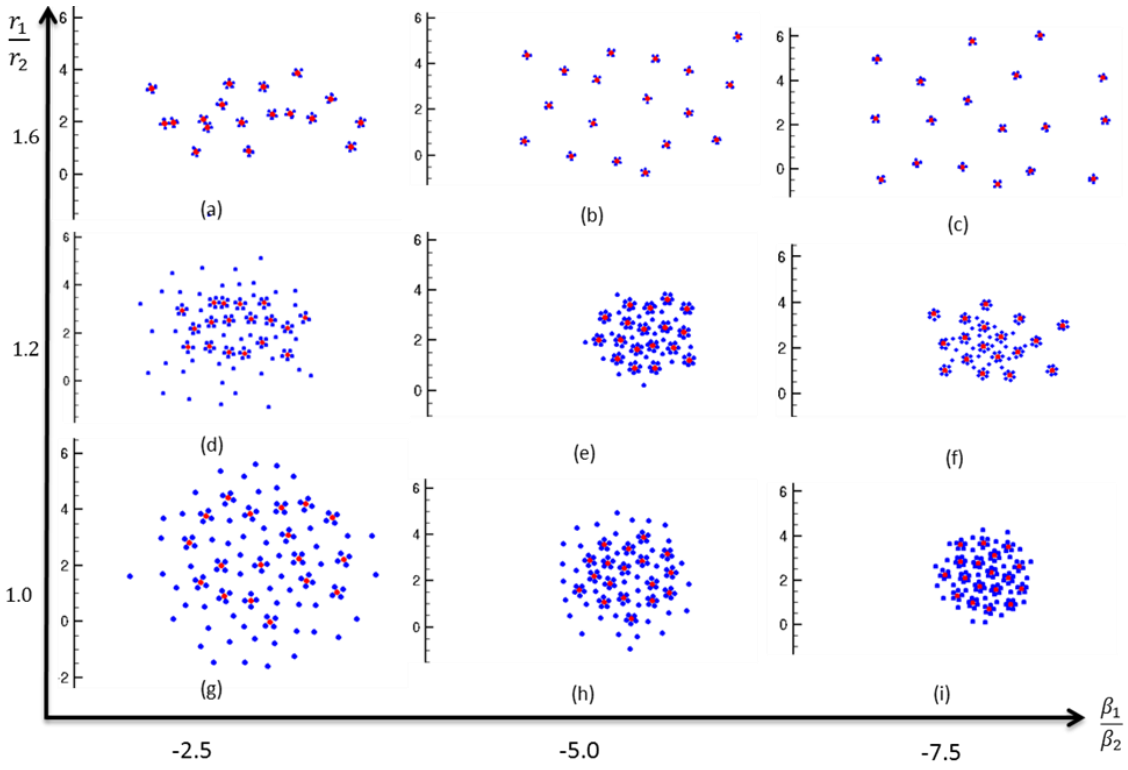

Figure 4.14 Numerical simulation of self-assembly of mixtures of particles for $E_0 = 95\,MV/m$; $\frac{r_1}{r_2}$ and $\frac{\beta_1}{\beta_2}$ were varied for three different values. Notice that some smaller (blue) particles in some of the cases are not in the viewing area, as they drifted away from the monolayer.

It is noteworthy that the tendency to form particle chains was not present in Figure 4.14, but in Figure 4.15 where $\frac{N_1}{N_2}$ =1 the two types of particles formed chains. All other parameters in Figures 4.14 and 4.15 were the same. Since the number of blue particles in Figure 4.14 was 7 times larger, there were not enough red particles present for forming chains. To form chains, the two types of particles must alternate. Notice that the length of particle chains decreased when $\frac{r_1}{r_2}$ or $\frac{\beta_1}{\beta_2}$ was increased, and when these parameter values were larger the chains contained

at most 3-4 particles. The area of the monolayer also increased when $\frac{r_1}{r_2}$ or $\frac{\beta_1}{\beta_2}$ was increased. We may therefore conclude that the tendency to form particle chains is the greatest when the particles are of the same size and $\frac{\beta_1}{\beta_2}$ is O(1).

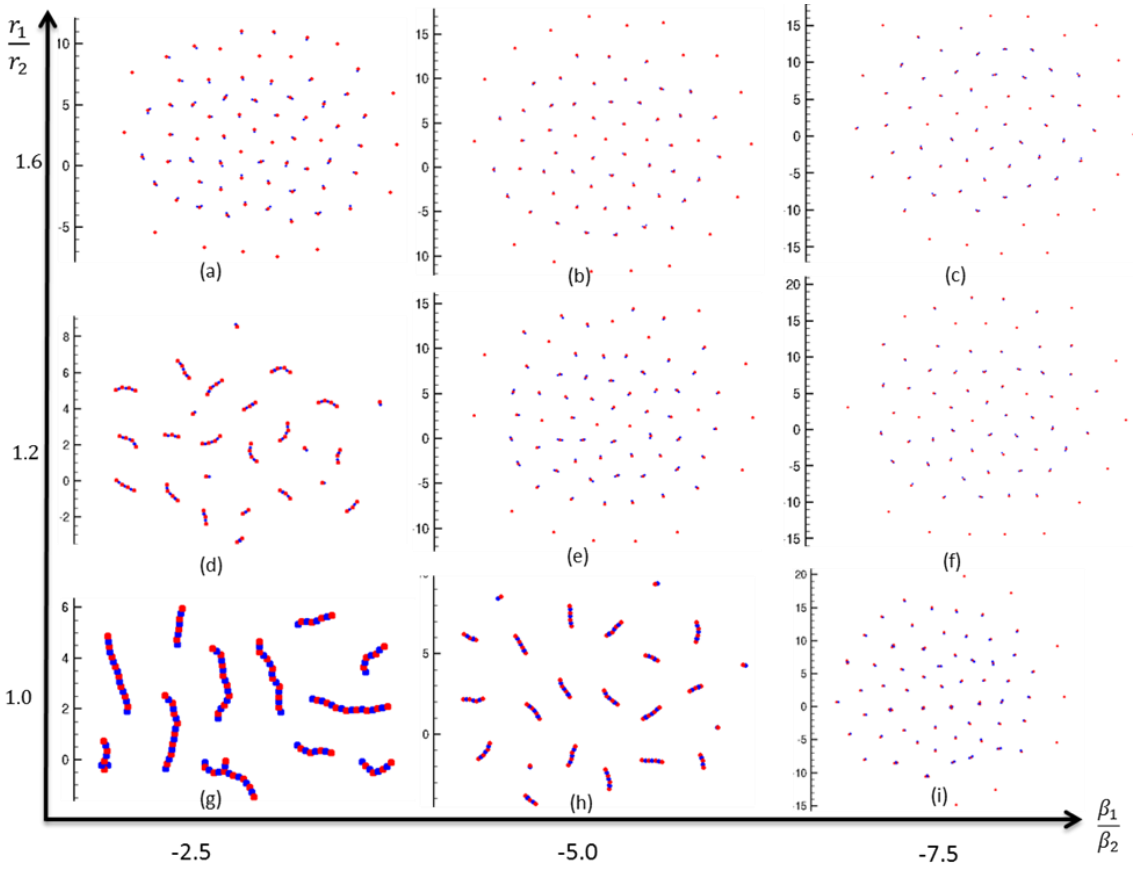

Figure 4.15 Numerical simulation of self-assembly of mixtures of particles for $N_1 : N_2 = 1:1$ and $E_0 = 95\ MV/m$; $\frac{r_1}{r_2}$ and $\frac{\beta_1}{\beta_2}$ were varied for three different values.

The above results show that when the electric field intensity is sufficiently large the two types of particles form composite particles and the assembled monolayers have no noticeable influence of Brownian motion. An increase in $\frac{\beta_1}{\beta_2}$

further weakened the influence of Brownian motion, making the monolayer arrangement well-ordered. But, as $\frac{r_1}{r_2}$ was increased, the capillary and dipole-dipole forces among the smaller particles decreased, and the influence of Brownian motion increased.

In Figures 4.16-4.18, the applied electric intensity was reduced to 60 MV/m, 35 MV/m and 10 V/m, respectively, to study its influence on the monolayer arrangement. All other parameter values in Figures 4.16-4.18 were the same as in Figure 4.14. Notice that as the field intensity was reduced, the monolayers became less ordered. For example, a comparison of Figure 4.14 and Figure 4.16 shows that although in both Figures particles combined to form composite particles, the arrangement of composite particles was more ordered and the distance between them was smaller when the electric field intensity was larger. This was more pronounced in Figures 4.14(g)-(i) and Figures 4.16(g)-(i), whereas in the former figures the composite particles formed a periodic lattice. This trend continued in Figure 4.17, where the composite particles were not arranged periodically and the number of smaller particle in the rings of composite particles was smaller. In Figure 4.18, even fewer composite particles formed and the particles were distributed over larger areas. The Figure also shows that the number of composite particles that were formed was greater when $\frac{\beta_1}{\beta_2}$ was larger. Figures 4.17-4.18

however show that increasing $\frac{\beta_1}{\beta_2}$ or $\frac{r_1}{r_2}$ has relatively smaller impact on enhancing order in the assembled monolayer, unlike in Figures 4.14-4.16, implying that there is a minimum electric field intensity below which Brownian forces dominate.

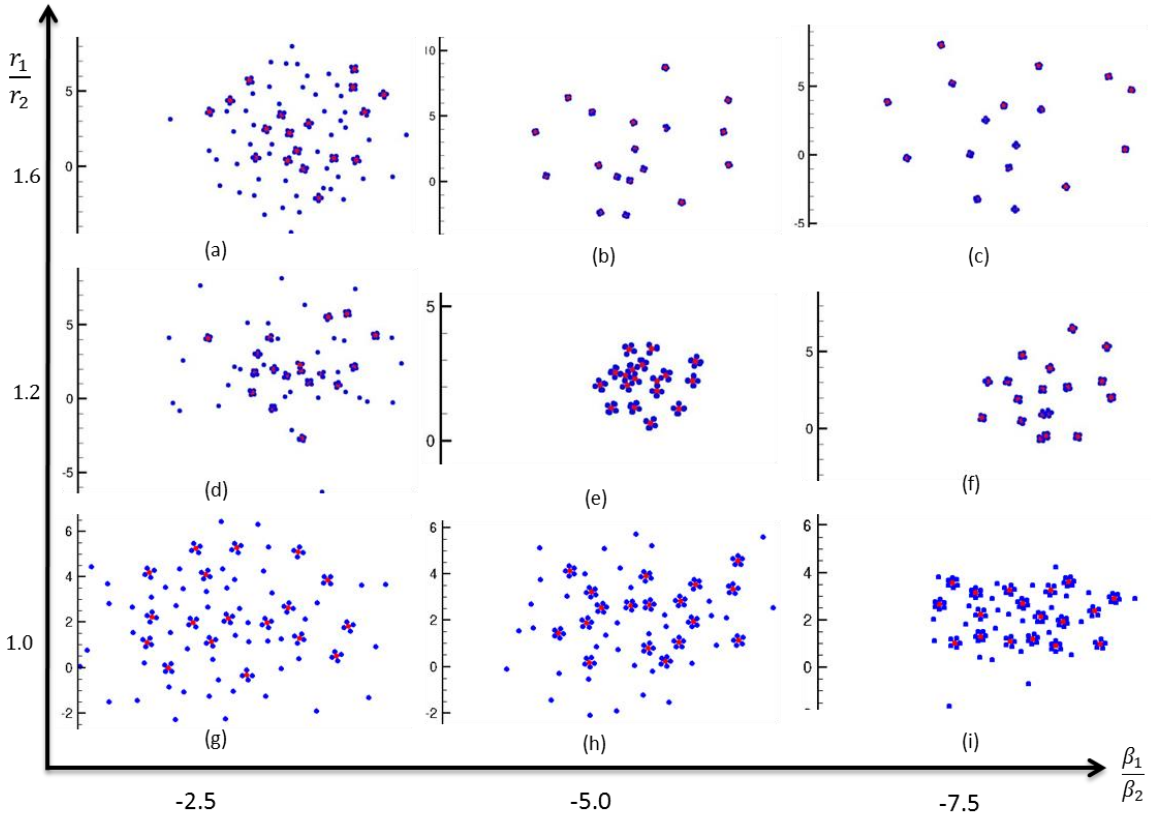

Figure 4.16 Numerical simulation of self-assembly of mixtures of particles for $E_0 = 60\ \mathrm{MV/m}$; $\frac{r_1}{r_2}$ and $\frac{\beta_1}{\beta_2}$ were varied for three different values.

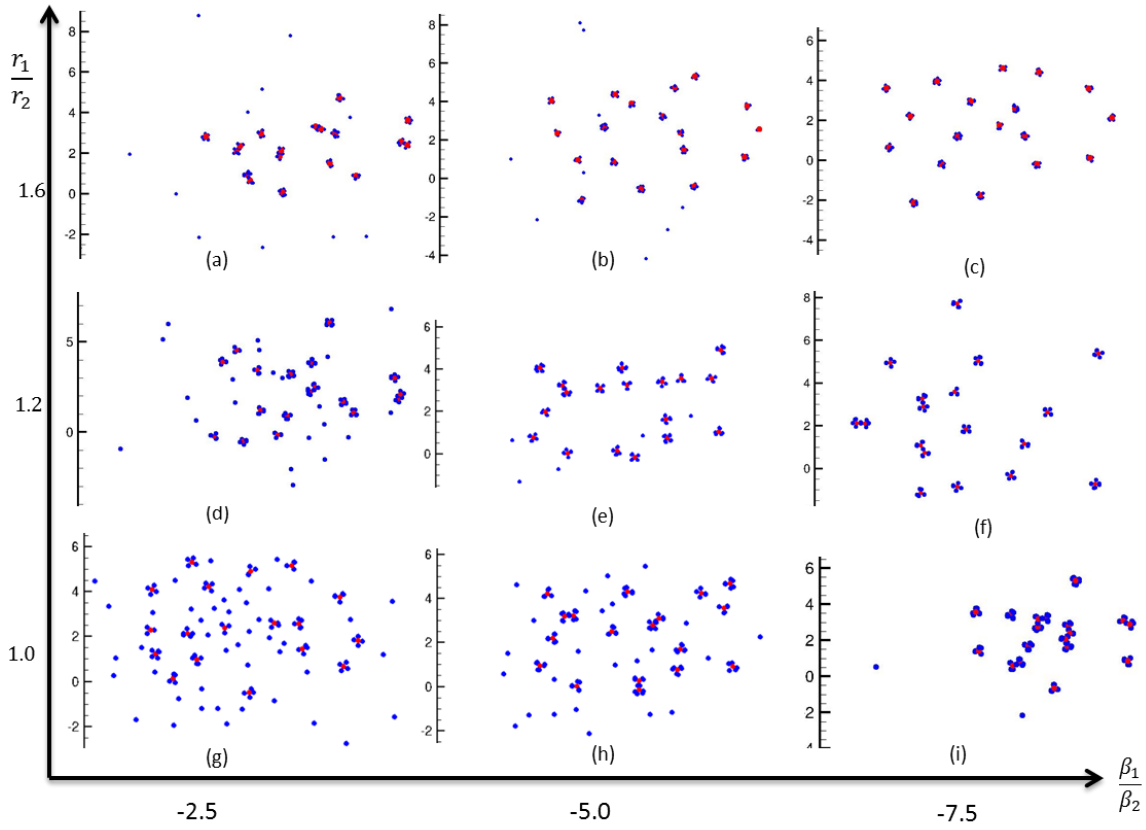

Figure 4.17 Numerical simulation of self-assembly of mixtures of particles for $E_0 = 35\ \mathrm{MV/m}$; $\frac{r_1}{r_2}$ and $\frac{\beta_1}{\beta_2}$ were varied for three different values.

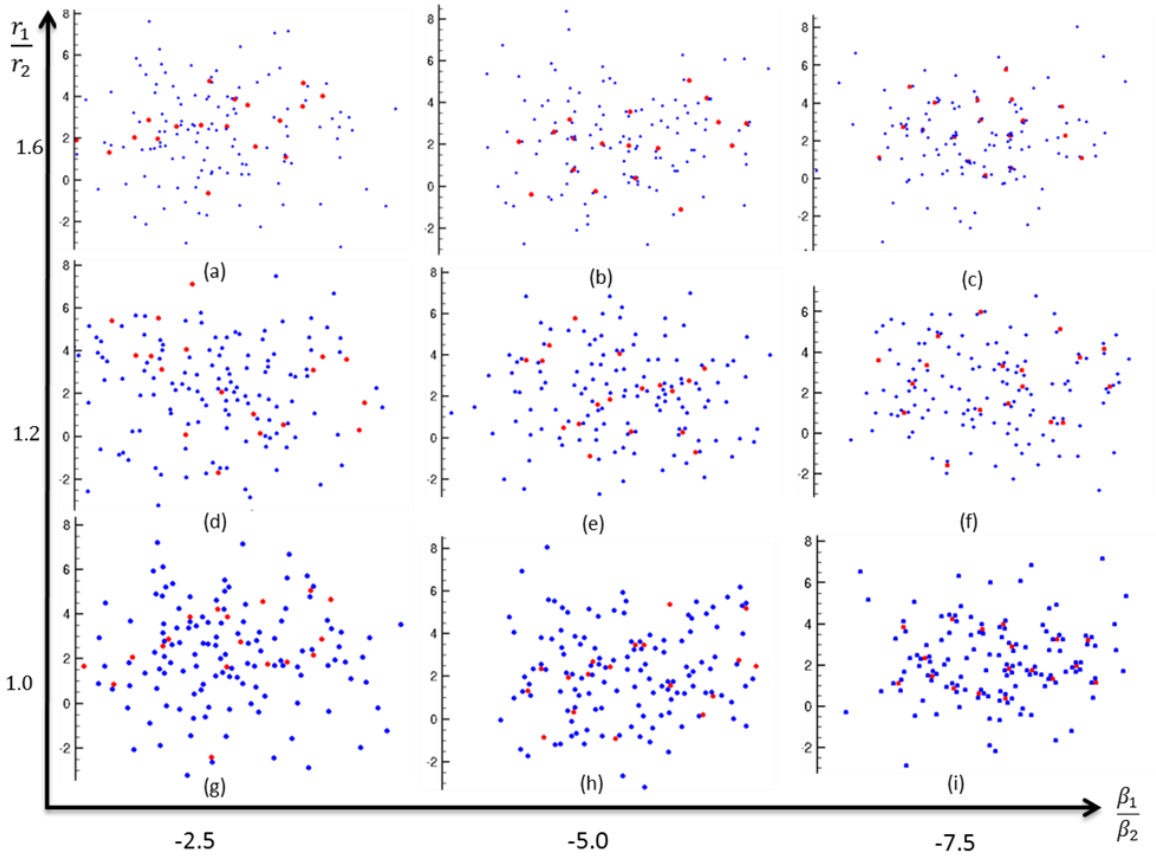

Figure 4.18 Numerical simulation of self-assembly of mixtures of particles for $E_0 = 10\,\mathrm{MV/m}$; $\frac{r_1}{r_2}$ and $\frac{\beta_1}{\beta_2}$ were varied for three different values.

4.5 Summary

We have numerically studied the self-assembly process of binary mixtures of particles adsorbed on a liquid surface when an electric field is applied normal to the surface. The electric field gives rise to lateral dipole-dipole and capillary forces which cause particles to self-assemble on the surface. The dipole-dipole force between two particles in a surface can be repulsive or attractive depending on the polarizabilities of the particles, and the intensity and direction of the force can be varied by selecting suitable upper and lower fluids. The force is repulsive when both particles are positively or negatively polarized, but attractive when one particle is positively polarized and the other is negatively polarized. The lateral capillary force between two particles depends on the net vertical forces acting on the particles which consist of their buoyant weights and the electric field induced vertical forces. The total lateral force is the sum of the capillary and dipole-dipole forces which among other factors depends on the electric field intensity. We have shown that the latter can be used to derive a hierarchical self-assembly process analogous to that which occurs at atomic scales.

The focus of this study is on binary mixtures for which the dipole-dipole force among the particles of different types is attractive. In this case, it is convenient to characterize the microstructure in terms of the dimensionless

equilibrium separations between two particles of the same types: $\overline{r}_1$ and $\overline{r}_2$. The particles of different types in equilibrium physically touch each other unless the capillary force between them is repulsive. Additionally, the strength of the inter-particle forces, together with their initial distribution, are important factors in determining the final monolayer arrangement. For example, if particles of type 1 move faster they will rearrange relatively quickly which can block the motion of particles of type 2 and thus prevent them from forming certain arrangements.

We have verified that numerical results obtained by integrating the system of Equation (4.5) for n particles correctly describe the self-assembly process of binary mixtures observed in experiments. The model parameters were obtained from the physical properties of the fluids and the particles. These parameter values were then used in Equation (4.5) to simulate the self-assembly process. As in experiments, groups of particles combined to form composite particles (analogous to molecules) and then these composite particles self-assembled in a pattern (like molecules arrange in a material). The force between similar particles was repulsive (because they had the same polarizabilities), and so they moved apart which allowed particles that attracted to come together relatively unhindered to form composite particles. The net force among the particles forming a composite particle

was attractive, and so after a composite particle was formed, it remained intact while the electric field was kept on.

The parameter values for glass and polymer particles adsorbed on a corn oil surface were used to simulate the size-dependence of the self-assembled monolayers observed in our experiments. Three size-dependent regimes identified in the experiments were numerically simulated. In the first regime, the particles attracted to form composite particles which consisted of a larger (glass) particle at the center that was surrounded by a ring of smaller (copolymer) particles. Larger particles were more intensely polarized than smaller particles. In the second regime, smaller (glass) particles were about three times smaller than larger (copolymer) particles, but they were more intensely polarized. In this case, smaller particles formed a triangular lattice in which larger particles were embedded, and depending on the electric field intensity were surrounded by 3-6 smaller particles. The number of particles decreased with increasing intensity as some of them escaped from the rings due to the dipole-dipole repulsive force when the electric field intensity was above a critical value. In the first regime, on the other hand, the monolayer expanded with increasing electric field intensity, but the number of particles in the rings did not vary with the intensity. In the third regime, the sizes of the two types of particles (glass and copolymer) were comparable. They formed chains in which

the two types of particles alternated instead of forming composite particles with ring-like arrangements. This formation of chains is analogous to the formation of long chained polymeric molecules, except that the former were formed by particles in two dimensions on the surface of a liquid.

In addition to the numerical validation of the three experimental regimes, other parameter values that were limited due to the availability of particles with specific dielectric constants and sizes were studied numerically. For example, simulations were performed for a range of $\frac{r_1}{r_2}$ and $\frac{\beta_1}{\beta_2}$; the results show that when $\frac{\beta_1}{\beta_2}$ is increased while keeping β_2 fixed, the tendency of larger and smaller particles to come together to form composite particles increased. This was because of an increase in the dipole-dipole attractive force among the smaller and larger particles which moved them closer, and an increase in the dipole-dipole repulsive force between the larger particles which kept them apart, making the formation of composite particles possible. Also, when $\frac{r_1}{r_2}$ was increased by reducing r_2, the inter-composite-particle spacing increased and some of the smaller particles were not employed in the formation of composite particles as they moved relatively slowly during the self-assembly process. The repulsive dipole-dipole force among the composite particles increased as the size of the negatively polarized (blue) particles decreased.

The case where the two types of particles were of the same size and had equal concentration in the mixture was also analyzed. We considered the cases where $\frac{f_{b1}}{f_{b2}}$ was fixed, while $\frac{f_{v1}}{f_{v2}}$ was varied. The monolayer assembled into particles pairs consisting of a positively and a negatively polarized particle. As $\frac{f_{v1}}{f_{v2}}$ was increased, the dipole-dipole repulsive force between the negatively polarized particles decreased, leading to greater influence of the capillary force. As a result, the binary composite particles coalesced to form particle chains. On the other hand, when the ratio $\frac{f_{v1}}{f_{v2}}$ was fixed, while $\frac{f_{b1}}{f_{b2}}$ was increased, the opposite was the case, as shown in Figure 4.11. The increase in $\frac{f_{b1}}{f_{b2}}$ caused the chains to break into smaller chains and then into binary particle pairs.

We also studied the role of $\frac{N_1}{N_2}$ on the monolayer arrangement. The total number of particles in the domain was kept fixed, while $\frac{N_1}{N_2}$ was varied. The results were obtained for the regimes in which the mixture self-assembled into composite particles with smaller particles forming rings around the larger ones. As the relative percentage of the smaller particles decreased, the monolayer involved into a circular shape and its area increased; this was as a result of an effective increase in the dipole-dipole force among the composite particles as the influence of the oppositely polarized particles decreased with decreasing size.

One of the effects of Brownian forces was to disrupt the formation of composite particles and so a stronger electric field was needed to self-assemble monolayers of nano-particles. Our simulations show that for the given parameter values there was a critical electric field intensity below which particles did not self-assemble into composite particles and continued to move under the action of Brownian forces. But, when the electric field intensity was above the critical value, particles organized to form composite particles which then arranged in a pattern. The critical electric field intensity was smaller when $\frac{\beta_1}{\beta_2}$ was larger and $\frac{r_1}{r_2}$ was O(1). When $\frac{r_1}{r_2}$ was O(1) and the concentration of the two types of particles was approximately equal, they formed chains. But, when there were more particles of one type, they self-assembled to form ring-like arrangements in which the particles that were fewer formed the cores. We may therefore conclude that binary mixtures of nano particles can be self-assembled into patterns similar to those formed by micron sized particles, but a stronger electric field will be required to overcome Brownian forces.

CHAPTER 5

CONCLUSION SUMMARY AND FUTURE STUDY

5.1 Dissertation Conclusion

This dissertation explores the physics and mechanisms behind electrohydrodynamic manipulations and self-assembly of particles at fluid-liquid interfaces.

Chapter 2 presented an efficient numerical scheme based on the Maxwell stress tensor method (MST) that was used to study the dynamical behavior of particles in a dielectrophoretic cage. Particles are assumed to be suspended inside a liquid and a nonuniform electric field is applied using the electrodes mounted in the domain walls, which causes positively polarized particles to collect in the regions where the electric field intensity is locally maximal and the negatively polarized particles collect in the regions where the electric field intensity is locally minimal. The DNS results obtained from this scheme are compared with the numerical results obtained from the point-dipole (PD) approximation method. The study shows that some final steady-state positions of two particles, including the orientations of the line joining their centers, for different starting configurations, differ for MST method and the point-dipole method. We find that the error in the point-dipole method, when compared with the MST results for the same problem,

increases as the distance between the particles decreases. Also, the error is relatively large when the particle radius is comparable to the domain size, which determines the length scale over which the electric field varies. An increase in the dielectric mismatch between the particles and the fluid is also found to amplify the error.

The model was extended in Chapter 3 to study the behavior of particles adsorbed on a drop surface at low electric field frequencies, when the drop and ambient liquids are weakly conducting dielectric liquids. The problem of manipulation of particles on liquid-liquid interfaces has received considerable attention in recent years because of its importance in a wide range of applications. For example, several recent studies have been conducted in which a dc electric field is applied to manipulate the distribution of particles. Here, the ac electric field gives rise to an EHD flow on the surface of the drop. The direction of the EHD flow can be pole-to-equator or equator-to-pole depending on the properties of the drop and ambient liquids. The flow causes particles adsorbed on the surface of the drop to move in its direction, and so the approach can be used to concentrate particles near the poles or the equator of the drop depending on the direction of flow. The frequency of electric field is an important parameter which can be used to adjust the magnitude of the EHD flow induced drag such that it is larger or

smaller than the DEP force. This is due to the fact that the EHD flow diminishes with increasing frequency and that there is a critical frequency at which the EHD flow induced drag on a particle becomes equal to the DEP force. For a frequency above the critical value, the DEP force dominates. When the fluid and particles properties are such that the EHD and DEP forces are in the opposite directions, particles can be collected, as well as moved, between the poles and the equator by varying the frequency of electric field. It was also shown that it is possible to separate the particles of a binary mixture when the critical frequencies for the two types of particles are different; in the sense that the two particle types can be separated, in a fractional manner, by tuning to corresponding critical frequencies of particle types that make up the mixture. We were able to separate a mixture of polystyrene particles and hollow glass particles. The approach is, thus, superior to traditional dielectrophoresis for which the frequency dependence is weak. It also serves as a step to further development of encapsulation technique that would drive innovation in the engineering of smart materials with robust applications in biological and physically processes.

In Chapter 4, experimental and numerical studies were conducted to study the process of self-assembly of monolayers of micron- to nano-sized particle mixtures on flat fluid-liquid interfaces, when an electric field is applied in the

direction normal to the interface. A particle mixture is made up of negatively and positively polarized particles. The inter-particle forces cause particle mixtures to self-assemble into monolayers of molecular-like hierarchical arrangements; consisting of particle chains or composite particles arranged in a pattern. A composite particle has a larger particle at the center, surrounded with a ring of smaller particles. As with the experimental results, the structure of a composite particle depends on factors such as the relative sizes and the number ratio of the particles, their polarizabilities, and the electric field intensity. The initial distribution also influenced the final arrangement especially when the speeds with which the two types of particles moved during the self-assembly process differed substantially. For nanoparticle monolayers, the composition of composite particles was relatively less uniform because of the mixing induced by Brownian motion. If the particles sizes differ by a factor of two or more, the composite particle has a larger particle at its core and several smaller particles forming a ring around it. Approximately same sized particles, when their concentrations are approximately equal, form chains (analogous to polymeric molecules) in which positively and negatively polarized particles alternate, but when their concentrations differ, the particles whose concentration is larger form rings around the particles with smaller concentration.

5.2 Future Study

For future work, I will further expand my work on the study of self-assembly and manipulation of adsorbed particles on drop surfaces and on planar fluid-liquid interfaces.

In the study of self-assembly and manipulation of adsorbed particles on drop surfaces, I will explore potential applications of Janus particles, self-assembled composite particles with variable surface properties. In the process, I will: (a) self-assemble mixture of particles with different dielectric properties adsorbed on drop surfaces to create Janus particles; and (b) study the possibility of self-assembly of monolayers of Janus particles on fluid-liquid interfaces.

In addition, I will perform direct numerical simulations of self-assembly of nanoparticle mixtures in three dimensions in uniform and nonuniform electric fields, where the role of molecular and Brownian forces in determining the microstructure will be quantified. Likewise, I will deploy molecular dynamics (MD) simulations to study the interaction behaviour of nanoparticles at fluid-liquid interface and the effects of induced electric forces on the self-assembly of adsorbed particles. From the study, I will attempt to accomplish the following: (a) develop a MD code to simulate the behavior of nanoparticles at air-liquid interfaces; and (b) model self-assembly of nanoparticles at fluid-liquid interfaces.

REFERENCES

[1] Washizu, M., et al., 1995, "Applications of electrostatic stretch-and -positioning of DNA," IEEE Transactions on Industrial Applications, **30**, pp. 835.

[2] Pohl, H.A., 1978, "Dielectrophoresis: the behavior of neutral matter in non-uniform electric fields, Cambridge University Press, Cambridge, NY.

[3] Hughes, M.P., Morgan, H., and Rixon, J.F., 2002, "Measuring the dielectric properties of herpes simplex virus type 1 virions with dielectrophoresis," Biochimica et Biophysica Acta, **1571** (1), pp. 1-8.

[4] Becker, F.F., Wang, X., Huang, Y., Pethig, R., Vykoukal, J., and Gascoyne, P.R.C, 1994, "The removal of human leukemia cells from blood using interdigitated microelectrodes," Journal of Physics D: Applied Physics, **27**, pp. 2659.

[5] Becker, F.F., Wang, X.B, Huang,Y., Pethig, R., Vykoukal, J, and Gascoyne, P.R.C., 1995, "Separation of human breast cancer cells from blood by differential dielectric affinity," *Proceedings of the National Academy of Sciences*, USA, **92**, pp. 860.

[6] Markx, G.H., Dyda, P.A., and Pethig, R., 1996, "Dielectrophoretic separation of bacteria using a conductivity gradient," Journal of Biotechnology, **51** (1), pp. 175-180.

[7] Hughes, M.P., and Morgan, H., 1998, "Dielectrophoretic trapping of single sub-micrometre scale bioparticles," Journal of Physics D: Applied Physics, **31**, pp. 2205.

[8] Voldman, J., et al., 2001, "Holding Forces of Single-Particle Dielectrophoretic Traps," Biophysical Journal, **80**, pp. 531.

[9] Green, N.G., Morgan, H., and Milner, J.J., 1997, "Manipulation and trapping of sub-micron bioparticles using dielectrophoresis," Journal of Biochemical and Biophysical Methods, **35**, pp. 89-102.

[10] Voldman, J., Toner, M., Gray, M.L., and Schmidt, M.A., 2003, "Design and analysis of extruded quadrupolar dielectrophoretic traps," Journal of Electrostatics, **57**, pp. 69-90.

[11] Pethig, R., Huang, Y., Wang, X.B., and Burt, J.B.H., 1992, "Positive and negative dielectrophoretic collection of colloidal particles using interdigitated castellated microelectrodes," Journal of Physics D: Applied Physics, **25**, pp. 881-888.

[12] Green, N.G., and Morgan, H., 1999, "Dielectrophoresis of submicrometer latex spheres. 1. Experimental Results," Journal of Physical Chemistry B, **103** (1), pp. 41-50.

[13] Hughes, M.P., and Morgan, H., 1999, "Measurement of bacterial flagellar thrust by negative dielectrophoresis," Biotechnology Progress, **15** (2). pp. 245-249.

[14] Jones, T.B., 1995, *Electromechanics of particles*, Cambridge University Press, Cambridge, NY.

[15] Nedelcu, S, and Watson, J.H.P, 2004, "Size separation of DNA molecules by pulsed electric field dielectrophoresis," Journal of Physics D: Applied Physics, **37**, 2197.

[16] Bonnecaze, R.T., and Brady, J.F., 1992, "Dynamic simulation of an electrorheological fluid," Journal of Chemical Physics, **96**, pp. 2183.

[17] Washizu, M., and Jones, T.B., 1996, "Generalized multipolar dielectrophoretic force and electrorotational torque calculation," Journal of Electrostatics, **38**, 199.

[18] Wang, X, et al., 1997, "General expressions for dielectrophoretic force and electrorotational torque derived using the Maxwell stress tensor method," Journal of Electrostatics, **39**, pp. 277.

[19] Singh, P., and Aubry, N., 2005, "Trapping force on a finite-sized particle in a dielectrophoretic cage," Physical Review E.

[20] Singh, P., and Aubry, N., 2004, "Particle separation using dielectrophoresis," *Proceeding of ASME Annual Meeting*, Anaheim, CA.

[21] Aubry, N., and Singh, P., 2006, "Control of electrostatic particle-particle interactions in dielectrophoresis," Europhysics Letters, **74**, pp. 623 629.

[22] Kadaksham, J., Singh, P., and Aubry, N., 2004, "Dynamics of electrorheological suspensions subjected to spatially non-uniform electric fields," Journal of Fluids Engineering, **126** (2), pp. 170-179.

[23] Kadaksham, J., Singh, P., and Aubry, N., 2004, "Dielectrophoresis of nanoparticles," Electrophoresis, **25**, pp. 3625.

[24] Kadaksham, J., Singh, P., and Aubry, N., 2005, "Dielectrophoresis induced clustering regimes of viable yeast cells," Electrophoresis, **26**, pp. 3738–3744.

[25] Kadaksham, J., Singh, P., and Aubry, N., 2006, "Manipulation of particles using dielectrophoresis," Mechanics Research Communications, **33**, pp. 108-122.

[26] Glowinski, R., Pan, T.W., Hesla, T.I., and Joseph, D.D., 1999, "A distributed Lagrange multiplier/fictitious domain method for particulate flows," International Journal of Multiphase Flow, **25** (5), pp. 755-794.

[27] Singh, P., Glowinski, R., Pan, T.W., Hesla, T.I., and Joseph, D.D., 2000, "A distributed Lagrange multiplier/fictitious domain method for particulate flows," Journal of Non-Newtonian Fluid Mechanics, **91**, pp. 165-188.

[28] Green, N.G., Ramos, A., and Morgan, H., 2002, "Numerical solution of the dielectrophoretic and traveling wave forces for interdigitated electrode arrays using the finite element method," Journal of Electrostatics, **56**, pp. 235-254.

[29] Li, H., and Bashir, R., 2002, "On the design and optimization of microfluidic dielectrophoretic devices: A dynamic simulation study," Biomedical Microdevices, **6**, pp. 289-295.

[30] Binks, B.P., 2002, "Particles as surfactants similarities and differences," Current Opinion in Colloid & Interface Science., **7**, pp. 21-41

[31] Ramsden, W., 1903, "Separation of solids in the surface-layers of solutions and 'Suspensions'. Preliminary Account," *Proceedings of the Royal Society*, **72**, pp. 156.

[32] Pickering, S.U., 1907, "Emulsion," Journal Chemical Society, London, **91,** 2001-2021.

[33] Menon, V.B, and Wasan, D.T., 1986, "Particle-fluid interactions with application to solid-stabilized emulsions part I. The effect of asphaltene adsorption," Colloids and Surface, **19**, pp. 89-105.

[34] Song, H., Tice, J.D., and Ismagilov, R.F., 2003, "Millisecond kinetics on a microfluidic chip using nanoliters of reagents," Angewandte Chemie International Edition, **42**, pp. 768.

[35] Dommersnes, P., et al., 2013, "Active structuring of colloidal armour on liquid drops," Nature Communications, 4, 2066, doi: 10.1038/ncomms3066.

[36] Rozynek, Z.J., et al., 2014, "Electroformation of Janus and patchy capsules," Nature Communications, **5,** 3945, doi: 10.1038/ncomms4945.

[37] Cayre, O.J., et al., 2012, "pH-responsive colloidosomes and their use for controlling release," Soft Matter, **8**, pp. 4717-4724.

[38] Li, J., and Stoever, H.D.H., 2008, "Doubly pH-responsive Pickering emulsion," Langmuir, **24**, pp. 13237-13240.

[39] Melle, S., Lask, M., and Fuller, G.G., 2015, "Pickering emulsions with controllable stability," Langmuir, **21**, pp. 2158-2162.

[40] Crossley, S., Faria, J., Shen., M., and Resasco, D.E., 2010, "Solid nanoparticles that catalyze biofuel upgrade reactions at the water/oil interface," Science, **327**, pp. 68-72.

[41] Ikem, V.O., Menner, A., Horozov, T.S., and Bismarck, A., 2012, "Highly porous polymer foams synthesized from particle stabilized emulsion templates," Advances in Material, **22**, pp. 3588 3592.

[42] Subramaniam, A.B., Abkarian, M., and Stone, H.A., 2005, "Controlled assembly of jammed colloidal shells on fluid droplets," Nature Materials, **4**, pp. 553 556.

[43] Allen, R.S., and Mason, S.G., 1962, "Particle behaviour in shear and electric fields. i. deformation and burst of fluid drops," *Proceedings of Royal Society London A, Mathematical and Physical Sciences*, vol. 267, pp. 45-61.

[44] Taylor, G., 1964, "Disintegration of water drops in an electric field," *Proceedings of Royal Society London A, Mathematical and Physical Sciences*, **280**, pp. 383-397.

[45] Taylor, G., 1966, "Studies in electrohydrodynamics. I. the circulation produced in a drop by an electric field." *Proceeding sof Royal Society London A, Mathematical and Physical Sciences*, **1425**, pp. 159-1966.

[46] Melcher, J.R., and Taylor, G.I., 1969, "Electrohydrodynamics: A review of the role of interfacial shear stresses," Annual Review of Fluid Mechanics, 1, pp. 111-146.

[47] Torza, S., Cox, R.G., and Mason, S.G., 1971, "Electrohydrodynamic deformation and burst of liquid drops," *Philosophical Transactions of the Royal Society A, Mathematical and Physical Sciences,* **269**, pp. 295-319.

[48] Salipante, P.F., and Vlahovska, P.M., 2010, "Electrohydrodynamics of drops in strong uniform dc electric fields," Physics of Fluids, **22**, pp. 112110.

[49] Ouriemi, M., and Vlahovska, P.M., 2014, "Electrohydrodynamics of particle-covered drops," Journal of Fluid Mechanics., **751**, pp. 106-120.

[50] Nudurupati, S., and Janjua, M., Singh, P., and Aubry, N., 2009, "Electrohydrodynamic removal of particles from drop surfaces," Physical Review E, **80**, 010402.

[51] Nudurupati, S., Janjua, M., Singh, P., and Aubry, N., 2010, "Effect of parameters on redistribution and removal of particles from drop surfaces," Soft matter, **6**, pp. 1157-1169.

[52] Nudurupati, S.C., Janjua, M., Aubry, N., Singh, P., 2008, "Concentrating particles on drop surfaces using external electric fields," Electrophoresis, **29**, pp. 1164-1172.

[53] Green, N.G., Ramos, A., and Morgan, H., 2002, "Numerical solution of the dielectrophoretic and travelling wave forces for interdigitated electrode arrays using the finite element method," Journal of Electrostatics, **56**, pp. 235-254.

[54] Heida, T., Rutten, W.L.C., and Marani, E., 2002, "Understanding dielectrophoretic trapping of neuronal cells: modelling electric field, electrode-liquid interface and fluid flow," Journal of Physics D: Applied Physics, **35**, pp. 1592-1602.

[55] Jones, T.B., and Washizu, M., 1996, "Multipolar dielectrophoretic and electrorotation theory," Journal of Electrostatics, **37**, pp. 121-134.

[56] Ramos, A., Morgan, H., Green, N.G., and Castellanos, A., 1999, "The role of electrohydrodynamic forces in the dielectrophoretic manipulation and separation of particles," Journal of Electrostatics, **47**, pp. 71-81.

[57] Aubry, N., and Singh, P., 2008, "Physics underlying controlled self-assembly of micro- and nanoparticles at a two-fluid interface using an electric field," Physical Review E, **77**, pp. 056302.

[58] Blanco, A., et al., 2000, "Large-scale synthesis of a silicon photonic crystal with a complete three-dimensional band gap near 1.5 micrometres," Nature, 405, pp. 437-440.

[59] Janjua, M., Nudurupati, S., Singh, P., and Aubry, N., 2011, "Electric field induced self-assembly of micro- and nanoparticles of various shapes at two-fluid interfaces," Electrophoresis, **32**, pp. 518–526.

[60] Cox, P.A., 1989, "Hydrophilous pollination," Annual Review of Ecology and Systematics, **19**, pp. 261-280.

[61] Kralchevsky, P.A., Paunov, V.N., Ivanov, I.B., and Nagayama, K., 1992, "Capillary meniscus interactions between colloidal particles attached to a liquid - fluid interface," Journal of Colloid and Interface Science, **151**, pp. 79 -94.

[62] Nikolaides, M.G., et al, 2002, "Electric field induced capillary attraction between like-charged particles at liquid interfaces," Nature, **420**, pp. 299-301.

[63] Singh, P., and Joseph, D.D., 2005, "Fluid dynamics of Floating particles", Journal of Fluid Mechanics, **530**, pp. 31-80.

[64] Singh, P., Joseph, D.D., and Aubry, N., 2010, "Dispersion and attraction of particles floating on fluid-liquid surfaces," Soft Matter, **6**, pp. 4310-4325.

[65] Singh, P., et al., 2103, "Molecular-like hierarchical self-assembly of monolayers of mixtures of particles," Scientific Reports, **4**, 7427.

[66] Lucassen, J., 1992, "Capillary forces between solid particles in fluid interfaces," Colloids and Surfaces, **65**, pp. 131.

[67] Nicolson, M.M., 1949, "The interaction between floating particles," *Proceedings of the Cambridge Philosophical Society*, **45**, pp. 288.

[68] Gust, D., Moore, T.A., and Moore, A.L., 2001, "Mimicking photosynthetic solar energy transduction," Accounts of Chemical Research, **34**, 40.

[69] Tang, Z., Zhang, Z., Wang, Y., Glotzer, S.C., and Kotov, N.A., 2006, "Self-assembly of CdTe nanocrystals into free-floating sheets," Science, **314**, pp. 274 278.

[70] Jiang, P., and McFarland, M.J., 2005, "Large-scale fabrication of wafer-size colloidal crystals, macroporous polymers and nanocomposites by spin-coating," Journal of the American Chemical Society, **126**, 13778, 13.

[71] Aubry, N., Singh, P., Janjua, M., and Nudurupati, S., 2008, "Assembly of defect-free particle monolayers with dynamically adjustable lattice spacing," *Proceedings of the National Academy of Sciences of the United States of America*, U.S.A., 105, pp. 3711–3714.

[72] Janjua, M., Nudurupati, S., Singh, P., and Aubry, N., 2009, "Electric field induced alignment and self-assembly of rods on fluid-fluid interfaces," Mechanics Research Communications, **36**, pp. 55–64.

[73] Dominguez, A., Oettel, M., and Dietrich, S., 2010, "Dynamics of colloidal particles with capillary interactions," Physical Review E, **82**, 011402.

[74] Singh, P., Hossain, M., Dalal, B., Gurupatham, S.K., and Fischer, I., 2012, "Thin films with self-assembled monolayers embedded on their surfaces," Mechanics Research Communications, **45**, pp. 54–57.

[75] Singh, P., and Joseph, D.D., 2000, "Sedimentation of a Sphere Near a Vertical Wall in an Oldroyd-B Fluid," Journal of Non-Newtonian Fluid Mechanics, **94**, pp. 179-203.

[76] Singh, P., Joseph, D.D., Hesla, T.I., Glowinski, R., and Pan, T.W., 2000, "Direct numerical simulation of viscoelastic particulate flows," Journal of Non Newtonian Fluid Mechanics, **91**, pp. 165-188.

[77] Ermak, D.L., and McCammon, J.A., 1978, "Brownian dynamics with hydrodynamic interactions," Journal of Chemical Physics, **69**, pp. 1352-1360.

[78] Climent, E., Maxey, M. R., and Karniadakis, G. E., 2004, "Dynamics of Self-Assembled Chaining in Magnetorheological," Fluids Langmuir, **20**, pp. 507-513.

[79] Singh, P., and Solanky, T.K.S., 2000, "Convection and local acceleration dominated regimes in Lennard-Jones systems," Physics Letters A., **266**, pp. 11-18.

[80] Singh, P., 1996, "Dynamics of an assembly of finite size Lennard-Jones spheres," Physical Review E, **53** (6), pp. 5904-5915.

[81] Wu, N., and Russell, W. B., 2009, "Micro- and nano-patterns created via electrohydrodynamic instabilities." Nanotoday, **4**, 180

[82] Wu, N., Pease, L. F. and Russel, W. B., 2005, "Electric-field-induced patterns in thin polymer films: Weakly nonlinear and fully nonlinear evolution." Langmuir, **21**, pp. 12290 12302.

[83] Collins, R. T., Jones, J. J., Harris, M. T. and Basaran, O. A., 2008, "Electrohydrodynamic tip streaming and emission of charged drops from liquid cones." Nature Physics, **4**, pp. 149 154.

[84] Vigo, C. R. and Ristenpart, W. D., 2010, "Aggregation and Coalescence of Oil Droplets in Water via Electrohydrodynamic Flows." Langmuir, **26**, pp. 10703–10707.

[85] Ristenpart, W. D., Jiang, P., Slowik, M. A., Punckt, C., Saville, D. A. and Aksay, I. A., 2008, "Electrohydrodynamic Flow and Colloidal Patterning near Inhomogeneities on Electrodes." Langmuir, 24, pp. pp. 12172 12180.

[86] Prieve, D. C., Sides, P. J. and Wirth, C. L., 2010, "2-D Assembly of colloidal particles on a planar electrode." Current Opinion in Colloids and Interface Science., **15**, pp. 160 174.

[87] Farook, U., Stride, E. and Edirisinghe, M. J., 2009, "Preparation of suspensions of phospholipid-coated microbubbles by coaxial electrohydrodynamic atomization." Journal of the Royal Society Interface, **6**, pp. 271 277.

[88] Brugarolas, T., Tu, F. and Lee, D., 2013, "Directed assembly of particles using microfluidic droplets and bubbles." Soft Matter, **9**, pp. 9046 9058.

[89] Cui, M., Emrick, T. and Russell, T. P., 2013, "Stabilizing Liquid Drops in Nonequilibrium Shapes by the Interfacial Jamming of Nanoparticles." Science, **342**, pp. 460 463.

[90] Dommersnes, P., Rozynek, Z., Mikkelsen, A., Castberg, R., Kjerstad, K., Hersvik, K. and Fossum, J., 2013, "Active structuring of colloidal armor on liquid drops." Nature Communications, 4, 2066.

[91] Rozynek, Z., Mikkelsen, A., Dommersnes, P. and Fossum, J. O., 2014, "Electroformation of Janus and patchy capsules." Nature Communications, **5**.

[92] Rozynek, Z., Dommersnes, P., Mikkelsen, A., Michels, L. and Fossum, J. O., 2014, "Electrohydrodynamic controlled assembly and fracturing of thin colloidal particle films confined at drop interfaces." The European Physical Journal Special Topics, **223**, pp. 1859–1867.

[93] Lanauze, J. A., Walker, L. M. and Khair, A. S., 2013, "The influence of inertia and charge relaxation on electrohydrodynamic drop deformation." Physics of Fluids, **25**.

[94] Melcher, J. R. and Taylor, G. I., 1969, "Electrohydrodynamics - a review of role of interfacial shear stress." Annual Review of Fluid Mechanics, 1, pp. 111–146.

[95] Ha, J. W. and Yang, S. M., 2000, "Electrohydrodynamics and electrorotation of a drop with fluid less conductive than that 9 of the ambient fluid." Physics of Fluids, **12**, pp. 764–772.

[96] Sato, H., Kaji, N., Mochizuki, T. and Mori, Y. H., 2006, "Behavior of oblately deformed droplets in an immiscible dielectric liquid under a steady and uniform electric field." Physics of Fluids, **18**, 127101.

[97] Jones, T. B., 1984, "Quincke rotation of spheres." IEEE Transactions on Industry Applications, **20**, pp. 845–849.

[98] Turcu, I., 1989, "Electric field induced rotation of spheres." Journal of Physics A: Mathematical and General, **20**, pp. 3301–3307.

[99] Lemaire, E. and Lobry, L., 2002, "Chaotic behavior in electrorotation." Physica A, 314, pp. 663–671.

[100] He, H., Salipante, P. F. and Vlahovska, P. M., 2013, "Electrorotation of a viscous droplet in a uniform direct current electric field." Physics of Fluids, **25**, 032106.

[101] Turcu, I. and Lucaciu, C. M., 1989, "Electrorotation -a spherical shell model." Journal of Physics A, 22, pp. 995–1003.

[102] Aussillous, P. and Quere, D., 2001, "Liquid marbles." Nature, **411**, pp. 924 927.

[103] Nushtaeva, A. V. and Kruglyakov, P. M., 2004, "Investigation of model emulsion films stabilized by solid particles: thickness of films, their stability, and interfacial tension." Colloid Journal, **66**, pp. 456 465.

[104] Cengiz, U. and Erbil, H. Y., 2013, "The lifetime of floating liquid marbles: the influence of particle size and effective surface tension." Soft Matter, **9**, 8980.

[105] Furst, E. M., 2011, "Directing colloidal assembly at fluid interfaces." *Proceedings of the National Academy of Sciences of the United States of America*, **108**, pp. 20853 2085.

[106] Cavallaro, M., Jr., Botto, L., Lewandowski, E. P., Wang, M. and Stebe, K. J., 2011, "Curvature-driven capillary migration and assembly of rod-like particles." *Proceedings of the National Academy of Sciences of the United States of America*, **108**, pp. 20923–20928.

[107] Cui, M., Emrick, T. and Russell, T. P., 2013, "Stabilizing liquid drops in nonequilibrium shapes by the interfacial jamming of nanoparticles." Science, **342**, pp. 460–463.

[108] Dommersnes, P., Rozynek, Z., Mikkelsen, A., Castberg, R., Kjerstad, K., Hersvik, K. and Fossum, J., 2013, "Active structuring of colloidal armor on liquid drops." Nature Communications, 4, 2066.

[109] Sato, H., Kaji, N., Mochizuki, T. and Mori, Y. H., 2006, "Behavior of oblately deformed droplets in an immiscible dielectric liquid under a steady and uniform electric field." Physics of Fluids, **18**, 127101.

[110] Salipante, P. F. and Vlahovska, P. M., 2013, "Electrohydrodynamic rotations of a viscous droplet." Physical Review E, **88**, 043003.

[111] Quincke, G., 1896, "Ueber Rotation em im constanten electrischen Felde." Annual Review of Physical Chemistry, **59**, pp. 417–86.

[112] Jones, T. B., 1984, "Quincke rotation of spheres." IEEE Transactions on Industry Applications, **20**, pp. 845–849.

[113] Turcu, I., 1987, "Electric field induced rotation of spheres." Journal of Physics A: Mathematical and General, **20**, pp. 3301 3307.

[114] Lemaire, E. and Lobry, L., 2002, "Chaotic behavior in electrorotation." Physica A, **314**, pp. 663 671.

[115] Ptasinski, K. J. and Kerkhof, P. J. A. M., 1992, "Electric field driven separations: Phenomena and applications," Separation Science and Technology, **27**, 995.

[116] Ha, J. W., and Yang, S. M., 1999, "Breakup of a multiple emulsion drop in a uniform electric field," Journal of Colloid and Interface Science, **213**, 92.

[117] Pieranski, P., 1980, "Two-dimensional interfacial colloidal crystals." Physical Review Letters, **45**, pp. 569–572.

[118] Wickmann, H. H. and Korley, J. N., 1998, "Colloid crystal self-organization and dynamics at the air/water interface." Nature, **393**, pp. 445–447.

[119] Kralchevsky, P. A. and Denkov, N. D., 2001, "Capillary forces and structuring in layers of colloid particles." Current Opinion in Colloid & Interface Science, **6**, pp. 383–401.

[120] Chan, D. Y. C., Henry, J. D. and White, L. R., 1981, "The interaction of colloidal particles collected at fluid interfaces." Journal of Colloid and Interface Science, **79**, pp. 410–418.

[121] Kralchevsky, P. A. and Nagayama, K., 2000, "Capillary interactions between particles bound to interfaces, liquid films and biomembranes." Journal of Colloid and Interface Science, **85**, pp. 145–192.

[122] Goulian, M., Bruinsma, R. and Pincus, P., 1993, "Long-range forces in heterogeneous fluid membranes." Europhysics letters, **22**, pp. 145–150.

[123] Aveyard, R. *et al.*, 2002, "Measurement of long-range repulsive forces between charged particles at an oil-water interface." Physical Review Letters, **88**, 246102-1-4.

[124] Dinsmore, A. D. et al., 2002, "Colloidosomes: selectively permeable capsules composed of colloidal particles." Science, **298**, pp. 1006 1009.